

Nanophotonic Waveguide Enhanced Raman Spectroscopy

Nanofotonische golfgeleiderversterkte Ramanspectroscopie

Ashim Dhakal

Promotoren: prof. dr. ir. R. Baets, prof. dr. N. Le Thomas
Proefschrift ingediend tot het behalen van de graad van
Doctor in de ingenieurswetenschappen: fotonica

Vakgroep Informatietechnologie
Voorzitter: prof. dr. ir. D. De Zutter
Faculteit Ingenieurswetenschappen en Architectuur
Academiejaar 2015 - 2016



ISBN 978-90-8578-928-4
NUR 950
Wettelijk depot: D/2016/10.500/60



GHENT UNIVERSITY
FACULTY OF ENGINEERING AND ARCHITECTURE
DEPARTMENT OF INFORMATION TECHNOLOGY

Examination Committee :

Prof. Dr. Ir. Patrick De Baets (**Chair**, Board of Governors, UGent)
Prof. Dr. Ir. Peter Bienstman (**Secretary**, Dept. INTEC, UGent)
Prof. Dr. Kevin Braeckmans (**Member**, UGent, Dept. Pharmaceuticals, UGent)
Prof. Dr. Ir. Jacob Caro (**Member**, Dept. Quant. Nanotech, Delft UTech.)
Prof. Dr. Ir. Thomas Krauss (**Member**, Dept. Physics, University of York)
Prof. Dr. Ir. Liesbet Lagae (**Member**, Director, Life Sci. Tech., IMEC)
Prof. Dr. Andre Skirtach (**Member**, UGent, Dept. Molecular Biotech.)

Advisers and non-voting members:

Prof. Dr. Ir. Roel Baets
Prof. Dr. Nicolas Le Thomas



A dissertation submitted to obtain
the degree of Doctor of Photonics Engineering
Academic Year 2015-2016

List of Acronyms

ATR	Attenuated total reflection (spectroscopy)
CCD	Charge-coupled device
cDNA	Complementary deoxyribonucleic acid
CMOS	Complementary-metal-oxide semiconductor (technology)
CM	Confocal microscope
DNA	Deoxyribonucleic acid
FWHM	Full width at half maxima
IPA	Isopropyl alcohol
LoD	Limit of detection
LDOS	Local density of states
MIR	Mid-infrared (wavelength region)
NA	Numerical aperture
NIR	Near-infrared (wavelength region)
NWERS	Nanophotonic waveguide enhanced Raman spectroscopy
SERS	Surface enhanced Raman spectroscopy
SNR	Signal to noise ratio
SNRF	Silicon nitride rich film
SOI	Silicon-on-insulator
SPM	Scanning probe microscopy
SPR	Surface plasmon resonance (technique for molecular detection)
TERS	Tip enhanced Raman spectroscopy
TE	(quasi) Transverse electric (polarization)
TM	(quasi) Transverse magnetic (polarization)
WGBL	Waveguide background luminescence
WGM	Whispering gallery mode (technique for molecular detection)

List of Symbols

P_0	Power emitted by a dipole in free-space
P_{in}	Input pump power to a waveguide or a free-space mode.
$P_{DL,0}(\vec{r}_0)$	Power scattered by a molecule located at a position \vec{r}_0 when excited by a diffraction-limited beam.
$P_{DL,B}$	Power collected from a bulk analyte by a diffraction-limited optics when excited by a diffraction-limited beam.
$P_{DL,S}$	Power collected from a adsobed surface analyte by a diffraction-limited optics when excited by a diffraction-limited beam.
P_{2D}	Total power collected by a 2D structure such as a waveguide from bulk cladding
$P_{col,s}$	Total power collected by a waveguide from surface molecules
P_{col}	Total power collected by a waveguide from bulk cladding
P_{tx}	Transmitted pump power (without the pump filter) through the waveguide measured by the Raman signal collection optics
$\zeta(l)$	Power collected by a waveguide normalized to the transmitted pump power, is a funtion of waveguide length l
$\xi(l)$	Power collected by a waveguide normalized to the input pump power.
$A_{eff,w}$	Effective interaction area for the a monolayer of particles on a waveguide contributing to the Raman signal.

$A_{eff}(\omega)$	Effective mode area in context of enhancement of emission, evaluated at an arbitrary cross-section of the waveguide.
$l_{eff}(\omega)$	Effective mode width in context of enhancement of emission, evaluated in the direction transverse to the symmetry.
l_{eq}	Equivalent length of the waveguide that provides same signal as that of the diffraction limited beam carrying the same power
$V_{eff,w}$	Effective interaction volume for the bulk analyte on top of a waveguide contributing to the Raman signal
$V_{eff}(\omega)$	Effective mode volume in context of enhancement of emission, evaluated at the maxima of the field.
$\tilde{V}_{eff}(\omega, \vec{r})$	Effective <i>local</i> mode volume in context of enhancement of emission, evaluated at \vec{r} .
ϕ	Bulk enhancement factor for NWERS compared to free space.
η_s	Conversion efficiency for surface species (monolayer); same as enhancement factor for NWERS compared to free space.
η_0	Conversion efficiency for bulk material or, for arbitrarily distributed particles.
σ, σ_{diff}	Differential (Raman) scattering cross-section.
σ_{norm}	Wavenumber normalized (Raman) scattering cross-section.
σ_{tot}	Total (Raman) scattering cross-section.
σ_{IR}	Infrared absorption cross-section.
σ_{flr}	Fluorescence emission cross-section.
β	Raman scattering efficiency for an ensemble of emitters (the product of σ and ρ)
ρ	Volume molecular number density (unit: m^{-3}).
ρ_s	Surface molecular number density (unit: m^{-2}).

s	Slot-sidith of slotted waveguide (assumed symmetric in this book.
h	Height of the waveguides (thickness of the deposited nitride) = 220 nm in this book.
w	Width of the waveguides.
$\bar{P}_{w,0}$	Scattered optical power coupled to a waveguide from a particle in the surrounding, normalized to the average of a diffraction limited beam carrying the same pump power.
Λ_{DL}	Integrated luminosity for a diffraction limited beam.
Λ_{cav}	Integrated luminosity for an arbitrary cavity.
Λ_{1D}	Integrated luminosity for an inhomegenous system with 1D symmetry such as a channel waveguide.
Λ_{2D}	Integrated luminosity for an inhomegenous system with 2D symmetry such as a slab waveguide.
D_{cav}	Local density of states inside an arbitrary cavity
D_0	Local density of states for freespace.
D_f	Total density of states for free-space (averaged over three othogonal directions)
D_{1D}	Local density of states for an inhomegenous system with 1D symmetry such as a channel waveguide
D_{2D}	Total density of states for an inhomegenous system with 2D symmetry such as a slab waveguide
$\vec{e}_g(\vec{r})$	Field profile vector for a diffraction limited (Gaussian) beam, normalized to the total energy/power flowing across the beam waist (unit: m^{-2}).
$\vec{e}(\vec{r})$	Field profile vector for a an arbitrary cavity, normalized to the total energy contained in the cavity (unit: m^{-3}).

$\vec{e}_1(\vec{r})$	Field profile vector for an inhomogeneous system with 1D symmetry, normalized to the total energy stored across its cross-section (unit: m^{-2}).
$\vec{e}_2(\vec{r})$	Field profile vector for an inhomogeneous system with 2D symmetry, normalized to the total energy stored per unit area across the plane of symmetry (unit: m^{-1}).
Δ_n	Index contrast for an arbitrary waveguide
Δ	Is the parameter due to a difference $\delta\alpha$ in waveguide losses for pump and Stokes frequencies, characterizing the deviation from the linear dependence.
Q_j^0	Average position of an ion in a molecule for a molecular vibration with index j
Q_j	Normal coordinate for the position of an ion in a molecule characterizing a vibration with index j
t_{int}	Signal integration (acquisition) time
$C(\omega_s)$	Photon-phonon coupling coefficient

This book is due to you. Thanks.

(in the order of size of the text)

Roel. For being my father figure.	Jury members. Bettering this work.
Nicolas. Pushing for the scientific exactness which have made all this very much better.	Ali. Doing some hard, boring but important experiments.
Frederic. Jeroen. My partner in crime (& research)	JanWillem. Techno-nights, and awesome parties.
Stephanne, Ananth, Eva. Numerous suggestions and advices.	Utsav, Sanjeev. Cooking my food and tolerating my mess.
Pieter W. Always being a supportive friend. Being open and critical to the several experiments we did together. Not the least: for the dutch translation of the summary.	Photonics Research Group. For your group meeting presentations, and the drinks afterwards, goodbye parties, Photonics days, light nights, good Fridays, bad Mondays,... the list never ends.
Nuria, Jindrich. Innumerable happy times: baziël, melac, spijker and, of course.. BTW is that lavender?	2*Ilse, Kristien, Mike, Michael I will rememeber your face full of joy, smile, and a helpful attitude; I wish I can be like you guys.

<p>Els, Sam & De Dappere Pootjes.</p> <p>Helping me explore this country the dappere way. You are brave, kind and awesome!</p>	<p>Ben, Jerry, Daniel, and RGSC diving team.</p> <p>Unforgivable times of flights, and the bike races!</p>
<p>Helena.</p> <p>The sweetest love.</p>	<p>Peter dC, Adil.</p> <p>Spiritual and philosophical explorations.</p>
<p>Ram, Lila, 2*Sunil.</p> <p>My mamaghar in Gent.</p>	<p>Asheesh, Sambridhi.</p> <p>My home in Gent.</p>
<p>Vinod Golu Nashib Piyush Raju Dina Bidur.</p> <p>I owe you.</p>	<p>Dhakal & Dahal Family.</p> <p>My dears who always supported me.</p>
<p>Kaka-hajurba,</p> <p>Atul & Savina,</p> <p>Sanjeeva & Avyudaya,</p> <p>Sova, and my Mom.</p> <p>I dedicate this work to you. Your incessant support and love made this possible.</p>	<p><i>My father.</i></p> <p><i>Here I Am Bereft Of You.</i></p> <p><i>Thus Without You, I Have Earned,</i></p> <p><i>What You Yearned For Me.</i></p> <p><i>Yet, Without Thee, I Would Not Be.</i></p> <p><i>Nor 'd I Be Me, Nor'd 'tis All Be.</i></p>

Gent, September 2016
Ashim Dhakal

Table of Contents

This book is due to you. Thanks.	xi
Table of Contents	xiii
Nederlandse samenvatting	xvii
English summary	xxiii
1 Introduction	1-1
1.1 Raman spectroscopy and its major challenges	1-1
1.2 The need for integrated photonics for Raman spectroscopy	1-2
1.3 Silicon nitride integrated waveguides for Raman spectroscopy . . .	1-4
1.4 Problem definition and research objective	1-6
1.5 Thesis outline	1-6
1.6 Contributions and Publications	1-7
2 A Brief review of light-matter interaction and Raman spectroscopy	2-1
2.1 Classical description of light-matter interaction	2-1
2.2 Scattering processes	2-2
2.2.1 Rayleigh scattering	2-3
2.2.2 Raman scattering	2-3
2.2.3 Brillouin scattering	2-5
2.3 Various definitions of scattering cross sections	2-6
2.4 Fluorescence	2-7
2.5 Infrared Absorption	2-8
2.5.1 Mutual Exclusion	2-9
2.5.2 Infrared Absorption spectroscopy	2-9
2.5.3 Problems with IR spectroscopy	2-9
2.6 Characteristics of spontaneous Raman scattering	2-11
2.7 Efficiency of Raman scattering in an ideal free-space system	2-12
2.7.1 Collection efficiency for bulk sensing	2-13
2.7.2 Collection efficiency for surface sensing	2-14
2.8 Closing Remarks	2-15

3	Enhancement of spontaneous scattering by optical confinement	3-1
3.1	Classical description of enhancement of emission	3-2
3.2	Enhancement of the emission in a cavity with a well-defined Q-factor	3-3
3.3	Scattering in a cavity with a well-defined Q-factor	3-4
3.4	Scattering in an inhomogeneous medium with a 2D invariance . .	3-6
3.4.1	Calculation of LDOS and enhancement	3-6
3.4.2	Scattering efficiency	3-7
3.5	Scattering in an inhomogeneous medium with a 1D invariance . .	3-8
3.5.1	Comparison with free-space excitation and collection . . .	3-9
3.6	Closing Remarks	3-10
3.6.1	Resonators formed with dielectric channel waveguides . .	3-11
3.6.2	Fluorescence and non-radiative transitions	3-12
4	NWERS of bulk material in the cladding	4-1
4.1	The efficiency of scattering	4-1
4.1.1	Efficiency for Strip waveguides	4-2
4.1.2	Efficiency for slotted waveguides	4-3
4.1.3	Equivalent length and enhancement	4-4
4.2	Considerations for coupling losses and waveguide losses	4-5
4.3	Experimental demonstration of evanescent Raman scattering . . .	4-6
4.3.1	Measurement setup	4-6
4.3.2	Evanescent spectroscopy of bulk liquid	4-7
4.4	Validation of the Theoretical Model	4-9
4.4.1	Sources of errors	4-9
4.5	Performance in comparison to the confocal microscopes	4-10
4.6	Closing Remarks	4-13
5	NWERS of Monolayers and thin layers	5-1
5.1	Importance of Raman spectroscopy of Monolayers	5-2
5.2	Collection efficiency for monolayers	5-3
5.3	Experiments	5-4
5.3.1	Demonstration of enhancement	5-4
5.4	DNA hybridization kinetics using spontaneous Raman signal . . .	5-7
5.5	Quantification of surface loading for a submonolayer of biotin and biotin-streptavidin complex	5-9
5.6	Determination of the cross-section of cy3	5-13
5.7	Raman spectroscopy of cell-membranes	5-13
5.7.1	Importance of Raman spectroscopy of Cell-membranes . .	5-13
5.7.2	Biocompatibility of Silicon Nitride and growth process . .	5-13
5.7.3	Spectrum of the cells	5-14
5.8	Closing Remarks	5-16

6	Dependence of the efficiency on channel waveguide parameters	6-1
6.1	Role of index contrast in the enhancement and scattering	6-1
6.2	A generic channel waveguide immersed in a medium	6-2
6.3	Integrated channel waveguides on a substrate	6-5
6.4	Closing Remarks	6-7
7	Background from waveguides and Signal-to-noise Ratio considerations	7-1
7.1	The origin of the waveguide WGBL	7-1
7.1.1	Raman features in the WGBL	7-1
7.1.2	Dependence with materials	7-2
7.1.3	Dependence on pump frequency	7-3
7.1.4	Dependence with pump power	7-5
7.1.5	Origin of the broad feature in the background	7-6
7.2	Determination of the WGBL efficiency	7-6
7.3	Modeling and subtraction of the WGBL	7-9
7.4	Closing Remarks	7-11
8	General conclusions and perspectives on Integration with plasmonic structures, resonators and spectrometers	8-1
8.1	Integration with plasmonic nanoantennas and comparison	8-2
8.2	Integrated resonators	8-2
8.3	Comparison with techniques based on refractive index sensing	8-3
8.4	General Conclusions	8-4
8.4.1	Microscope-less	8-4
8.4.2	Smallest étendue enabling integration with compact spectrometers and light sources	8-4
8.4.3	High Performance	8-5
8.4.4	CMOS compatible	8-5
8.5	Closing Remarks: Applications	8-5
A	Calculation of free-space Green's Dyadic	A-1
B	Calculation of Signal-to-noise ratio	B-1
C	DNA hybridization kinetics	C-1
D	Étendue of a beam, number of modes and spectrometer size	D-1
	References	D-5

Nederlandse samenvatting

–Summary in Dutch–

Nanofotonische golfgeleiderversterkte Ramanspectroscopie. Hoewel Ramanspectroscopie de laatste decennia een enorme vooruitgang gekend heeft in verscheidene disciplines, hebben tot heden weinig toepassingen de stap gezet heeft van het gespecialiseerde laboratorium naar een industriële omgeving. De extreem zwakke aard van Raman verstrooiing vereist niet alleen zeer gevoelige detectietechnieken, in veel gevallen is ook een versterking vereist van het intrinsieke signaal. Coherente, gestimuleerde of surface-enhanced Raman scattering zijn enkele geavanceerde methodes om deze versterking te bereiken. Een eenvoudiger concept bestaat erin het licht enerzijds te begrenzen tot een zeer klein volume en anderzijds gebruik te maken van een grotere interactielengte tussen het licht en de moleculen die aanleiding geven tot Raman verstrooiing. In dit werk bespreken we de verschillende aspecten van nanofotonische, golfgeleider-versterkte Ramanspectroscopie. We zullen aantonen hoe geïntegreerde enkelvoudige-mode golfgeleiders gebruikt kunnen worden om een Raman signaal zowel evanescent te exciteren als op te vangen, waarbij de intrinsieke voordelen van Raman spectroscopie in een lab-on-chip framework duidelijk worden. De combinatie van een groot detectievolume samen met de veldversterking nabij hoog index-contrast golfgeleiders leidt hierbij tot meer dan duizendvoudige signaalversterking in vergelijking met een conventionele Raman microscoop.

Fig. S.1 toont een logaritmische plot van het genormaliseerde Raman vermogen $\bar{P}_{w,0}$ dat op verschillende posities gekoppeld wordt naar de fundamentele TE mode van een door water omringde siliciumnitride slot golfgeleider ($s = 20$ nm, $w = 660$ nm). Teneinde dit te vergelijken met microscopische technieken is het Raman signaal in deze figuur genormaliseerd naar het totale Raman vermogen dat uitgestraald wordt door dezelfde molecule wanneer deze geëxciteerd wordt door een ideale, diffractie-gelimiterde lichtbundel ($NA = 1$) met hetzelfde vermogen in de vrije ruimte. De figuur toont aan dat het Raman vermogen dat gecollecteerd wordt van een molecule in de slot van de waveguide meer dan tien keer hoger is in vergelijking met het diffractie-gelimiterde systeem. Dit duidt op de immense mogelijkheid tot versterking van het Raman signaal door gebruik te maken van goed ontworpen golfgeleiders.

Naast de transversaal versterking, zoals geïllustreerd in Fig. S.1 is de meest belangrijke bijdrage aan de versterking bij het *NWERS* concept afkomstig van de longitudinale propagatie van de mode langsheen de golfgeleider. Hierdoor is het ef-

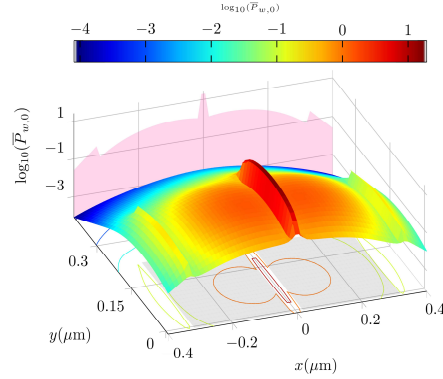


Fig. S.1| Genormaliseerd vermogen dat gekoppeld wordt golfgeleider TE-mode. $\log_{10}(\bar{P}_{w,0})$ in 3D weergegeven voor een slot-golfgeleider ($s = 20$ nm, $w = 660$ nm) maakt de variaties in gekoppeld vermogen langs de verschillende regio's van de doorsnede duidelijk. $\bar{P}_{w,0}$ is het vermogen dat door een molecule naar de fundamentele TE golfgeleider gekoppeld wordt, genormaliseerd naar de totale scattering van dezelfde molecule in de vrije ruimte geëxciteerd door een diffractie-gelimiteerde bundel met $\text{NA}=1$. De paarse schaduw geeft de projectie van $\bar{P}_{w,0}(\vec{r}_0)$ weer, met daarbij de maxima van $\bar{P}_{w,0}(\vec{r}_0)$. De grijs gearceerde regio in het x-y vlak geeft een doorsnede van de golfgeleider weer. De contouren stellen lijnen voor met dezelfde $\bar{P}_{w,0}$ waarvan de magnitude weergegeven wordt op de kleurschaal bovenaan $\bar{P}_{w,0}$.

fectieve interactievolumen dat bijdraagt aan het Raman signaal in een geleide mode $V_{eff,w}$ veel groter in vergelijking met het excitatie-volume in een microscopie-gebaseerde setup in de vrije ruimte. Dit interactievolumen kan willekeurig lang gemaakt worden door gebruik te maken van langere golfgeleiders, hierbij slechts gelimiteerd door de optische verliezen van deze golfgeleiders. Rekening houdend met de huidige technologie, waarbij verliezen kleiner dan 1 dB cm^{-1} mogelijk zijn, kunnen deze golfgeleiders ettelijke centimeters lang zijn alvorens een significant deel van het pompvermogen of Raman signaal te verliezen. Fig. S.2 geeft een illustratie van zulk een siliciumnitride, spiraalvormige, golfgeleider die gebruikt kan worden voor on-chip Ramanspectroscopie.

Dit staat in schril contrast tot een vrij-ruimte benadering, waarbij het effectieve meetvolume gelimiteerd is door de diffractie van de lichtbundel en beperkte focusdiepte. Een direct gevolg hiervan is dat de golfgeleider, in vergelijking met een conventionele microscoop, meer dan honderdmaal meer signaal geeft voor een bulk materiaal dat op de golfgeleider gedeponeerd is. Fig. S.3 toont de signaalversterking per eenheidslengte van de golfgeleider Φ in vergelijking met een ideale microscoop voor een vloeistof op deze golfgeleider.

Het voordeel van de golfgeleider wordt nog meer prominent wanneer men het oppervlak van deze golfgeleiders functionaliseert met monolagen van moleculen. In het geval van een diffractie-gelimiteerde spot is het effectief gemeten oppervlak bepaald door de piek-intensiteit en de breedte van de bundel w_0 . In het geval van

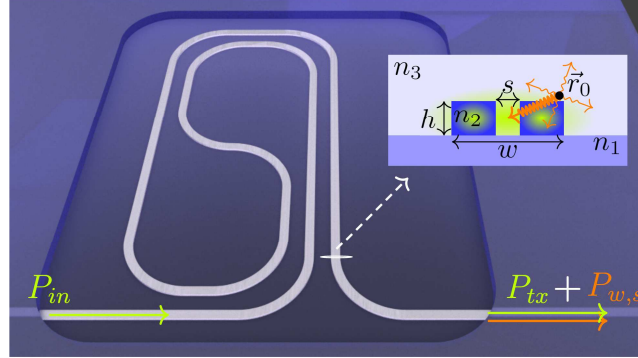


Fig. S.2 | Schema van een geïntegreerde golfgeleider voor Ramanspectroscopie. De inzet toont een dwarsdoorsnede van een typische slot-golfgeleider. Voor de golfgeleider in deze thesis is $n_1=1.45$ (SiO_2), $n_2=1.89$ (Si_3N_4), $n_3=1.33$ (H_2O), $h=220$ nm.

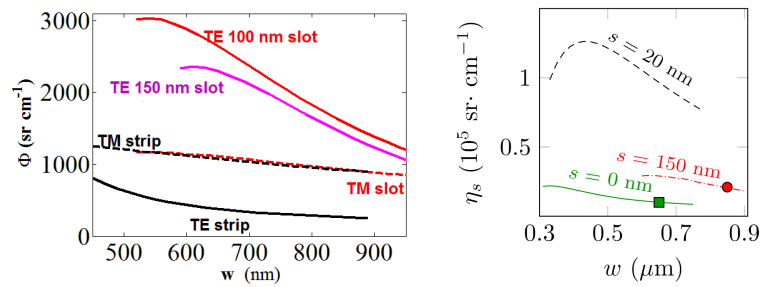


Fig. S.3 | **(Links)** Theoretische versterkingsfactor per eenheidslengte voor bulk metingen Φ in vergelijking met een confocale microscoop in functie van de breedte van de golfgeleider voor een strip- en slot siliciumnitride golfgeleider bij $\lambda_0 = 785$ nm. **(Rechts)** Berekende waarden voor de oppervlakte-efficiëntie η_s voor een golfgeleider vergeleken met de vrije ruimte, voor $h = 220$ nm, slot breedte $s = 0, 20$ nm en 150 nm in functie van de breedte van de golfgeleider w . De experimenteel onderzochte golfgeleiders zijn aangeduid met cirkels.

een golfgeleider is het effectieve interactieoppervlak dat bijdraagt tot het Raman signaal in een geleide mode $A_{eff,w}$ nagenoeg gelijk aan de totale oppervlakte van de golfgeleider A_{wg} . In dit geval leidt dit tot een signaalversterking van vijf grootteordes in vergelijking. Fig. S.3 (rechts) toont de versterking weergegeven door de parameter η_s voor oppervlaktemetingen in vergelijking met een vrije-ruimte microscoop.

Experimentele resultaten. De eerste demonstratie van evanescente Raman spectroscopie met nanophotonische golfgeleiders wordt weergegeven in Fig. S.4. Figuur S.4 (a) toont het achtergrondsignaal van de golfgeleider alvorens en na het aanbrengen van isopropyl alcohol (IPA). De achtergrond werd verwijderd door het

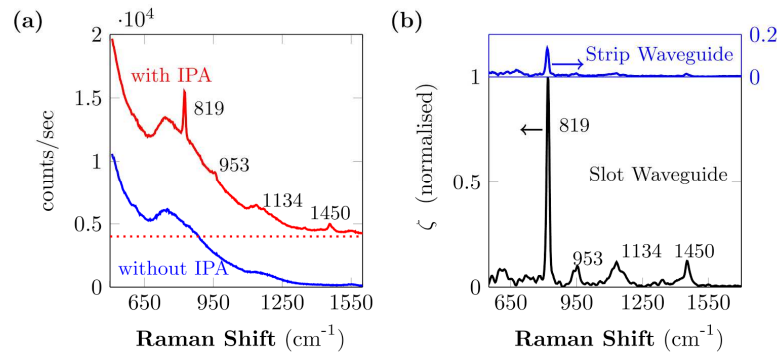


Fig. S.4 a) Spectra gemeten met een 1.6 cm golfgeleider zonder IPA (blauw) en met IPA (rood). Het spectrum van IPA is verticaal verschoven waarbij het nulpunt aangeduid is met de stippellijn. B) Typisch evanescent gemeten Raman spectrum van IPA na correctie voor het achtergrond spectrum. De spectra zijn genormaliseerd op de 819 cm^{-1} piek verkregen met een slot golfgeleider. ($w = 700$ nm, $s = 150$ nm). Het blauwe spectrum is opgemeten met behulp van een 700 nm strip Si_3N_4 golfgeleider.

aftrekken van een polynomische fit. Fig S.4 (b) toont een typisch Raman spectrum van IPA verkregen met deze procedure voor een $w = 700$ nm strip golfgeleider en een $w = 700$ nm slot golfgeleider met $s = 150$ nm. Hoewel we in beide gevallen de belangrijkste pieken van IPA duidelijk kunnen onderscheiden, is het signaal merbaar sterker voor slot golfgeleider.

Fig. S.5 vergelijkt de experimenteel geschatte waarden van de specifieke omzetting efficiëntie η_0 verkregen voor verschillende golfgeleider-geometrieën en –polarisaties met de theoretisch bepaalde waarden. De theoretische curves van η_0 in functie van de breedte van de golfgeleider w liggen binnen de foutenmarge van de experimentele data voor beide polarisaties en types van bestudeerde golfgeleiders. Dit bevestigt de waarde van het theoretische model dat in deze thesis ontwikkeld werd.

Fig. (S.6) toont een ander belangrijk resultaat van het werk in deze thesis, namelijk een verbetering van de signaal-ruis verhouding (SNR) en dus de detectielimiet (LoD) in vergelijking met confocale microscopie. Deze figuur toont de evolutie van SNR bij variaties in de dichtheid ρ_s of crosssectie σ van de moleculen. Meer dan twee grootteordes verbetering in SNR of LoD is verwacht bij NWERS voor eenzelfde pompvermogen en integratietijd.

Indien het hagelruis, afkomstig van het achtergrondsignaal van de golfgeleider, verminderd kan worden, kan een verbetering tot vier grootteordes in SNR of LoD bereikt worden. Vanuit een licht ander perspectief kunnen we stellen dat afhankelijk van de dominante bron van ruis en concentratie van het analyte, de golfgeleider-benadering toelaat de integratietijd met vier tot acht grootteordes te verminderen in vergelijking tot een vrije-ruimte systeem voor een vergelijkbare SNR en pompvermogen. Bovendien, zoals men kan zien in Fig (S.3) is de conversie efficiëntie nagenoeg invariant met kleine variaties in dimensies van de golfge-

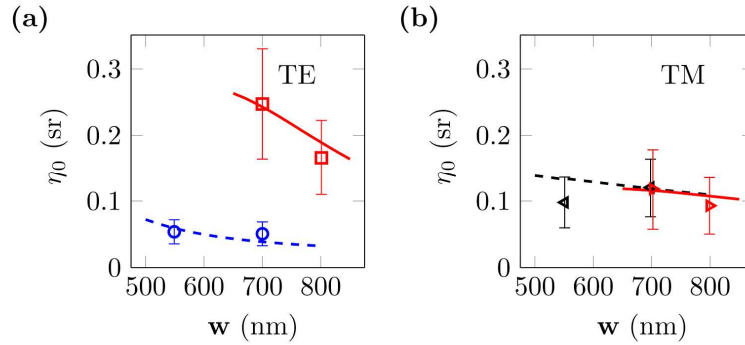


Fig. S.5 Theoretische en experimentele waarden van η_0 voor **a)** TE modes en **b)** TM modes van Si_3N_4 golfgeleiders. De markeringen met foutenmarge stellen de geschatte experimentele waarden voor. De lijnen geven de theoretische curves. De rode volle lijnen zijn theoretische curves voor slot golfgeleiders met $s = 150$ nm. De blauw en zwart gestippelde lijn zijn de theoretische curves voor respectievelijk TE en TM polarisaties voor strip golfgeleiders. Cirkels: TE polarisatie, strip golfgeleiders. Vierkanten: TE polarisatie, slot golfgeleiders. Linkshandige driehoeken: TM polarisatie, strip. Rechtshandige driehoeken: TM polarisatie, slot.

leider die kunnen voorkomen bij fabricage. ($< 4\%$ voor een variatie van 20 nm). Bijgevolg zal η zeer dicht bij de berekende waarde liggen, wat toelaat bepaalde grootheden accuraat te bepalen.

Perspectieven en conclusies. Ten gevolge van de versterking is het golfgeleider systeem superieur aan commerciële microscopen op het vlak van SNR. Door de exponentiele aard van de evanescente golf is er bovendien weinig bijdrage van achtergrondsignaal van ongewenst volume. Het is echter mogelijk om de detectielimiet voor zeer lage concentraties verder te verbeteren indien het aanwezige achtergrondsignaal van de golfgeleider zelf verlaagd van worden. Aangezien het onderliggende SiO_2 substraat een verwaarloosbare achtergrond heeft, is de grootste bron van achtergrondsignaal de Si_3N_4 kern van de golfgeleider zelf. De depositiemethode van dit Si_3N_4 is reeds sterk geoptimaliseerd om achtergrond te verminderen, maar kan mogelijk nog verder verbeterd worden. Het gebruik van alternatieve golfgeleider geometrieën zoals slot golfgeleiders met nauwere sloten enerzijds en TM polarisatie anderzijds kan mogelijk de achtergrond verder verminderen.

Onze resultaten met het golfgeleiderplatform breken de impasse van onpraktisch lange integratie tijden en onvoorspelbare signaalversterking die verscheidene toepassingen van Raman spectroscopie tot heden limiteren. Maar de voordelen van geïntegreerde optische golfgeleiders beperken zich niet enkel tot performantie. De kost en duurzaamheid geassocieerd met mature wafer-scale technologieën en bijkomende miniaturisatie is een belangrijke voorwaarde voor een wijdverspreid verbruik van de technologie. De kleine *étendue* van het opgevangen Raman sig-

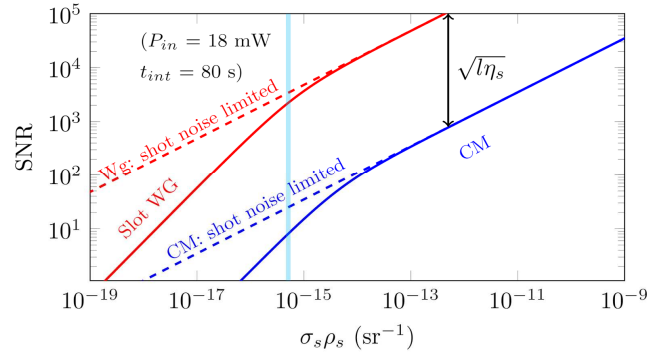


Fig. S.6 | Evolutie van SNR voor verschillende $\rho_s \sigma_s$ voor een monolaag van moleculen gebaseerd op de gemeten waarde (aangeduid met de verticale cyaan lijn). De evolutie voor een ideaal systeem, waarbij hagelruis van het signaal de enige ruisbron is, is aangeduid met stippellijn voor beide systemen.

naal in een enkelvoudige-mode golfgeleider laat bovendien de integratie toe met de kleinst mogelijke geïntegreerde spectrometers. Een performante, goedkope en compacte Raman sensor kan dus geïntegreerd worden op één chip. Bovendien kan dit platform gecombineerd worden met nanoplasmonische antennes voor SERS, waarbij een nog hogere signaalversterking het mogelijk maakt om zeer kleine volumes te detecteren.

Ter conclusie vatten we de voornaamste resultaten van het doctoraatsonderzoek in deze thesis samen:

1. Ontwikkelen van een model voor het kwantificeren van de versterking mechanismes nabij golfgeleiders en caviteiten. Voorspelling van het signaal in een realistische configuratie en de experimentele validatie hiervan.
2. Eerste demonstratie van evanescente Ramanspectroscopie met nanofotonische golfgeleiders.
3. Microscop-vrij, lab-on-a-chip, geïntegreerd CMOS compatible Raman platform voor zowel bulk vloeistoffen en monolagen van moleculen in het nabije infrarood.
4. Theoretische en experimentele demonstratie van minstens twee grootte-orders verbetering van signaal-ruisverhouding in vergelijking met een vrije-ruimte systeem door gebruik te maken van een geïntegreerd platform.
5. Onderzoek van het achtergrondsignaal van de golfgeleiders in functie van verschillende experimentele variabelen.

English summary

Nanophotonic waveguide enhanced Raman spectroscopy. Despite the enormous progress made over the past decades in demonstrating and identifying several applications, Raman spectroscopy has not yet found a widespread use as a point-of-need tool outside of the specialized labs. As the Raman scattering process is intrinsically weak, it requires advanced techniques to enhance and detect the signal. Coherent Raman scattering, stimulated Raman scattering, and surface enhanced Raman scattering (SERS) are only a few examples of advanced techniques devised to enhance the Raman signal. One method to enhance the Raman signal is to confine the light in a very small volume using nanophotonic waveguides thereby improving the evanescent interaction and simultaneously also extending the interaction volume, by the means of waveguiding, to boost the Raman signal. In this thesis, we discuss various aspects of this nanophotonic waveguide enhanced Raman spectroscopy (NWERS). We will show that integrated single-mode waveguides can be used to evanescently excite and collect Raman signals and have intrinsic performance advantages to implement Raman spectroscopy in a lab-on-a-chip framework. A large detection volume of the analyte molecules in the surrounding of a long single mode waveguide is combined with the field enhancement near a high-index-contrast waveguide to obtain more than three orders of magnitude larger signal compared to conventional free-space setup.

Let's first look at the enhancement due to mode confinement. To compare with the techniques based on optical microscopy (free-space), the collected power of the Raman signal from waveguides can be normalized by the corresponding total Raman power emitted by the same molecule when excited by the average intensity of an ideal diffraction limited beam (Numerical Aperture $NA = 1$) carrying the same pump power in the free space. Fig. S.1 displays the plot of the logarithm of the normalized Raman signal power coupled to the waveguide $\bar{P}_{w,0}$ for different positions of a scattering particle in the surrounding of a silicon nitride slot waveguide ($s = 20$ nm, $w = 660$ nm in Fig S.2) in water medium for fundamental TE mode (further discussed in §3.5.1). The figure shows that more than an order of magnitude of power is coupled to the waveguide mode compared to the total emission in the most ideal diffraction limited system. This illustrates an immense enhancement that could be utilized by the use of suitably designed waveguides.

In addition to the transverse enhancement, illustrated by Fig. S.1, the most significant component of the enhancement of the NWERS approach comes from the longitudinal propagation of the waveguide modes along the waveguide. The effective interaction volume contributing to the Raman signal in a guided mode $V_{eff,w}$

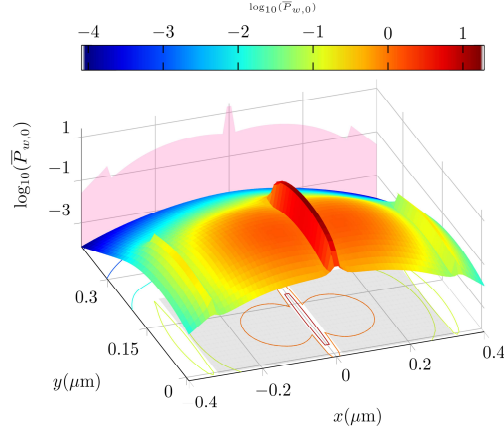


Fig. S.1| Normalized power coupled to the waveguide mode. $\log_{10}(\bar{P}_{w,0}(\vec{r}_0))$ for a slotted waveguide ($s = 20$ nm, $w = 660$ nm) shown in 3D highlighting the variations of the coupled power across the various regions of the section. $\bar{P}_{w,0}(\vec{r}_0)$ is the power coupled from a particle to the fundamental TE waveguide mode as a function of the emitter position \vec{r}_0 , normalized to the total emission from the particle when excited by a diffraction limited beam with $NA = 1$. The purple shaded area shows the projection of $\bar{P}_{w,0}(\vec{r}_0)$, indicating the maxima of the $\bar{P}_{w,0}(\vec{r}_0)$. The gray shaded region in the x - y plane indicates the waveguide cross-section. The contours represent the lines with the same $\bar{P}_{w,0}$ and the color bar shows the magnitude of $\bar{P}_{w,0}$.

is much larger than the confocal volume in a free-space setup. This $V_{eff,w}$ can be made arbitrarily large by using longer waveguide, limited only by the waveguide losses. With the current technology, waveguide losses smaller than 1 dB cm^{-1} are typical, thus allowing for waveguide lengths in the order of several centimeters without a significant loss of the pump or the Raman signal. Fig. S.2 is an illustration of the schematic of nanophotonic waveguide enhanced Raman spectroscopy (NWERS) illustrating a typical waveguide spiral. Such waveguide spirals can be made very compact in an area smaller than $500 \mu\text{m} \times 500 \mu\text{m}$ for 1 cm long waveguide.

In contrast to the NWERS approach, for a free-space approach the effective probed volume is determined by the limitations imposed by the diffraction on the waist of the beam and the depth of focus (§2.7). An important consequence of these results is that, for bulk materials placed on the top of the waveguides, the NWERS approach provides more than two orders of magnitudes stronger signal than the usual microscopic methods. Fig. (S.3) depicts the enhancement per unit length of the waveguide Φ compared to the ideal microscopes for bulk analyte.

The advantage of the NWERS compared to the free-space approach becomes more prominent for a monolayer of molecules functionalized on top of the waveguides. For monolayers observed by a diffraction-limited spot, the effective probed surface is determined by the peak intensity and the waist of the beam w_0 . The effective interaction area contributing to the Raman signal in a guided mode $A_{eff,w}$

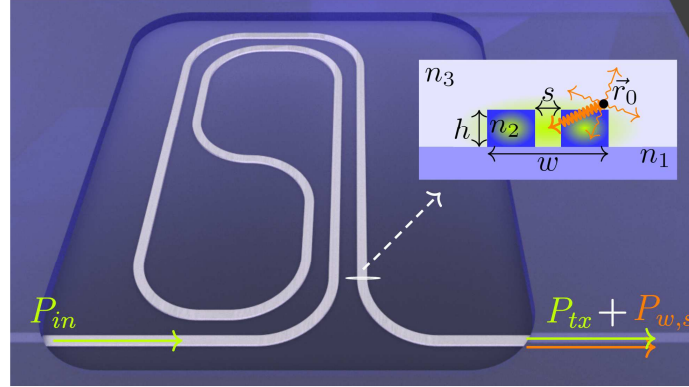


Fig. S.2| The schematic of the waveguide integrated Raman spectroscopic system. Inset shows a cross-section of a generic slot waveguide. For the waveguide used in this article $n_1 = 1.45$ (SiO_2), $n_2 = 1.89$ (Si_3N_4), $n_3 = 1.33$ (H_2O), $h = 220$ nm.

is almost equal to the total surface area A_{wg} of the waveguides. This leads to more than five orders of magnitude enhancement in the signal compared to the free-space approach (discussed further in §5.2). Fig. S.3 (Right) shows the enhancement (quantified by a parameter *surface conversion efficiency* η_s) for surface sensing compared to the free-space.

Further, as can be seen in Fig (S.3), the conversion efficiency values are practically invariant with small variations in the waveguide dimensions that might occur during fabrication ($< 4\%$ for a variation of 20 nm); hence it will remain very close to the calculated value in average. This makes the design of the spectroscopic system quite robust in spite of fabrication tolerances.

Experimental Results. The first demonstration of NWERS is presented in Fig. S.4. Fig. S.4 (a) shows the signal observed from the Si_3N_4 waveguide (§1.3) before and after application of an analyte on the upper cladding of the waveguide. The background luminescence from the waveguide observed before application of the analyte (in the present case it is isopropyl alcohol (IPA)) was fitted with a truncated polynomial and was removed by subtracting the corresponding polynomial fit (§7.4). Fig. S.4 (b) shows typical Raman spectra of IPA obtained using such a procedure for a strip waveguide with width $w = 700$ nm and a slotted waveguide with total width $w = 700$ nm and slot width $s = 150$ nm. All the major peaks of IPA are clearly distinguishable. A major highlight of Fig S.4 (b) is about 8 times enhanced signal for slotted waveguides. This demonstrates another important characteristic of the NWERS which allows us to tailor the waveguide enhancement.

In Fig. S.5, the experimental values of the specific conversion efficiency η_0 (defined as the ratio of collected Raman power per unit input pump power in a waveguide of unit length for particles of unit scattering cross-section distributed

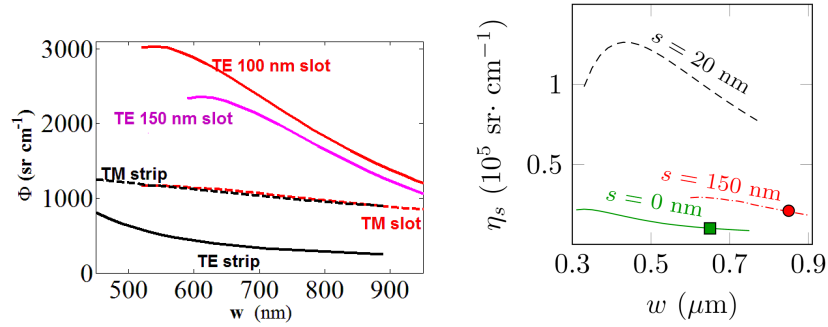


Fig. S.3 | (Left) Theoretical values for Φ defined as the enhancement factor per unit waveguide length for bulk sensing compared to the confocal microscope as a function of waveguide width for strip and slot silicon nitride waveguides and $\lambda_0 = 785 \text{ nm}$. (Right) Calculated values of η_s defined as the enhancement for surface enhancement for waveguide system compared to the diffraction-limited free-space system, for $h = 220 \text{ nm}$, slot widths $s = 0, 20 \text{ nm}$ and 150 nm as a function of waveguide width w . The waveguides investigated experimentally (discussed in §5.3.1) are marked with circles.

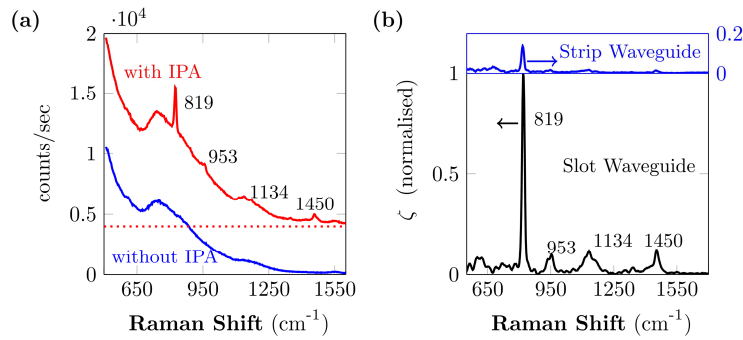


Fig. S.4 | **a**) Spectra measured from a 1.6 cm waveguide without IPA (blue) and with IPA (red). The spectrum with IPA is shifted vertically with zeros at red line shown. **b**) Typical evanescently measured Raman spectra of IPA after background subtraction. The spectra are normalized to the 819 cm^{-1} peak of obtained from a Si_3N_4 slot waveguide ($w = 700 \text{ nm}$, $s = 150 \text{ nm}$). The blue spectrum (with blue axes) is obtained by using a 700 nm wide Si_3N_4 strip waveguides.

uniformly in the vicinity of the waveguide with a unit number density, §4.1) obtained for various waveguide geometries and polarizations are compared with the theoretically determined values. The theoretical curves of η_0 as a function of waveguide width w are within the error margin of the experimental data for both polarizations and the waveguide types studied, thus validating the theoretical model that is developed in this thesis.

Another important result of the work presented in this thesis is displayed in Fig (S.6). It shows the improvement of the SNR and thus Limit of detection (LoD) compared to the confocal microscopes for the Raman signal collected from the

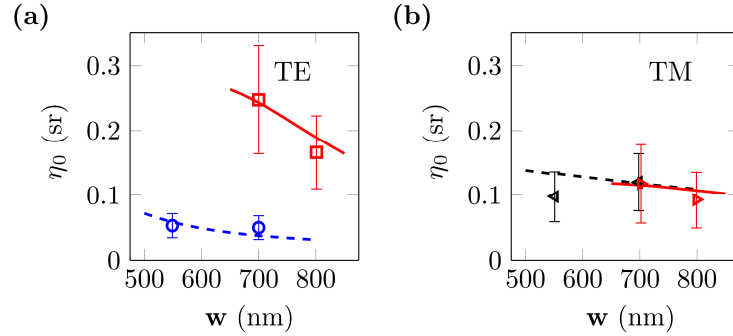


Fig. S.5 | The theoretical and experimental values of conversion efficiency η_0 obtained for **a)** TE modes and **b)** TM modes of Si_3N_4 waveguides. The markers with error bars represent the estimated experimental values. The lines represent theoretical curves. The red solid lines are the theoretical curve for slot waveguides with $s = 150$ nm. The blue and black dashed lines are the theoretical curves for TE and TM polarizations respectively for strip waveguides. Circle: TE polarization, strip waveguides. Square: TE polarization, slot waveguides. Left handed triangles: TM polarization, strip waveguides. Right handed triangles: TM polarization, slot waveguides.

adsorbed molecule monolayers. The figure is based on experimental data and illustrates the extrapolated SNR as a function of the product of the surface density of the molecules ρ_s and the cross-section of the molecules σ . Compared to confocal microscopes, more than two orders of magnitude improvement of SNR or LoD is expected with the NWERS for the same pump power P_{in} and same integration time t_{int} (§5.3.1).

A critical aspect of the NWERS that needs further study and optimization is the shot noise from the background luminescence from the waveguide material (§7). If this shot noise from the waveguide background luminescence can be reduced, the improvement of SNR or LoD can approach to four orders of magnitude (Appendix B). Seen from a slightly different perspective, depending on the dominating source of noise and the concentration of analyte, the waveguide-based approach leads to 4 to 8 orders of reduction in the integration time compared to the free-space system for a similar SNR and pump power.

As a result of the enhancement, the NWERS already out-performs the commercial microscopic systems in terms of SNR. Due to the exponential nature of the evanescent wave, the background from unwanted volume also poses little problem. However, the detection limit for a very low concentration can be improved further if the existing background, related to the properties of the waveguide material, can be reduced. While the SiO_2 under-cladding contributes negligibly to the background luminescence, the major source of the background in our measurements is due to the waveguide core material (§7). The deposition method of the waveguide Si_3N_4 has been improved significantly to reduce the background, and can possibly be improved further. The use of alternative waveguide designs such as the slotted waveguides with narrower slots and the use of TM polarization may further reduce

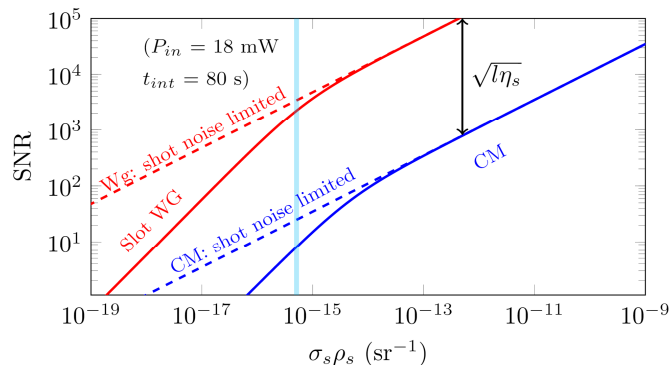


Fig. S.6 The SNR as a function of Raman efficiency (the product of surface density and cross-section) $\rho_s \sigma$ for a monolayer of molecules based on the measured value (indicated by the vertical cyan line) from slotted silicon nitride waveguide (WG) and a commercial confocal microscope (CM). Evolution of signal to noise ratio (SNR) for the ideal cases, i.e. when shot-noise from the signal coming from analyte is the only source of noise, is also shown in dashed lines for the respective systems. P_{in} is the input pump power, t_{int} is the integration time, l is the length of the waveguide and η_s is the surface conversion efficiency for the waveguide.

the background compared to the signal.

Perspectives and conclusions. Our results for single mode waveguide based NWERS approach break the impasse of impractically long integration times and unpredictable signal enhancement that several potential applications of Raman spectroscopy are facing. The asset of NWERS goes beyond performance advantages. The cost and reliability advantage associated with the use of mature wafer-scale technologies and the miniaturization is an important factor for widespread use of the technology. A key requirement for integration is a very small *étendue* (§Appendix D) of the light so that photonic structures remain compact. The smallest possible *étendue* of the collected signal in a single mode waveguide facilitates integration with the smallest possible integrated spectrometers for a given spectral resolution. A high performance, low cost, and compact Raman sensor can thus be integrated on a chip. Further, SERS can be performed by integrating nanoplasmonic antennas on the single mode waveguides when a considerably higher signal enhancement is desirable for the detection of small volumes of analyte (§8.1).

To conclude, the key results of the doctorate research presented in this thesis can be summarized as follows:

1. Development of the models for quantification of the enhancement mechanisms near waveguides and cavities, prediction of the signal in a practical situation and experimental validation thereof.
2. First demonstration of evanescent Raman spectroscopy using nanophotonic waveguides. Microscope-less, lab-on-a-chip, integrated, CMOS compatible

Raman spectroscopy of both bulk and a monolayer of molecules in the NIR wavelength region.

3. Characterization of the dependence of waveguide background luminescence spectrum from the waveguides as a function of different experimental variables.
4. Study of the impact of the waveguide background noise on the performance of the NWERS. Experimental demonstration of at least two orders of magnitude enhancement in SNR, compared to free-space system, by the use of the waveguide in an integrated platform.

1

Introduction

In this chapter, the context of this PhD thesis will be introduced and its objectives and key findings will be outlined. Some texts of this chapter have been adapted from my recently published review article [1].

1.1 Raman spectroscopy and its major challenges

Raman scattering is a scattering process where incident photons are scattered *inelastically* by the molecules. Here the term *inelastic* refers to the fact that there are net exchanges of energies between the molecules and the incident photons, with a net loss of energy from the scattering particles into new photonic and vibronic states. The lost energy results in shifts in the frequency of the scattered photons compared to the frequency of the incident photons and changes in the vibrational energies of the scattering molecules [2] - [4]. The frequency of the scattered photon is shifted by an amount corresponding to vibrational energies of the molecules and the intensity of the scattered light is proportional to the number of scattering molecules and the intensity of the incident light. Hence, the Raman spectrum constitutes a specific pattern that allows one to identify the molecules, quantify their number, and to study their vibrational properties. In his Nobel lecture Sir C. V. Raman, the discoverer of the Raman effect, himself recognized Raman spectroscopy as “the new field of spectroscopy {that} has practically unrestricted scope in the study of problems relating to the structure of matter” shortly after the discovery of the Raman Effect [5]. However, it was not until the technological advances

after mid-1980s that Raman spectroscopy established itself as a mainstream analytic tool for analytic chemistry and biology. The major drawback of Raman spectroscopy is the extremely small cross-section of the spontaneous Raman scattering process. It is in the order of 10^{-30} cm², which is fifteen orders of magnitude smaller compared to fluorescence that competes with this process in detection systems [2]. Advances in improved Charge-Coupled Device (CCD) detectors, near infrared (NIR) diode lasers, dielectric filters and computer technology improved the applicability of the technique for various scientific problems [6]. Since then, owing to its non-invasive and label-free nature, Raman spectroscopy has been established as a powerful spectroscopic technique for basic research and a myriad of applications ranging from biology, chemistry to material sciences [3] - [4]. Scientists have applied Raman spectroscopy for a wide variety of remarkable applications such as the study of viruses [7], the classification of tumour cells [8] and the detection of single molecules [9].

Despite the enormous progress made over the past decades in demonstrating and identifying several applications, Raman spectroscopy has not yet found a widespread use as a point-of-need tool outside of the specialized labs. The extremely weak nature of the Raman scattering process necessitates advanced techniques to enhance and detect the signal. Coherent Raman scattering [10], stimulated Raman scattering, and surface enhanced Raman scattering [11] - [12] (SERS) are only a few examples of advanced techniques devised to enhance the Raman signal. However, in conventional setups these techniques still require a confocal microscope combined with advanced laser sources, detectors and usually a large monochromator with a cooled detector, hence, limiting the use of the Raman spectroscopic techniques to specialized lab environments. In short, Raman spectroscopy has an enormous potential in bio-chemical analysis, if the sensitivity can be improved and if the spectroscopic devices can be made cheaper and handier.

1.2 The need for integrated photonics for Raman spectroscopy

An integrated electronic circuit is a well-known example of a monolithic integration where several electronic components and functionalities are miniaturized, integrated and fabricated together on a single substrate, thereby simultaneously reducing the size, parasitic effects and cost of the integrated system. With the advent of integrated laser diodes, the applications and complexity of photonic components have tremendously grown, from telecom applications and consumables, to biochemical sensing. The increase of complexity in optical systems has demanded the need of application specific and seamless integration of the photonic components to reduce the size, coupling losses and cost. Other advantages for the

photonic integration are:

1. Elimination of moving parts that take up significant amount of efforts and cost to stabilize the optical system.
2. Elimination of the need of beam alignment within the optical circuitry.
3. Reduction of coupling and misalignment losses due to seamless integration.
4. Reduction of the system size, leading to small form-factor, portable, and pluggable devices.
5. Reduction of the cost by the use of optimized processes of mass fabrication of a device.
6. Possibility of modular designs which could be reusable for similar devices.

The efforts of photonic integration have led to the development of dielectric waveguides integrated on a substrate like silicon, so that light could be produced, propagated and utilized by wave-guiding within a photonic chip without a significant optical loss. Dielectric waveguides constitute a high refractive index (n_{core}) material called *core* surrounded by, one or more, lower refractive index materials called *cladding* (with lowest refractive index n_{clad}) so that the light is guided in the core by total internal reflection [13].

Optical fibres are a well-known example of dielectric waveguides (not yet integrated) with a very low *index contrast* Δ_n , defined as $\Delta_n = 1 - n_{clad}/n_{core}$. In the realm of integrated photonics, however, a high index core is usually defined by silicon (Si, refractive index $n_{si} = 3.45$) on top of a low refractive index material such as silica (SiO₂) undercladding (refractive index $n_{ox} = 1.45$), by selectively etching the unwanted Si region [14] [15]. This particular example of a platform for defining Si waveguides on SiO₂ is popularly called the silicon-on-insulator (SOI) technology platform or simply called silicon photonics. It is the epitome of high index contrast waveguide integration platforms and has matured substantially in the recent years. Silicon photonics makes use of the standard materials and lithographical technologies available in an advanced CMOS fab developed and matured over past fifty years for the electronics industry. The price per silicon chip can thus be kept minimal thanks to the use of the high yield mass-fabrication process in a well-established CMOS fab.

An important aspect of silicon photonics is the use of high index contrast waveguides. High index contrast waveguides confine the light in a very small area, which leads to many advantages. One important advantage of the high index contrast waveguide is the enhancement of the field intensity in the vicinity of the waveguides, thus increasing the light-matter interaction, which we shall explore in forthcoming chapters. Another critical advantage is the significant reduction

of *étendue* (the product of the area A and the solid angle Ω of a light beam, see §Appendix D) of pump and signals that allows small spectrometers with an optimal spectral resolution, and facilitates compact integration. Yet another advantage is a small circuit size due to the possibility of using a small bend radius for the waveguides.

The development of optoelectronic and photonic technologies such as diode lasers and CCD detectors has enormously advanced the use of Raman spectroscopy for numerous applications [6]. Recent advances in integrated photonics technology have opened up unique ways towards cheap and compact point-of-need Raman analysis tools by integrating the essential components of the spectroscopic system on a chip [16]- [17]. However, effective transduction methods to generate Raman signals in an on-chip integrated Raman spectroscopic system have remained largely unexplored. A large enhancement and a small *étendue* are two key requirements of a transduction method for an integrated Raman sensor. A large enhancement is needed to eliminate the necessity of cooled detectors and expensive filters which are typically used in Raman spectroscopy. A small *étendue* is essential to keep the size of the integrated spectrometer as small as possible for a given resolution and sensitivity. These requirements have neither been identified nor addressed in an integrated setup.

Nevertheless, Kanger et al, have demonstrated the use of multilayer planar waveguides for the evanescent excitation of adsorbed thin layers for Raman spectroscopy [18]. Although this technique is not readily integrable with an optimal on-chip spectrometer, and still requires a conventional microscope to collect the signal from the top, this work took the idea of confining light and extending the interaction volume to boost the Raman signal using waveguides proposed by Rabolt et. al. [19]. The readers are referred to [20] for a review of spectroscopic techniques based on planar waveguides. Photonic crystal fibres filled with gaseous analyte [21] and hollow core fibres filled with liquid analyte [22] are other popular examples of the techniques that recognize wave-guiding as a mechanism to enhance Raman signal, but fail to be directly integrable on a chip. In this thesis advantages, challenges and prospect of the use of integrated photonics for Raman spectroscopy will be explored. In the next section CMOS compatible silicon nitride integrated photonics technology mainly developed for the purposes of visible light biospectroscopy is briefly discussed.

1.3 Silicon nitride integrated waveguides for Raman spectroscopy

A standard SOI integration platform, with a pump wavelength $\lambda_0 = 1.55\mu\text{m}$, would be a possible choice for on-chip Raman spectroscopy, owing to its maturity and

extensive use in the long-haul telecom applications and compatibility with CMOS technology. However, the Raman scattering cross-section roughly scales as λ^{-4} – the inverse to the fourth power of the pump wavelength [2]. Thus, a shorter wavelength is generally preferred as long as the fluorescence and absorption, characteristically associated with the use of shorter wavelengths, remains manageable. A near-infrared wavelength of 785 nm is a popular choice in Raman spectroscopy for biological applications because of the low water absorption, low fluorescence originating from biological molecules, but still fairly short wavelength for achieving a reasonably high scattering cross-section. The availability of high efficiency, high quality and low-cost sources and detectors in the 700-1000 nm wavelength region is also an important drive for the choice of 785 nm wavelength. Unfortunately, the popular SOI platform is not suitable for 785 nm wavelength as silicon absorbs heavily for wavelengths $< 1 \mu\text{m}$, so an alternative integration platform is required.

Silicon nitride (Si_3N_4) is another common material used in CMOS fabrication technology. It has a small absorption in the 500 nm – 2500 nm wavelength region, a moderately high refractive index $n_{\text{Si}_3\text{N}_4} = 1.8 - 2.2$, exhibits low fluorescence and is a very robust material capable of handling large optical powers [23] [24]. Thus Si_3N_4 waveguides [25] [26] defined on top of a silica undercladding constitutes a good trade-off for Raman spectroscopy at visible and near-infrared wavelengths, satisfying several technological constraints.

Si_3N_4 waveguide circuits discussed in this thesis are fabricated on 200 mm diameter silicon wafers with a thickness of 700 μm . A stack of 220 nm thick Si_3N_4 on top of 2.4 μm thick SiO_2 is deposited on top of the Si wafer. The Si_3N_4 as well as the SiO_2 are deposited by plasma enhanced chemical vapor deposition [25]. The waveguide structures are defined with 193 nm optical lithography and subsequently etched by fluorine based inductively coupled plasma reactive ion-etch process to get the final structure. Fig 1.1 shows the structure of a typical Si_3N_4 waveguide on a silica-on-silicon substrate.

Si_3N_4 platform is becoming a mature platform, and has been established as an alternative, medium-index-contrast material for integrated photonics. Indeed, all the essential components such as lasers [27], detectors, planar concave gratings [28], arrayed waveguide gratings [29], Mach-Zehnder interferometer filters [30] [31], ring cavity filters [32] and Bragg gratings [33] have been demonstrated using chip-scale nanophotonics. As for many other optical devices mentioned before, a Raman spectroscopic system may also be miniaturized and integrated on a chip. This is one of the goals of the research presented in this thesis. Other aims are discussed in the next section.

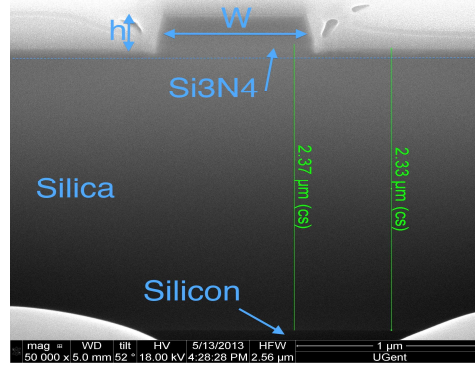


Fig. 1.1| Cross section view of Si_3N_4 waveguide discussed in this thesis. Typically we use $h = 220$ nm and $w = 700$ nm for strip waveguides. From [25].

1.4 Problem definition and research objective

The objective of the research presented in this thesis is to investigate:

1. Whether Raman spectroscopy is possible in the framework of integrated photonics.
2. The development of silicon nitride photonics platform for the visible-NIR region for the purpose.
3. Whether integrated Raman sensors are viable and to explore the possible fields of applications.
4. The quantification and comparative analysis with the existing systems such as confocal microscopes.
5. To identify and quantify the advantages and limitations of the waveguide approach.

1.5 Thesis outline

This thesis is structured as follows. In **Chapter 2** we briefly introduce the Raman scattering process and contrast its properties with other light-matter interaction phenomena. In that chapter we also discuss the collection efficiency of an ideal conventional Raman confocal microscope and identify its limitations. Subsequently, in **Chapter 3**, we explore the possibilities of the enhancement of Raman scattered signal coupled to an optical eigenmode by altering the environment of the light-matter interaction. We will particularly focus on planar waveguides and channel waveguides, described in general as an inhomogeneous environment with

1D and 2D symmetry respectively. In **Chapter 4** we will be concerned with theoretical and experimental explorations of the Raman spectroscopy of bulk material in the cladding using channel waveguides. In **Chapter 5** we demonstrate Raman spectroscopy of biological sub-monolayers functionalized on top of the waveguides and discuss few applications of the nanophotonic waveguide enhanced Raman spectroscopy (NWERS) of monolayers and thin layers. In the chapter we will also compare the NWERS results with a free-space approach for Raman spectroscopy. In **Chapter 6** we discuss different parameters on which the efficiency of the NWERS approach depends. Beginning with an empirical investigation on the origin of the waveguide background, in **Chapter 7**, we investigate the dependence of the waveguide background luminescence on several experimental variable and subsequently suggest some minimization and subtraction strategies. **Chapter 8**, the final chapter of this thesis, is dedicated to a short discussion about the possible directions that this research might develop towards.

1.6 Contributions and Publications

This work has led to following publications. Some proportion of the texts and figures in this thesis has been adapted from many of these published and submitted works. All conference contributions were presented orally except for the ones marked with an asterix (*).

International Journals

1. **A. Dhakal**, F. Peyskens, S. Clemmen, A. Raza, P. Wuytens, H Zhao, N. Le Thomas, R. Baets, "Single mode waveguide platform for spontaneous and surface-enhanced on-chip Raman spectroscopy", *Interface Focus*, (6) 20160015, (2016)
2. **A. Dhakal**, P. Wuytens, F. Peyskens, K. Jans, N. Le Thomas, R. Baets, "Nanophotonic waveguide enhanced Raman spectroscopy of biological submonolayers on a CMOS-compatible platform", Submitted (arXiv preprint: <http://arxiv.org/abs/1608.08002>)
3. F. Peyskens, **A. Dhakal**, P. Van Dorpe, N. Le Thomas, R. Baets, Surface Enhanced Raman Spectroscopy Using a Single Mode Nanophotonic-Plasmonic Platform, *ACS Photonics*, 3 (1), p.102-108 (2016)
4. **A. Dhakal**, A. Raza, F. Peyskens, A. Subramanian, S. Clemmen, N. Le Thomas, R. Baets, "Efficiency of evanescent excitation and collection of spontaneous Raman scattering near high index contrast channel waveguides", *Optics express*, 23 (21), p.27391-27404 (2015).
5. A. Subramanian, E.M.P. Ryckeboer, **A. Dhakal**, F. Peyskens, A. Malik, B. Kuyken, H. Zhao, S. Pathak, A. Ruocco, A. De Groote, P.C. Wuytens, D. Martens, F. Leo, W. Xie, U.D. Dave, M. Muneeb, Pol Van Dorpe, Joris Van Campenhout, W. Bogaerts, P. Bienstman, N. Le Thomas, D. Van Thourhout, Zeger Hens, G. Roelkens, R. Baets, "Silicon and silicon nitride photonic circuits for spectroscopic sensing on-a-chip", *Photonics Research* (invited), 5(3), p.B47 (2015)

6. H. Zhao, B. Kuyken, S. Clemmen, F. Leo, A. Subramanian, **A. Dhakal**, P. Helin, S. Simone, E. Brainis, G. Roelkens, R. Baets, "Visible-to-near-infrared octave spanning supercontinuum generation in a silicon nitride waveguide", *Optics Letters*, 40 (10), p.2177-2180 (2015)
7. F. Peyskens, A. Subramanian, P. Neutens, **A. Dhakal**, P. Van Dorpe, N. Le Thomas, R. Baets, "Bright and dark plasmon resonances of nanoplasmonic antennas evanescently coupled with a silicon nitride waveguide", *Optics Express*, 23(3), p.3088-3101 (2015)
8. **A. Dhakal**, A. Subramanian, P.C. Wuytens, F. Peyskens, N. Le Thomas, R. Baets, "Evanescent excitation and collection of spontaneous Raman spectra using silicon nitride nanophotonic waveguides", *Optics Letters*, 39 (13), p.4025-4028 (2014)
9. A. Subramanian, P. Neutens, **A. Dhakal**, R. Jansen, T. Claes, X. Rottenberg, F. Peyskens, S. Selvaraja, P. Helin, B. Du Bois, K. Leyssens, S. Severi, P. Deshpande, R. Baets, P. Van Dorpe, "Low-loss singlemode PECVD silicon nitride photonic wire waveguides for 532-900 nm wavelength window fabricated within a CMOS pilot line", *IEEE Photonics Journal*, 5 (6), p.2202809 (2013).
10. A. Subramanian, S. Selvaraja, P. Verheyen, **A. Dhakal**, K. Komorowska, R. Baets, "Near infrared grating couplers for silicon nitride photonic wires", *IEEE Photonics Technology Letters*, 24 (19), p.1700-1703 (2012)

International Conferences

1. **A. Dhakal**, A. Raza, P.C. Wuytens, F. Peyskens, A. Skirtach, R. Baets, "Lab-on-a-chip Raman sensors outperforming Raman microscopes", *CLEO 2016*, San Jose (2016).
2. F. Peyskens, **A. Dhakal**, P. Van Dorpe, N. Le Thomas, R. Baets, "Hybrid Single Mode Nanophotonic-Plasmonic Waveguides for On-Chip Surface Enhanced Raman Spectroscopy", accepted for publication in *META 2016*, Spain, (to be published).
3. F. Peyskens, **A. Dhakal**, P. Van Dorpe, N. Le Thomas, R. Baets, "Surface Enhanced Raman Spectroscopy on Single Mode Nanophotonic-Plasmonic Waveguides", *CLEO 2016*, San Jose (2016)
4. **A. Dhakal**, P.C. Wuytens, F. Peyskens, A. Subramanian, A. Skirtach, N. Le Thomas, R. Baets, "Nanophotonic Lab-On-A-Chip Raman Sensors: a Sensitivity Comparison with Confocal Raman Microscope", *BioPhotonics 2015*, Florence, p.Th6.3 (2015)
5. S. Clemmen, H. Zhao, F. Peyskens, **A. Dhakal**, P.C. Wuytens, A. Subramanian, N. Le Thomas, R. Baets, "Coherent anti-Stokes Raman spectroscopy on chip", 28th *IEEE Photonics Conference (IPC 2015)*, United States, p.623-624 (2015)
6. D. Delbeke, A. Subramanian, P. Cardile, W. Woestenborghs, A. Ruocco, J.W. Hoste, D. Martens, **A. Dhakal**, P. Bienstman, G. Roelkens, N. Le Thomas, R. Baets, "Silicon photonics for on-chip spectrophotometry", *12th International Conference on GPF (invited)*, United States, p.FC1(2015).

7. **A. Dhakal**, F. Peyskens, A. Subramanian, N. Le Thomas, R. Baets, Enhanced Spontaneous Raman Signal Collected Evanescently by Silicon Nitride Slot Waveguides, *CLEO: 2015*, United States, p.paper STh4H.3 (2015).
8. R. Baets, A. Subramanian, **A. Dhakal**, F. Peyskens, P.C. Wuytens, E.M.P. Ryckeboer, G. Roelkens, N. Le Thomas, Spectroscopic sensing enabled by silicon photonics, *Asia Communications and Photonics Conference (ACP) (invited)*, China (2014).
9. R. Baets, **A. Dhakal**, F. Peyskens, P.C. Wuytens, A. Skirtach, N. Le Thomas, A. Subramanian, "Resonant enhancement mechanisms in lab-on-chip raman spectroscopy on a silicon nitride waveguide platform", *IEEE Photonics Conference 2014 (IPC) (invited)*, United States, p.500-501(2014).
10. **A. Dhakal**, P.C. Wuytens, F. Peyskens, A. Subramanian, N. Le Thomas, R. Baets, "Evanescent Raman spectroscopy using photonic waveguides", *International Conference on Raman Spectroscopy- ICORS 2014*, Germany, p.WeA-O-006(2014).
11. F. Peyskens, A. Subramanian, P. Neutens, **A. Dhakal**, P.C. Wuytens, P. Van Dorpe, N. Le Thomas, R. Baets, "Enhancement of Raman scattering efficiency by on-chip nanoplasmonic antennas", *Surface-Enhanced Spectroscopies*, Germany, (2014)
12. **A. Dhakal**, P.C. Wuytens, F. Peyskens, A. Subramanian, N. Le Thomas, R. Baets, "Silicon-nitride waveguides for on-chip Raman spectroscopy", *SPIE Photonics Europe 14* (2014)
13. P. Neutens, A. Subramanian, M. Ul Hassan, C. Chen, R. Jansen, T. Claes, X. Rottenberg, B. Du Bois, K. Leyssens, P. Helin, S. Severi, **A. Dhakal**, F. Peyskens, L. Lagae, P. Deshpande, R. Baets, P. Van Dorpe, "Characterization of PECVD silicon nitride photonic components at 532 and 900 nm wavelength", 4th Conference on *Silicon Photonics and Photonic Integrated Circuits*, Belgium, p.article 91331F (6 pages) (2014)
14. **A. Dhakal**, P.C. Wuytens, F. Peyskens, A. Subramanian, N. Le Thomas, R. Baets, "Raman spectroscopy using photonic waveguides", *IPS Benelux 2013*, Netherlands, (2013)
15. N. Le Thomas, **A. Dhakal**, F. Peyskens, A. Subramanian, T. Claes, K. De Vos, E.M.P. Ryckeboer, R. Bockstaele, P. Bienstman, R. Baets, "Biological sensing with integrated silicon and silicon nitride photonics", *The 2nd BioPhotonics Conference (invited)*, Taiwan, p.28-29(2013)
16. **A. Dhakal**, F. Peyskens, A. Subramanian, N. Le Thomas, R. Baets, "Enhancement of light absorption, scattering and emission in high index contrast waveguides", *OSA-Advanced Photonics Congress, Optical Sensors*, United States, p.ST2B.5 (2013)
17. F. Peyskens, A. Subramanian, **A. Dhakal**, N. Le Thomas, R. Baets, "Enhancement of Raman Scattering Efficiency by a Metallic Nano-antenna on Top of a High Index Contrast Waveguide", *CLEO 2013*, United States, p.paper CM2F.5 (2013)
18. R. Baets, A. Subramanian, **A. Dhakal**, S. Selvaraja, K. Komorowska, F. Peyskens, E.M.P. Ryckeboer, N.A. Yebo, G. Roelkens, N. Le Thomas, Spectroscopy-on-chip applications of silicon photonics, *Photonics West (invited)*, 8627(01), United States, p.86270I-1 - 86270I-10 (2013).

19. A. Subramanian, S. Selvaraja, **A. Dhakal**, K. Komorowska, R. Baets, "Grating couplers for Si₃N₄ waveguides at 900 nm", *16th European Conference on Integrated Optics (ECIO 2012)*, Spain, p. paper 182(2012).
20. ***A. Dhakal**, A. Subramanian, N. Le Thomas, R. Baets, "The role of index contrast in the efficiency of absorption and emission of a luminescent particle near a slab waveguide", *16th European Conference on Integrated Optics (ECIO 2012)*, Spain, p. paper 131(2012).

2

A brief review of light-matter interaction and Raman spectroscopy

In this chapter, the classical theory of radiation and light-matter interaction is introduced. The Raman scattering process, which is our major concern in this thesis, can be modelled in a simplistic manner from the classical theory. The theory developed in the chapter is sufficient to understand the work presented in this thesis. For a detailed and complete analysis of Raman scattering process, a quantum theory is needed. The readers are referred to excellent text books by Loudon [34], Novotny [35], Long [2] and Jackson [36] for a detailed and in-depth treatment of the topic. Some texts and figures in this chapter have been adapted from some of my published articles [1] [37].

2.1 Classical description of light-matter interaction

In a large majority of classical light-matter interaction problems, matter is modeled as a collection of electrical dipoles. An electrical dipole is a pair of oppositely charged particles separated by a small distance, potentially oscillating with one or several orthonormal modes of vibrations. An incoming light is modeled as an oscillating electromagnetic field with the electric field $\vec{E} = \vec{E}_0 e^{i\omega_0 t} + cc$. The oscillating field would then drive the oscillation of the dipoles, which in turn re-radiates the power into the environment according to the normal modes that are excited. At the molecular level, such a polarization is described by an induced

local dipole moment \vec{d} , which is a function of the incoming oscillating field \vec{E} and a material dependent quantity called polarizability α . In general α can have a non-linear tensorial form. But for the purposes of this thesis we make a linear and isotropic approximation, such that polarizability can be considered a scalar and the induced dipole moment can be described in the following form:

$$\vec{d} = \alpha \vec{E} \quad (2.1)$$

The polarizability of a molecule α is dependent on the molecular properties such as the distribution of charges in the molecule, and the frequency of the resonance of the normal vibrational modes that the molecular charges are subject to. Polarizability increases if the electrons are loosely bound to the nuclei. In general, larger molecules have more loosely held electrons in comparison to smaller molecules with the electrons tightly bound to the nuclei. In case of atoms in the periodic table for example, polarizability increases from right to left and from top to bottom of the periodic table. The dominant component of polarizability, which is called the static polarizability α_0 , is dependent on the average charge distribution, and it can be described by an average normal coordinate Q_j^0 . However, the polarizability also has a dynamic component described by a set of normal coordinates Q_j corresponding to each normal modes j of the molecular vibrations. The normal coordinates Q_j and the corresponding angular frequency ω_j are related such that $Q_j = Q_j^0 e^{-i\omega_j t} + cc$. The total polarizability α can thus be decomposed into the static and dynamic components as follows,

$$\alpha = \alpha_0 + \sum_j \left(\frac{\partial \alpha}{\partial Q_j} \right) Q_j + .. \quad (2.2)$$

2.2 Scattering processes

Here, we outline a simplified picture of Raman, Rayleigh and Brillouin scattering based on dipole radiation and dynamic polarizability described in the previous section. A detailed classical treatment of Raman scattering can be found in [2] and a quantum mechanical description of Raman scattering or light-matter interaction in general can be found in [34], [36].

Ignoring higher order terms, Eq. (2.1) and Eq. (2.2) yields,

$$\begin{aligned} \vec{d} &= \alpha_0 \vec{E} + \vec{E}_0 \sum_j \left(\frac{\partial \alpha}{\partial Q_j} \right) Q_j^0 [e^{-i(\omega_0 - \omega_j)t} + e^{-i(\omega_0 + \omega_j)t}] + cc \\ &= \vec{d}_{(\omega_0)} + \vec{d}_{(\omega_0 - \omega_j)} + \vec{d}_{(\omega_0 + \omega_j)} \end{aligned} \quad (2.3)$$

Eq. (2.3) suggests that the induced dipole oscillates at three frequencies, one corresponding to the incident light ω_0 and the other two at frequencies $\omega_0 \pm \omega_j$ corresponding to the incident light modulated by each of the molecular vibrational modes j for which $\partial\alpha/\partial Q_j \neq 0$. Since a dipole oscillating at a frequency ω radiates at the same frequency, the scattered or re-radiated light has the same frequencies as that of the induced dipole oscillation. The total time-average power radiated by a dipole of strength \vec{d} is proportional to $|\vec{d}|^2$ (given by Eq. (A.7) in Appendix A). Hence, for each dipole term in Eq. (2.10) respectively yields powers P_{RY} , P_{ST} and P_{AS} :

$$P_{scat} = P_{RY}(\omega_0) + P_{ST}(\omega_0 - \omega_j) + P_{AS}(\omega_0 + \omega_j) \quad (2.4)$$

2.2.1 Rayleigh scattering

In Eq. (2.4) the power P_{RY} corresponding to the elastic scattering of light, i.e. the scattering conserving the frequency of the incident light ω_0 is called **Rayleigh scattering**. Since it is dependent only on the strongest static polarizability, it is the strongest component in the light scattered by the molecule. In the absence of absorption (or absence of resonance, i.e. $\omega \neq \omega_0$), Rayleigh scattering is in phase with the incident field in the forward direction. Thus, for a medium with some significant degree of molecular order, the first term in Eq. (2.4) is responsible for the forward propagation of light. However, in reality, there also exists a considerable degree of disorder among the positions of the molecules depending on the amorphosity, thermal properties and the temperature. The random positioning of the scattering molecules with respect to an arbitrary location leads to an incoherent addition of scattered light at that location. For a collection of molecules, this incoherent collection of scattered light at an arbitrary position is historically called Rayleigh scattered light, and the in-phase component of forward propagating light originating from the first term of Eq. (2.4) is just termed as the forward propagating or transmitted light. Nevertheless, the process of light propagation in the medium and Rayleigh scattering is governed by the same static polarizability.

2.2.2 Raman scattering

The inelastic component of scattered light described by second and third terms of Eq. (2.4), i.e. the scattering where the light exchanges its energy with the molecules thereby changing the frequency, is called **Raman scattering**. For each molecular vibration yielding Raman scattering, there are positive (third term in Eq. 2.4) and negative frequency shifts (second term in Eq. 2.4). Raman scattering where the scattered light gains energy from the molecules, thereby manifesting with larger frequency, is called **anti-Stokes Raman scattering**. The opposite case where the light loses energy is called **Stokes Raman scattering**. In a state of

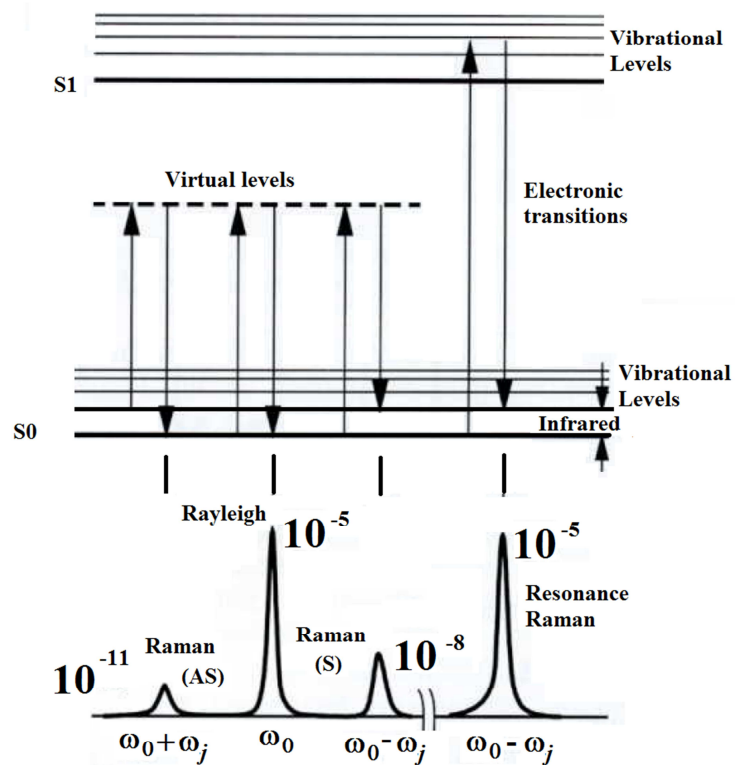


Fig. 2.1] Raman Stokes (S), anti-Stokes (AS), resonance Raman and Rayleigh scattering depicted in terms of transitions between a virtual state and the vibrational states. In case of Rayleigh scattering there is no exchange of energy between the molecule and the light as the initial and final vibrational states are the same, hence, incident and scattered photons have the same frequency ω_0 . In case of Stokes Raman scattering the molecule absorbs energy from the light hence has less frequency compared to the incident photon and in case of anti-Stokes Raman scattering molecule loses energy, hence the scattered photon has more energy than the incident photon. Their approximate relative intensities in the units of incident intensity are also shown. The states S0 and S1 are electronic states; hence usually have high transition energy (in visible and UV frequency region).

thermal equilibrium, the population of the molecules occupying the excited state is smaller than the population of the molecules in the ground state by the Boltzmann factor, $\exp\left(-\frac{\hbar\omega}{k_B T}\right)$. Hence the intensity of anti-Stokes light is smaller than the Stokes light by this factor. The phase of Raman scattering is dependent on the phase of the individual molecular vibrations, which are vibrating incoherently, hence spontaneous Raman emission described by second and third terms of Eq. (2.4) have arbitrary phase relative to each other, and thus incoherent. This is in contrast to Rayleigh scattering, where incoherence in the scattered light is due to random position of the emitters rather than the randomness in the phase of the vibrations of the molecules.

Fig. 2.1 illustrates Stokes and anti-Stokes Raman light, and Rayleigh scattered light and their relative intensities. At room temperature Rayleigh, anti-Stokes and Stokes scattered intensities are in the order of 10^{-5} , 10^{-11} , 10^{-8} respectively normalized to the incident intensity. These numbers are typical for the Stokes shift in the order of ~ 0.3 eV (~ 2500 cm^{-1}). The intensity of anti-Stokes with respect to the Stokes, however, depends on the Boltzmann factor i.e. reduces exponentially with the ω_j/T . The corresponding quantum mechanical picture in terms of energy levels is also illustrated in Fig 2.1. In a quantum mechanical model, the Raman scattering process is described as the scattering between two bosonic particles photons and *phonons*, the quanta of molecular vibrations. In essence, this is annihilation (or absorption) of a phonon and subsequent creation (emission) of a photon via an intermediate non-resonant virtual quantum state of a material. As a result, the frequency of emitted photons is shifted by the amount corresponding to the energy of the phonons which are annihilated. In case of anti-stokes, the phonons are created at the expense of the energy of the photons.

When an intermediate state is nearby a resonant electronic state, the corresponding Raman scattering process is called **Resonant Raman scattering**. Resonant Raman scattering is distinguished from ordinary Raman scattering for the excitation wavelengths at or very close to the electronic resonant wavelengths. Such a scattering leads to an enhanced intensity, which unfortunately, also comes with a significant amount of fluorescence (§2.5) that forms a strong background in the measurement of the Raman signal.

2.2.3 Brillouin scattering

So far we have implicitly qualified the applicability of Eq. (2.4) to the molecular vibrations in the optical frequencies (i.e. > 10 THz) with high energy vibrational modes of the molecules. The normal modes Q_i corresponding to these vibrations are called *optical normal modes* (the corresponding quantum particles are called optical phonons) as their energies correspond to the optical light at the mid-infrared (MIR) wavelengths. However, a similar analysis can be applied to

the cases of *acoustic normal modes* where the large scale collective vibrations of the molecules in acoustic frequencies (i.e. < 1 THz) are of concern. The scattering corresponding to the polarizations due to molecular vibrations in acoustic frequencies is called **Brillouin scattering**. The low energy acoustical vibrations relates to the collective oscillations of ions (where they move together). This is in contrast to the optical vibrational modes where the ions swing independently. Brillouin scattering is distinguished from Raman scattering as the scattered signal does not reveal the internal ionic structure of the molecules but relates to the large scale vibrations of a collection of molecules. A detailed description, references and its analysis in context of integrated photonics can be found in Raphaël Van Laer's PhD thesis [109].

2.3 Various definitions of scattering cross sections

Using definition of wave numbers, $\nu = \omega/(2\pi c)$, the power P emitted by a dipole \vec{d} oscillating at frequency ω is given by following equation (see §Appendix A for details, follows from (A.11)):

$$P = n \frac{2\pi^3 c}{\varepsilon_0} \nu^4 |\vec{d}|^2 \quad (2.5)$$

The intensity of incident light I_0 , assuming that it is a plane wave in a free space, is given by the following equation:

$$I_0 = \frac{c\varepsilon_0}{2n} |\vec{E}|^2 \quad (2.6)$$

It is useful to define a quantity σ_{tot} defined as the ratio of average scattered power per molecule scattered in all space for a given pump intensity I_0 . Assuming the molecules lie in a homogenous free-space medium, and a scalar polarizability (hence the dipole to be in the same direction as that of the incoming field \vec{E}), we can write,

$$\sigma_{tot} = \frac{\langle P \rangle}{I_0} = 4\pi k_\nu \nu^4 \alpha^2 \quad (2.7)$$

with $k_\nu = \pi^2/\varepsilon_0^2 = 1.26 \cdot 10^{23} \text{C}^{-2} \text{V}^2 \text{m}^2$ as a constant for conversion. σ_{tot} is more precisely called the **total scattering cross-section**, also just referred to as the scattering *cross-section* in the literature. The scattering cross-section σ_{tot} is a function of the average polarizability of an ensemble of molecules and the wavenumber of incident light. It is a quantity directly measured in most of the experiments and has $\text{m}^2 \text{molecule}^{-1}$ as its SI unit.

In many situations one is concerned with different pump frequencies (hence different absolute Stokes frequencies), in such cases σ_{tot} is an inconvenient quantity as it is function of absolute wavenumbers. The power $P_{d\Omega}$ scattered by a

molecule towards a given direction in a given solid angle $d\Omega$ is dependent on the electronic configurations and orientations of the constituent atoms. It is dependent on the so called *Placzek polarizability tensor* [2], which in general depends on the direction relative to a particular molecular orientation and is independent of the wavelength. Hence it is convenient to define the **wavenumber-normalized scattering cross-section** σ_{norm} defined as:

$$\sigma_{norm} = \nu^{-4} \left(\frac{1}{I_0} \frac{d}{d\Omega} P_{d\Omega} \right) = \nu^{-4} \left(\frac{d}{d\Omega} \sigma_{tot} \right) = k_v \alpha^2 \quad (2.8)$$

Here the last step is valid only for the scalar polarizability. Wavenumber-normalized scattering cross-section σ_{norm} is usually tabulated as β_0 in the literature and is typically used in theoretical estimations of cross-section and for measurements with crystalline materials. It has SI units of $m^6 sr^{-1} molecule^{-1}$.

In Eq.(2.8) the bracketed term is another common definition of cross-section called **differential cross-section** σ_{diff} [2] usually tabulated as $d\sigma/d\Omega$ in the literature. For an ensemble of randomly oriented molecules, as we mostly deal in this thesis, the emission is isotropic, hence, in such cases

$$\sigma_{diff} = \frac{d\sigma_{tot}}{d\Omega} = \frac{\sigma_{tot}}{4\pi} = k_v \nu^4 \alpha^2 \quad (2.9)$$

This definition of cross-section is handy for calculations bridging theoretical calculations and experiments, and used extensively in the literature referring to it just as *cross-section*, any ambiguity with the total scattering cross-section is resolved by its unit $m^2 sr^{-1} molecule^{-1}$. We follow the same convenience in this thesis and use the symbol σ for differential cross-section, without any subscript label for qualification, unless we need to make an explicit differentiation.

2.4 Fluorescence

If the frequency of an incoming light is near an electronic transition resonance of a molecule (characterized with a transition energy > 1.5 eV in contrast to low energy < 1 eV molecular vibrations), the total polarizability of the molecule is changed due to the rearrangement of the electron cloud in the resonance. This leads to the absorption of the incoming light and a net change in dipole moment. Some part of the absorbed energy is non-radiatively dissipated by the molecules during collisions and internal vibrionic transitions. The remaining absorbed energy is mostly reradiated with reduced frequency (Stokes shift) in the form of emission called *fluorescence*.

In a quantum mechanical description, as depicted in Fig. 2.1, the molecule makes a transition to a high energy electronic state upon absorption of the resonant light. This is in contrast to the Raman scattering process where a non-resonant

virtual state is involved. It is also different compared to infrared absorption (see further §2.5), as an electronic rather than a vibrational transition is involved. Since real electronic states are involved in the transition, there is a large probability that the molecule makes subsequent transitions to nearby vibrionic or electronic states before radiating away the remaining energy with a delay. Hence, other essential properties of fluorescence are non-radiative dissipation of some part of the absorbed energy, and a characteristic delay that is in the order of nano-seconds, as the molecule makes transitions to the nearby electronic states. In contrast, as it involves a virtual state, Raman scattering is almost an instantaneous process (\sim pico-seconds [110]) and the transition to lower vibrionic state is made without an intermediate loss of the energy to non-radiative pathways. Fluorescence is quite stronger than Raman scattering as it directly involves the resonant electronic transitions that strongly influence the polarizability of the molecules.

In case of fluorescence, it is instructive to relate the power of the light absorbed or emitted by the molecules with the change in the dipole moment of the molecule corresponding to the electronic transition. This leads to the following relationship for fluorescence cross-section with the net dipole moment (\vec{d}) and electronic state U_i [7] :

$$\sigma_{flr} \propto \left(\frac{\partial \vec{d}}{\partial U_i} \right)^2 \Big|_{U_i^0} \quad (2.10)$$

2.5 Infrared Absorption

The application of the classical Eq. (2.3) is not valid for $\omega_0 \leq \omega_i$ because α is not a non-zero smooth function of the normal coordinates in this frequency region. There is no simple classical explanation for this. However, in quantum-mechanics the condition $\omega_0 < \omega_i$ corresponds to the cases where the incident photons have less energy than the quanta of the energy of the molecular vibrations. Hence the photons are not able to efficiently exchange the energy with the molecules. At resonance, i.e. when $\omega_0 = \omega_i$, the energy exchange leads to a net change in the dipole moment due to change in the vibrational states, just like in the case of electronic absorption leading to fluorescence described by Eq. (2.10). Thus, in the case of infrared absorption too, it is helpful to relate the power of the light absorbed by the molecules P_{IR} with the change in the dipole moment of the molecule corresponding to each normal coordinate [6] :

$$\sigma_{IR} \propto \left(\frac{\partial \vec{d}}{\partial Q_j} \Big|_{Q_j^0} \right)^2 \quad (2.11)$$

2.5.1 Mutual Exclusion

Eq. (2.11) is to be contrasted with the case of Eq. (2.3) for Raman scattering where the changes in the dynamic component of the polarizability (due to the molecular vibration) indirectly modulates the dipole moment of the molecule. Whereas, in case of IR absorption the rearrangement of molecular orbitals lead to a net change in the static polarizability of the molecules. Further, not all normal modes lead to a net change in the polarization. Molecular vibrations symmetric with respect to a point, such as symmetrical stretch vibration (Fig. 2.2), do not lead to any net change in the dipole moment and can only exhibit Raman scattering as will be explained next. In a similar manner, molecular vibrations which are antisymmetric to the center of symmetry, such as antisymmetric stretch or bend, do not lead to a strong change in polarizability, hence do not exhibit Raman peaks (Fig. 2.2). The complementary and mutually exclusive nature of Raman scattering and infrared absorption with regard to the symmetry of vibration about the point of symmetry means a combination of the two techniques is needed for the most detailed study of the molecular vibrations.

2.5.2 Infrared Absorption spectroscopy

As discussed before, the resonant energy of the optical normal modes of molecular vibrations ω_0 corresponds to the energy of light at the MIR wavelengths. Thus, an alternative way to get the information about these modes of vibrations is to directly excite the molecular vibration with a MIR light with the corresponding resonant excitation frequency. Incoherent reemission in the surrounding and dissipation of the resonantly absorbed light as heat causes a significant extinction of the incident light. The extinction of the light can be measured and information relating to the corresponding vibrational modes of the molecules can be obtained. Such a technique of molecular spectroscopy is a well-established and popular spectroscopic technique called *infrared (absorption) spectroscopy*. There are several advantages of this techniques. The major advantage is relatively high absorption cross-section of substances. The other advantage is the simplicity in the measurement setup as precision filters are not needed. Unfortunately, there are several problems associated with infrared spectroscopy as discussed below [6].

2.5.3 Problems with IR spectroscopy

1. Lack of cheap lasers that works in the IR band ($2\ \mu\text{m}$ - $10\ \mu\text{m}$). Furthermore, it requires broadband or tunable IR source, which in general, is expensive.
2. All the three vibrational modes of water are IR active hence IR light is strongly absorbed by water. Consequently, IR spectroscopy is not suitable

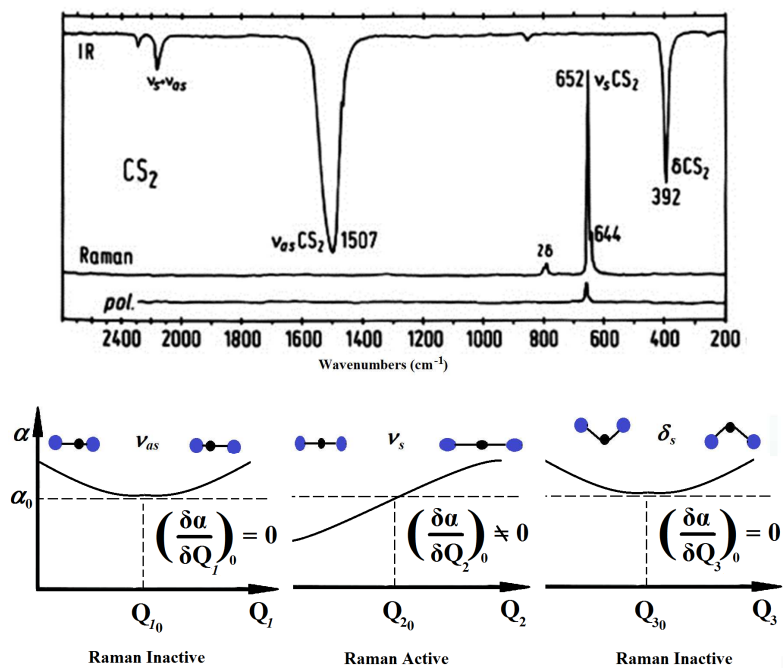


Fig 2.2 Symmetric vibrational modes lead to strong change in polarizability near the average molecular position. No changes of the polarizability ($\delta\alpha/\delta Q = 0$) as in asymmetric vibrations lead to Raman inactive but IR active modes. Here this is exemplified by asymmetric stretch ν_{as} (IR active, Raman inactive), symmetric stretch ν_s (Raman Active, IR inactive) and symmetric bend δ_s (IR Active, Raman active) modes of vibrations of CS₂ (based on Michael K. Denk, Vibrational Spectroscopy online lectures).

for aqueous samples. Interference from atmospheric water and trace water in samples or containers are also regular problems in the IR measurement.

3. Absorption of light heats the sample and therefore may potentially lead to sample damage.
4. Mid-IR light is not transparent to many common optical materials, thus restricting sampling flexibility. A total penetration of the light through the sample is usually needed to determine the absorption, except for cases where a sophisticated attenuated total reflection (ATR) spectroscopy is used by exploiting attenuation due to evanescent tail of the light.
5. To minimize the interference from optics and containers itself, IR spectroscopy requires special and costly optics.
6. Long wavelength used in IR absorption renders spatial resolution worse.

2.6 Characteristics of spontaneous Raman scattering

Based on the discussions in the previous sections, we can derive several conclusions about the characteristics of the Raman scattering process on its utility and limitations. These are enumerated as follows.

1. From Eq.(2.2), it can be concluded that Raman scattering is exhibited only by the vibrations that change the polarizability i.e. which $\partial\alpha/\partial Q_j \neq 0$. Usually the symmetrical vibrations exhibit strong Raman signal. The Raman signal corresponding to the asymmetric stretches and bends are weak.
2. It follows from Eq.(2.3) and Eq.(2.5) that Raman scattering is a linear process with respect to the intensity of the incident field or power of the incoming light.
3. Raman scattering can be described by an effective dipole moment as in Eq.(2.2). Thus a conclusion derived for a dipole radiation problem can be applied to Raman scattering problem. It is an important conclusion as it means that several enhancement mechanisms, such as cavity enhancements or enhancement by heterogeneous media, generally developed to describe enhancement of dipole radiation can be used to study the enhancement of Raman signal. This will be of our concern in the next chapter.
4. From Eq.(2.2) it can be seen that one strong pump at frequency ω_0 is sufficient to produce a Raman spectrum corresponding to several vibrionic states with energies almost up to the pump frequency ω_0 . Since the vibrational

energies are less than 1eV, usually a visible or near-infrared light can be used to obtain all the essential Raman signals. This also means that well-established techniques developed for visible microscopy and imaging can be used for Raman spectroscopy. This is in sharp distinction with the IR spectroscopy which either requires a broadband or a tunable source in the infrared band.

5. Raman scattering is a non-resonant process, hence the cross-section is much weaker compared to infrared absorption or fluorescence. This is a critical drawback of the Raman scattering process, and leads to an extremely low sensitivity of the Raman signal compared to the signal from fluorescence or IR absorption.
6. The signal-to-noise ratio for Raman systems are very low because of the shot noise from competing processes like fluorescence, in addition to weak nature of the Rmana scattering process (discussed further in Appendix B).

2.7 Efficiency of Raman scattering in an ideal free-space system

When deriving Eq. (2.7) we assumed an electromagnetic plane wave impinging on an ensemble of molecules lying uniformly in a medium. However, any realistic light beam is subject to diffraction. Here, the efficiency of excitation and collection of a Raman signal using an ideal diffraction-limited beam employing a dispersionless (and lossless) free-space optical system is described. We choose a diffraction-limited beam, the fundamental Gaussian mode in free-space, in our analysis because it ensures minimum possible étendue for Raman microscopes. Minimum étendue warrants maximal power density for maximal excitation, hence serves as the best case scenario for the free space excitation and collection. Further, smallest étendue is required to have small spectrometer, high resolution and high power density at the detector (explained in Appendix D). For the scattering problem we are concerned with, we consider the beam profile at the beam waist where the field intensity $I_g(\vec{r})$ is maximal to excite a particle and assume that the numerical aperture of the optics $NA = 1$, corresponding to the most ideal situation in the free-space. The total power of light scattered by the particle in all directions at an arbitrary location \vec{r} of the beam within the beam waist w_0 is given by,

$$P_{DL,0}(\vec{r}) = \sigma_{tot} I_g(\vec{r}) = 4\pi\sigma_{diff} \frac{P_{pump}}{\pi w_0^2} |\vec{e}_g(\vec{r})|^2 \quad (2.12)$$

Here, $|\vec{e}_g|^2$ is the well-known normalized Gaussian beam profile given by $\exp(-(2r^2)/w_0^2)$ for the fundamental Gaussian mode with a waist $w_0 = \lambda_0/\pi$ (we assume, $NA = 1$) [38]. The scattering efficiency is then,

$$\frac{P_{DL,0}}{P_{pump}} = 4\pi\sigma_{diff} \frac{|\vec{e}_g(\vec{r})|^2}{\pi w_0^2} = \sigma_{diff} \left(\frac{4\pi^2 |\vec{e}_g(\vec{r})|^2}{\lambda_0^2} \right) = \Lambda_{DL}\sigma_{diff} \quad (2.13)$$

Here, following the terminology used in particle scattering theory [39], we have defined a cross-section independent parameter for the diffraction-limited beam, called *integrated luminosity* for the free-space Λ_{DL} . Integrated luminosity for a diffraction limited beam (with $NA = 1$), Λ_{DL} is given by the term in the brackets in Eq. 2.13. This quantity will be handy in the next chapter to compare scattering efficiencies for various systems (Table 3.1).

2.7.1 Collection efficiency for bulk sensing

The intensity of a diffraction-limited beam reduces as $1/(1+(z/z_R)^2)$ with the distance z away from the beam waist, where $z_R = w_0/\theta$ is the Rayleigh range of the beam for a beam divergence θ and beam waist w_0 . The excitation intensity reduces by more than half the amount for the sample volume away from the range Rayleigh range. Hence, in case of confocal microscopes employing diffraction limited excitation and collection, the collected signal essentially originates from particles located in the confocal volume, i.e. within the depth-of-focus $2z_R$. Further, only the emission inside a solid angle Ω corresponding to a half-acceptance angle θ (Fig 2.3) of the collection optics is collected. We assume that the collection optics has the same acceptance width (slit width of the spectrometer) as the $1/e^2$ width of the exciting beam. Then, in terms of differential scattering cross-section σ and the density of the particles ρ , the overall efficiency of excitation and collection can then be calculated as [37], [40]

$$\frac{P_{DL,Bulk}}{P_{pump}} = 2z_R\Omega\sigma\rho \quad (2.14)$$

Assuming a small beam divergence, $\theta = w_0/z_R = \lambda_0/(n\pi w_0)$, the solid angle can be expressed in terms of the parameters of the diffraction-limited beam:

$$\Omega = 4\pi \sin^2\left(\frac{\theta}{2}\right) \approx \pi \left(\frac{w_0}{z_R}\right)^2 = \frac{\lambda_0}{nz_R} \quad (2.15)$$

Hence,

$$\frac{P_{DL,Bulk}}{P_{pump}} = 2 \left(\frac{\lambda_0}{n}\right) \sigma\rho \quad (2.16)$$

Note that the SI unit for solid angle steradian (sr) is implicit in the pre-factor of Eq. (2.16). The approximation carried out in Eq. (2.15) overestimates the solid angle, as in general, $w_0/z_R > \sin(\theta)$. Hence, Eq. (2.16) sets the upper-limit for the confocal microscopic systems. Microscopes with higher transmission

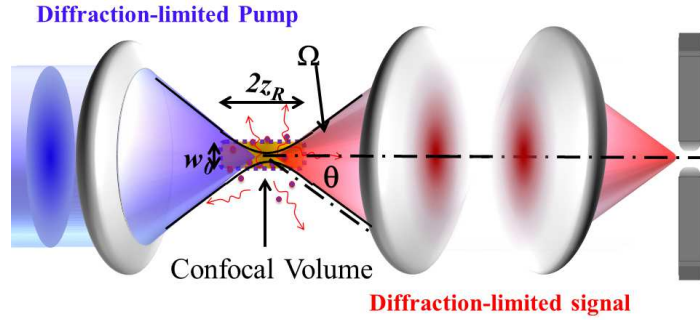


Fig. 2.3 Schematic of the beam geometry for a confocal microscope. Only signal from confocal volume contributes significantly to the signal. The aperture size of the collection optics is assumed to be the same as that of the size of the excitation beam. A slit is usually present in the collection Fourier plane to collect signal exclusively from the confocal volume.

losses and having larger divergence than diffraction-limited systems behave worse. Eq. (2.16) is independent of any system-specific parameters such as numerical aperture or focal length. It reveals the opposite effects due to the beam divergence and the depth of focus, which restricts the detection volume and field intensity, hence, the collected power [37]. In chapter 3, we describe the use of dielectric waveguides to overcome the limit imposed by diffraction by means of waveguiding and electromagnetic confinement.

2.7.2 Collection efficiency for surface sensing

For a monolayer or a very thin layer of molecules with surface density ρ_s when excited and collected by a diffraction limited free-space system, the interaction area is limited by the beam waist. Integrating Eq. (2.12) within the beam waist, the power emitted *in every direction* when excited by a diffraction-limited beam is given by, $P_{DL,s} = \sigma \rho_s P_{pump}$. Thus for collection using $NA = 1$, which collects all the light from the half-space,

$$\frac{P_{DL,S}}{P_{pump}} = \frac{1}{2} \sigma \rho_s \quad (2.17)$$

Just like Eq. (2.16) sets an upper limit for the bulk collection, Eq. (2.17) sets an upper limit in the collection of a Raman signal from a monolayer of molecules using a free-space system. As in the case of Eq. (2.16), the ideal excitation and collection in a free-space system is independent of the system dependent parameters such as focal length of the focusing lens (beam waist) because of the opposing effects of divergence and sampling area. In Chapter 4 we will compare this value

limited by the diffraction with a realistic waveguide system that overcomes the diffraction by means of electromagnetic confinement, which leads to waveguiding and enhancement.

2.8 Closing Remarks

In this chapter we discussed several aspects of light-matter interaction relevant to Raman spectroscopy in a homogenous medium. In particular we introduced Raman scattering and distinguished it from other forms of light matter interactions. Further, we developed an upper-limit case for the generic free-space Raman excitation and collection system. We shall refer to several equations and conclusions developed in this chapter in later chapters.

3

Enhancement of spontaneous scattering by optical confinement

In Chapter 2 we discussed that spontaneous Raman scattering is a non-resonant process, and therefore it is an extremely weak process. In this chapter we explore the possibility of enhancing the Raman scattering rate by changing the boundary conditions of the environment. Before mid-1940s the radiated power of a dipole, as given by Eq. (2.5), was thought to be a sufficient description for the classical dipole emission. Even during the development of quantum mechanics, the spontaneous emission rate of excited molecules was assumed to be intrinsic to the molecules. In the context of nuclear magnetic resonance, in 1946 E. M. Purcell suggested [41] that the spontaneous emission rate is strongly influenced by the electromagnetic environment. Specifically, he proposed that for an emitter coupled to a resonant mode of a cavity, the spontaneous emission rate is modified by the properties of the cavity. Subsequently, the idea has been applied in a variety of practical problems to enhance or inhibit emissions, such as fluorescence [42]. In this chapter we look at the modification of the emission depending on the boundary conditions of the environment of an emitter. Although the problem has a quantum-mechanical root, we will limit ourselves to the classical description. As we shall see in this chapter, the enhancement of emission in an inhomogeneous medium including Purcell's original equation for a cavity can be derived classically.

3.1 Classical description of enhancement of emission

In appendix A we show that the enhancement and inhibition of emission in an inhomogeneous medium is governed by the local density of states (LDOS). In the context of classical electromagnetic modes, LDOS $D(\vec{r}, \omega)$ is defined as the number of available modes at a given position \vec{r} per unit frequency per unit volume. Then, the emitted power P for a dipole \vec{d} in an inhomogeneous medium is given by (see Appendix A for details):

$$P = \frac{\pi\omega^2}{4\epsilon\epsilon_0} |\vec{d}|^2 D(\vec{r}_0, \omega_0) \quad (3.1)$$

In many practical situations we can exploit a symmetry present in the environment and the LDOS can be calculated by counting the number of states in k -space (Fig. 3.1), as only certain values of k lead to a valid wave solution in a given volume V . For example, in an isotropic homogenous medium with refractive index n , the dispersion is given by $dk/d\omega = v_g = c/n$, hence the LDOS can be calculated as follows,

$$D_0(\omega) = \frac{1}{V} \frac{dN}{d\omega} = \frac{2}{V} \frac{4\pi |k|^2 dk}{(2\pi/l)^3 d\omega} = \frac{\omega^2 n^3}{\pi^2 c^3} = \frac{k^2 n}{\pi^2 c} \quad (3.2)$$

Here an arbitrary length l defines a cube of volume V . The prefactor 2 takes the two possible transverse polarization modes of the field into account. It is instructive to introduce the so called *total density of states* for the homogeneous medium given by $D_f(\omega) = D_0(\omega)/3$ which is an average over the three possible dipole orientations along the three possible orthonormal spatial orientations. Hence, the emission of a dipole in an inhomogeneous environment, normalized to the emission in a homogeneous medium, is given by,

$$\frac{P(\vec{r}_0, \omega_0)}{P_0} = \frac{D(\vec{r}_0, \omega_0)}{D_f(\omega_0)} = 3 \frac{D(\vec{r}_0, \omega_0)}{D_0(\omega_0)} \quad (3.3)$$

Notice that according to Eq. (3.3) the emission in a homogenous medium is, as expected, $3P_0$ which is the emission power without spatial averaging. The readers are referred to [35] and [43] for a more detailed treatment of the density of states and the emission problem in a homogenous space. For the purposes of the forthcoming sections, it is useful to define Eq. (3.3) in terms of scalar polarizability α , the corresponding wavenumber normalized cross-section σ_{norm} , (using Eq. (2.9)) and the excitation field \vec{E} , as follows:

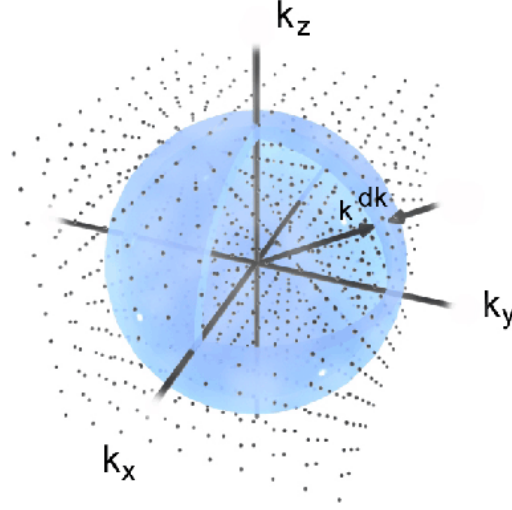


Fig 3.1| the number of k-states in a 3D homogenous medium. Each k value is shown as a point in the k-space. A shell of radius k and thickness dk contains the allowed states. The number of these points is given by $4\pi k^2 dk$. (from: <http://brineyspears.ac>)

$$\begin{aligned}
 P &= \frac{\pi\omega^2}{4\varepsilon(\vec{r}_0)\varepsilon_0} \alpha^2 \left| \vec{E}(\vec{r}_0, \omega) \right|^2 D(\vec{r}_0, \omega) \\
 &= \frac{\pi\omega^2}{4\varepsilon(r_0)\varepsilon_0} \left(\frac{\varepsilon_0^2}{\pi^2} \sigma_{norm} \right) \left| \vec{E}(\vec{r}_0, \omega) \right|^2 D(\vec{r}_0, \omega) \\
 &= \sigma_{norm} \frac{\varepsilon_0}{\pi} \left(\frac{\omega^2}{4\varepsilon(\vec{r}_0)} \right) \left| \vec{E}(\vec{r}_0, \omega) \right|^2 D(\vec{r}_0, \omega)
 \end{aligned} \tag{3.4}$$

3.2 Enhancement of the emission in a cavity with a well-defined Q-factor

In a cavity, the homogeneity of the medium is broken, and the LDOS is no longer given by Eq. (3.2). Instead, the LDOS is determined by the resonance conditions of the cavity, which is ultimately determined by the boundary conditions of the cavity. A cavity mode is characterized by the *Q-factor* of the mode which is defined as,

$$Q = \omega \frac{W}{P_{cav}} = \frac{\omega}{\Delta\omega} \tag{3.5}$$

The Q-factor is defined as the ratio of the energy stored in the cavity W to that of the dissipated energy per radian of the oscillation cycle of the mode. In a steady state, the dissipated energy (or, input energy for critical coupling) per radian of oscillation is the ratio of power P_{cav} pumped into the particular mode and the cavity frequency ω . Incidentally, the ratio $\Delta\omega = P_{cav}/W$ is identified as the FWHM line-width of the resonance frequency of a mode centered at the frequency ω . Assuming that the cavity resonance is described with a Lorentzian line-shape function, the normalized field density, hence, LDOS for a cavity with Q and the effective mode volume V_{eff} is given by:

$$D_{cav}(\omega) = \frac{1}{V_{eff}} \left[\frac{\frac{\Delta\omega}{2\pi}}{(\frac{\Delta\omega}{2})^2 + (\omega - \omega_0)^2} \right] \xrightarrow{\omega=\omega_0} \frac{2}{\pi} \frac{1}{\Delta\omega V_{eff}} = \frac{2}{\pi\omega} \frac{Q}{V_{eff}} \quad (3.6)$$

Here the bracketed term describes the Lorentzian lineshape function. If the cavity consists of lossless composite materials, and a modal field \vec{E} effective mode volume V_{eff} calculated at the maxima of the modal field \vec{E}_{max} is given by:

$$V_{eff}(\omega) \equiv \frac{\iiint \varepsilon(\vec{r}_0, \omega) \left| \vec{E}(\vec{r}, \omega) \right|^2}{\varepsilon(\vec{r}_0, \omega) \left| \vec{E}_{max}(\vec{r}_{max}, \omega) \right|^2} \quad (3.7)$$

Hence, an emitter, if oriented parallel to the polarization of the modal field of the cavity, would emit with a rate enhanced by a factor, called Purcell factor F_p

$$F_p = \frac{D_{cav}}{D_f} = \frac{3}{4\pi^2} \left(\frac{\lambda}{n} \right)^3 \frac{Q}{V_{eff}} \quad (3.8)$$

This is the famous equation suggested by Purcell in his original 1947 paper based on quantum mechanical arguments for nuclear magnetic resonance [41].

3.3 Scattering in a cavity with a well-defined Q-factor

In the Eq. (3.7) the effective mode volume is measured at the maxima of the field. This way of defining the effective mode volume is customary in cavity quantum electrodynamics. However, an emitter may be located at any location of the cavity. For a mode denoted by an index m , and a modal field \vec{E}_m the *local* effective mode volume, \tilde{V}_{eff} is defined as:

$$\begin{aligned} \tilde{V}_{eff}(\vec{r}_0, \omega) &= \frac{\iiint \varepsilon(\vec{r}_0, \omega) \left| \vec{E}_m(\vec{r}, \omega) \right|^2}{\varepsilon(\vec{r}_0, \omega) \left| \vec{E}_m(\vec{r}_0, \omega) \right|^2} \\ &= \frac{W}{\varepsilon_0 \varepsilon(\vec{r}_0, \omega) \left| \vec{E}_m(\vec{r}_0, \omega) \right|^2} = \frac{1}{\left| \vec{e} \right|^2} \end{aligned} \quad (3.9)$$

Note that this definition of the local effective mode volume is position dependent. This definition of effective volume renders it as another way of expressing the field intensity of the mode at a given point in terms of the total energy in the cavity W or the energy-normalized field of the cavity mode $|\vec{e}|^2$ (unit: m^{-3}) as shown in Eq. (3.9). Using Eq. (3.4) with Eq. (3.6) and (3.9), the emission power, P can be written in terms of the energy-normalized field \vec{e} of the cavity mode :

$$P = Q \frac{\omega}{2\varepsilon\varepsilon_0} \left| \vec{d} \cdot \vec{e} \right|^2 \quad (3.10)$$

Here we have used the vector dot product to ensure that the dipole \vec{d} is oriented in the direction of the modal field. Thus, we conclude that the emission in a cavity is proportional to the square of the normalized field in the direction of the dipole at the dipole location. When the cavity mode is excited by a steady state power P_{cav} which in turn excites the dipole, the modal field \vec{E}_m can be written in terms of P_{cav} , if we assume that the pump is also resonant in the cavity with a $Q_p = Q(\omega_p)$. Using the relationship between the modal field \vec{E}_m , the energy stored in the cavity W , i.e. Eq. (3.9), and the definition of Q , i.e. Eq. (3.5), one can write,

$$\begin{aligned} P(\omega_s, \vec{r}) &= \sigma_{norm} \frac{\varepsilon_0}{\pi} \left(\frac{\omega_s^2}{4\varepsilon(\omega_s)} \right) \left| \vec{E}_m(\omega_p, \vec{r}) \right|^2 \frac{2Q_s}{\omega_s \pi} |\vec{e}(\omega_s, \vec{r})|^2 \\ &= \sigma_{norm} Q_s \frac{\omega_s \varepsilon_0}{2\varepsilon(\omega_s) \pi^2} \left(\frac{W(\omega_p) |\vec{e}(\omega_p)|^2}{\varepsilon_0 \varepsilon(\omega_p)} \right) |\vec{e}(\omega_s)|^2 \\ &= \frac{\sigma_{norm}}{2\pi^2} \left[\omega_s Q_s \frac{|\vec{e}(\omega_s)|^2}{\varepsilon(\omega_s)} \right] \left[\frac{Q_p P_{cav}(\omega_p)}{\omega_p} \frac{|\vec{e}(\omega_p)|^2}{\varepsilon(\omega_p)} \right] \\ \implies \frac{P(\omega_s, \vec{r})}{P_{cav}(\omega_p)} &= \frac{\sigma_{norm}(\omega_p, \omega_s)}{2} \frac{\omega_s}{\omega_p} \left[\frac{Q_s}{\pi} \frac{|\vec{e}(\omega_s)|^2}{\varepsilon(\omega_s, \vec{r})} \right] \left[\frac{Q_p}{\pi} \frac{|\vec{e}(\omega_p)|^2}{\varepsilon(\omega_p, \vec{r})} \right] \end{aligned} \quad (3.11)$$

If the Stokes shift is negligible, then the equation takes a simpler form in terms of differential cross-section (see Eq. (2.9)):

$$\frac{P(\omega, \vec{r})}{P_{cav}} = \frac{\sigma_{diff}}{2} \left(\frac{\lambda}{n} \right)^4 \left(\frac{Q}{\pi} \right)^2 |\vec{e}(\omega, \vec{r})|^4 = \sigma_{diff} \Lambda_{cav} \quad (3.12)$$

As for Eq. (2.19), in the previous chapter, we can define a cross-section independent parameter for the cavity called *integrated luminosity* of the cavity Λ_{cav} as,

$$\Lambda_{cav}(\omega, \vec{r}) = \frac{1}{2} \left(\frac{\lambda_0^2}{\varepsilon(\omega, \vec{r})} \frac{Q}{\pi} |\vec{e}(\omega, \vec{r})|^2 \right)^2 \quad (3.13)$$

Thus, scattering in a cavity is proportional to the square of the Q of the cavity and the fourth power of the modal field, if both pump and stokes are resonant with the cavity. Eq. (3.13) is expedient to determine the scattering efficiency in heterogeneous cavities using a mode solver. We shall briefly comment on the use of this equation to determine the relative efficiency of resonators based on dielectric channel waveguides at the end of this chapter (§3.6.1).

3.4 Scattering in an inhomogeneous medium with a 2D invariance

In many cases, as we shall describe next, the boundary conditions of the inhomogeneous medium lead to electromagnetic solutions in terms of orthonormal eigenmodes. In such cases, calculation of the LDOS for each of the eigenmodes is simplified by counting the respective spatial mode density and calculating the corresponding mode volume.

3.4.1 Calculation of LDOS and enhancement

In case of an inhomogeneity with a 2D invariance, such as planar dielectric waveguides (say, slab waveguides with its normal oriented in Z direction), the calculation of the LDOS for the eigenmodes can be performed by counting the number of spatial modes in 2D $k_x k_y$ -space. For a k -space within a radius k defined by an arbitrary square of side l in the direction of the symmetry (Fig. 3.2), the number of modes is given by $N = \pi k^2 / (2\pi/l)^2$. The LDOS for such a structure is then given by:

$$\begin{aligned} D_{2D}(\vec{r}_0, \omega) &= \frac{1}{V_{eff}(\vec{r}_0, \omega)} \frac{dN}{d\omega} \\ &= \frac{4\pi k}{V_{eff}(\vec{r}_0, \omega) (2\pi/l)^2} \frac{dk}{d\omega} \\ &= \frac{1}{2\pi l_{eff}(\vec{r}_0, \omega)} \frac{k}{v_g} \end{aligned} \quad (3.14)$$

Here, V_{eff} and l_{eff} are respectively the effective mode volume and effective mode width defined by Eq. (3.8) and Eq. (3.15) respectively. Because of the spatial invariance in the x-y plane, the arbitrary area l^2 in xy plane is the same as the corresponding integral component in x-y plane. Hence, the effective mode volume is reduced to an effective mode width l_{eff} defined as follows,

$$\begin{aligned} l_{eff}(\vec{r}_0, \omega_p) &\equiv \frac{\int_{-\infty}^{\infty} \varepsilon(\vec{r}, \omega) |\vec{E}_m(\vec{r}, \omega)|^2 d\vec{r}}{\varepsilon(\vec{r}_0, \omega) |\vec{E}_m(\vec{r}_0, \omega)|^2} \\ &= \frac{W_2}{\varepsilon(\vec{r}_0, \omega) \varepsilon_0 |\vec{E}_m(\vec{r}_0, \omega)|^2} \\ &= \frac{1}{|\vec{e}_2(\vec{r}_0, \omega)|^2} \end{aligned} \quad (3.15)$$

where $|\vec{e}_2|^2$ (unit: m^{-1}) is the modal field intensity, normalized to the unit energy W_2 stored in the structure per unit area in the x-y plane [47]. Hence, using Eq. (3.3), the enhancement compared to the free-space emission for a dipole orientation parallel to the modal field is given by,

$$F_{2D} = \frac{D_{2D}(\omega)}{D_f(\omega)} = \frac{3}{4} \frac{n_g}{n_{eff}} \left(\frac{\lambda}{n} \right) \frac{1}{l_{eff}} = \frac{3}{4} \frac{n_g}{n_{eff}} \left(\frac{\lambda}{n} \right) |\vec{e}_2|^2 \quad (3.16)$$

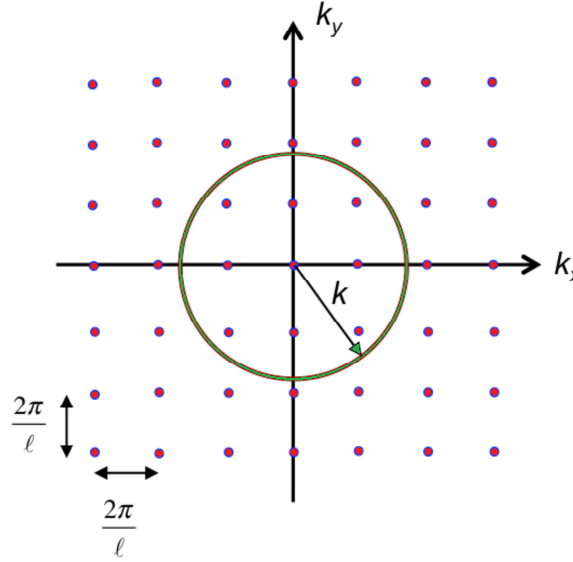


Fig 3.2| Determination of the number of k -states in 2D k -space. The number of states within k is given by $(\pi k^2)/(2\pi/l)^2$.

For a dipole of strength \vec{d} , using Eq. (3.3), the power emitted in the mode can be calculated as,

$$P_{2D} = \frac{\pi\omega^2}{4\epsilon\epsilon_0} \left(\frac{k}{2\pi v_g} |\vec{e}_2(\vec{r}_0, \omega)|^2 \right) |\vec{d}|^2 = \frac{1}{8\epsilon\epsilon_0} \left(\frac{\omega^2 k}{v_g} \right) |\vec{d} \cdot \vec{e}_2(\vec{r}_0, \omega)|^2 \quad (3.17)$$

This is the same as that calculated using other methods for 2D multilayer waveguides and plasmonic structures [44] [45].

3.4.2 Scattering efficiency

The effective mode width for the waveguide is directly related [13, 47] to the excitation power flow P in the waveguide and the group velocity v_g via the relation $P_{in} = kv_g W_2$ where W_2 is the energy stored per unit area as defined in Eq. (3.15). Thus, for scattering near the planar waveguides, using Eq. (3.4), Eq. (3.14), and Eq. (3.15), we obtain,

$$\frac{P_{2D}(\vec{r}_0, \omega_p, \omega_s)}{P_{in}(\omega_p)} = \frac{\omega_s^2 \sigma_{norm}(\omega_p, \omega_s)}{8\pi^2} \left(\frac{k(\omega_p)}{v_g(\omega_p)} \frac{|\vec{e}_2(\vec{r}_0, \omega_p)|^2}{\epsilon(\omega_p)} \right) \left(\frac{k(\omega_s)}{v_g(\omega_s)} \frac{|\vec{e}_2(\vec{r}_0, \omega_s)|^2}{\epsilon(\omega_s)} \right) \quad (3.18)$$

In terms of the differential cross-section, for Raman scattering when the Stokes shift is negligible, Eq. (3.18) reads as:

$$\frac{P_{2D}}{P_{in}} = \frac{\sigma_{diff}}{2\varepsilon^2} \left(\frac{n_{eff}^2 n_g^2}{\lambda_0^2} \right) |\vec{e}_2(\vec{r}_0, \omega)|^4 = \sigma_{diff} \Lambda_{2D} \quad (3.19)$$

where, as in the case of Eq. (3.13), we have defined a cross-section independent parameter Λ_{2D} as the integrated luminosity of the structure defined as:

$$\Lambda_{2D}(\vec{r}_0, \omega) = \frac{1}{2} \left(\frac{n_{eff} n_g}{\lambda_0} \frac{|\vec{e}_2(\vec{r}_0, \omega)|^2}{\varepsilon(\vec{r}_0, \omega)} \right)^2 \quad (3.20)$$

If the emission is isotropic, one can calculate the coupled power for every infinitesimal angle $d\theta$ in the plane of symmetry of the structure.

3.5 Scattering in an inhomogeneous medium with 1D invariance

If the inhomogeneity medium is invariant in one of the dimensions (say x direction), such as in case of a dielectric channel waveguide, the calculation of LDOS can be performed by counting the number of modes in 1D k-space, (Fig. 3.4). The number of modes within a radius k in the k-space defined by an arbitrary length l in x direction is given by $N = 2k/(2\pi/l)$. The factor 2 in this expression originates to account for the forward and the backward propagating modes.

$$D_{1D}(\omega) = \frac{1}{V_{eff}} \frac{dN}{d\omega} = \frac{1}{V_{eff}} \frac{2}{(2\pi/l)} \frac{dk}{d\omega} = \frac{l}{V_{eff}} \frac{1}{\pi} \frac{1}{v_g} = \frac{1}{\pi A_{eff} v_g} \quad (3.21)$$

Here, similar to the 2D case, the arbitrary length l in the direction of invariance (\hat{x}) is identical with the corresponding component of the integration in the x-axis. The effective mode area A_{eff} is defined by:

$$\begin{aligned} A_{eff}(\vec{r}_0, \omega_p) &\equiv \frac{\iint \varepsilon(\vec{r}, \omega) |\vec{E}_m(\vec{r}, \omega)|^2 d\vec{r}}{\varepsilon(\vec{r}_0, \omega) |\vec{E}_m(\vec{r}_0, \omega)|^2} = \frac{W_1}{\varepsilon(\vec{r}_0, \omega) \varepsilon_0 |\vec{E}_m(\vec{r}_0, \omega)|^2} \\ &= \frac{1}{|\vec{e}_1(\vec{r}_0, \omega)|^2} \end{aligned} \quad (3.22)$$

The effective mode area of the mode symmetric in 1D allows us to normalize the local field by the average energy stored per unit length of the waveguide W_1 . The modal field intensity, normalized to the energy W_1 stored in the structure per unit cross-section, denoted by $|\vec{e}_1|^2$ (unit: m^{-2}) can then be used instead of an

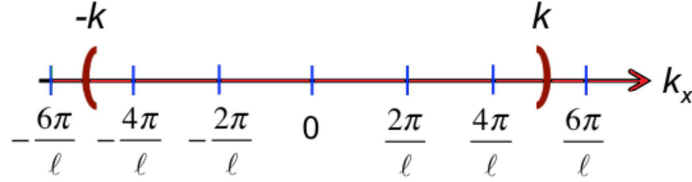


Fig 3.4 | Determination of the number of k -states in 1D k -space. The number of states within k is given by $2k/(2\pi/l)$.

effective area to determine the enhancement. Using Eq. (3.3), the enhancement in the emission is calculated as,

$$F_{1D} = \frac{D_{1D}(\omega)}{D_f(\omega)} = \frac{3}{4\pi} \frac{n_g}{n} \left(\frac{\lambda}{n}\right)^2 \frac{1}{A_{eff}} = \frac{3}{4\pi} \frac{n_g}{n} \left(\frac{\lambda}{n}\right)^2 |\vec{e}_1|^2 \quad (3.23)$$

The energy per unit waveguide length W_1 is related [13] to the excitation power P_{in} of the mode and its group velocity v_g , via $P_{in} = v_g W_1$. Thus, using Eq. (3.4), Eq. (3.21), and Eq. (3.23), we can write for Raman scattering,

$$\frac{P_{1D}(\vec{r}_0, \omega_p, \omega_s)}{P_{in}(\omega_p)} = \frac{\omega_s^2 \sigma_{norm}(\omega_p, \omega_s)}{4\pi^2} \left(\frac{|\vec{e}_1(\vec{r}_0, \omega_p)|^2}{v_g(\omega_p) \varepsilon(\omega_p)} \right) \left(\frac{|\vec{e}_1(\vec{r}_0, \omega_s)|^2}{v_g(\omega_s) \varepsilon(\omega_s)} \right) \quad (3.24)$$

If the Stokes shift is negligible, Eq. (3.24) takes following simpler form, in terms of differential cross-section:

$$\frac{P_{1D}}{P_{in}} = \sigma_{diff} \lambda_0^2 \frac{n_g^2}{\varepsilon^2} |\vec{e}_1|^4 = \sigma_{diff} \Lambda_{1D} \quad (3.25)$$

where, as in Eq. (3.13), we have defined cross-section independent parameter Λ_{1D} as the integrated luminosity of the structure defined as:

$$\Lambda_{1D}(\vec{r}_0) = \left(\lambda_0 \frac{n_g}{\varepsilon(\vec{r}_0)} |\vec{e}_1|^2 \right)^2 \quad (3.26)$$

3.5.1 Comparison with free-space excitation and collection

In Chapter 2 we calculated the efficiency of scattering by the average intensity of the fundamental Gaussian mode within the beam waist w_0 . The total Raman power emitted by the same molecule when excited by a silicon nitride can be calculated using Eq. (3.24). Fig. (3.5) plots $\log_{10}(\Lambda_{1D}/\Lambda_{DL}) = \log_{10}(\bar{P}_{w,0})$ for different

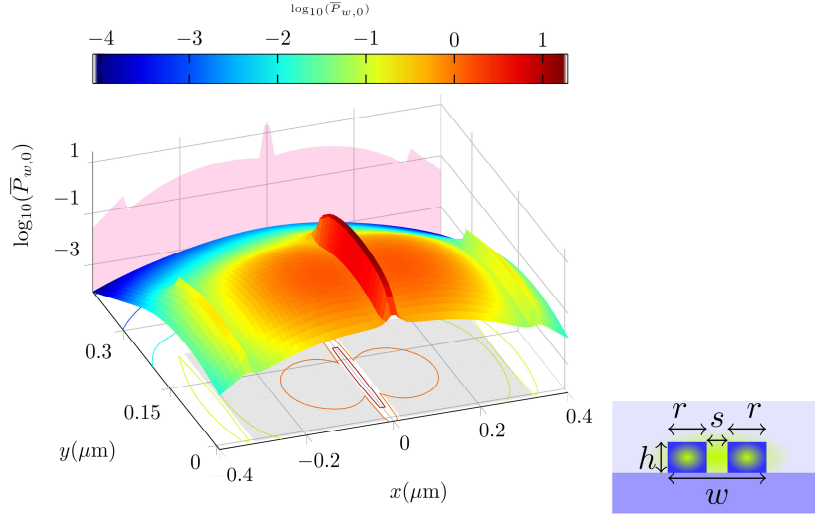


Fig. 3.5| Power coupled to a slot waveguide mode normalized to an ideal free-space excitation and collection. $\log_{10}(\bar{P}_{w,0})$ for a slotted waveguide ($s = 20$ nm, $w = 660$ nm, see inset for a cross-section of slotted waveguide) shown in 3D highlighting the variations of the coupled power across the various regions of the section. The purple shaded area shows the projection of $\bar{P}_{w,0}(\vec{r}_0)$, indicating the maxima of the $\bar{P}_{w,0}$. The contours represent the lines with the same $\bar{P}_{w,0}$ and the color bar shows the magnitude of $\bar{P}_{w,0}$. The gray shaded region in the x - y plane indicates the waveguide cross-section which is also shown in the inset.

positions in the surrounding of a silicon nitride slot waveguide ($s = 20$ nm, $w = 660$ nm, see Fig 3.5 for a cross-section of a slotted waveguide, also discussed in §4.1.2 in more detail) in water calculated by the *COMSOL* finite elements mode solver for the fundamental TE mode. $\bar{P}_{w,0}$ is the power coupled from a particle to the fundamental TE waveguide mode, normalized to the total emission from the particle when excited by a diffraction limited beam with $NA = 1$. The figure shows that more than one order of magnitude of power is coupled to the waveguide mode compared to the total emission in the most ideal diffraction-limited system. This result demonstrates the possibility of a large broadband Purcell enhancement [76] that could be utilized with waveguides. Implications of this result will be discussed in detail in forthcoming sections.

3.6 Closing Remarks

Table 3.1 summarizes the integrated luminosity calculated for excitation and collection by means of eigenmodes in medium described by different symmetry properties. Note that the normalized mode profile has different units depending on different symmetry conditions and corresponding normalization. We see that the

S No.	Excitation and collection medium	Integrated Luminosity, $\Lambda(\vec{r})$
1	A fundamental Gaussian mode, Diffraction limited optics in free-space	$\left(\frac{1}{4\pi\lambda_0^2} \vec{e}_g(\vec{r}) ^2\right)$
2	A cavity mode with a well-defined Q	$\frac{1}{2} \left(\frac{\lambda_0^2}{\varepsilon(\vec{r})} \frac{Q}{\pi} \vec{e}(\vec{r}) ^2\right)^2$
3	A mode in an inhomogeneous medium with a 2D symmetry (e.g. slab waveguides)	$\frac{1}{2} \left(\frac{n_{eff} n_g}{\lambda_0 \varepsilon(\vec{r})} \vec{e}_2(\vec{r}) ^2\right)^2$
4	A mode in an inhomogeneous medium with a 1D symmetry (e.g. channel waveguides)	$\left(\lambda_0 \frac{n_g}{\varepsilon(\vec{r})} \vec{e}_1(\vec{r}) ^2\right)^2$

Table 3.1 | Comparison of scattering efficiencies in terms of integrated luminosities for a mode in various scattering media for excitation and collection.

integrated luminosity is proportion to fourth power of the normalized modal field and some function of mode size, which is represented by some function of wavelength. In this thesis we have assumed loss-less materials; a generalization to lossy materials may be performed in a similar manner.

3.6.1 Resonators formed with dielectric channel waveguides

Here we briefly discuss the significance of Eq. (3.12) to determine the scattering efficiency of a particle located in the vicinity of resonators consisting of an inhomogeneous dielectric material. Some examples of such cavities are micro-ring resonators or a cavity formed with a short waveguide with Bragg reflectors at the ends. With the knowledge of the Q of the cavity, either via a direct measurement of Q , or indirectly via the knowledge of the dissipation of the cavity, the scattering efficiency can be calculated using Eq. (3.12). In a cavity formed using a dielectric channel waveguide of length l , the normalized field can be calculated as,

$$\begin{aligned}
|\vec{e}(\vec{r}_0, \omega)|^2 &= \frac{|\vec{E}_m(\vec{r}_0, \omega)|^2}{\iiint \varepsilon(\vec{r}) |\vec{E}_m(\vec{r}_0, \omega)|^2 d\vec{r}} \\
&= \frac{|\vec{E}_m(\vec{r}_0, \omega)|^2}{l \iint \varepsilon(\vec{r}) |\vec{E}_m(\vec{r}_0, \omega)|^2 d\vec{r}} \\
&= \frac{|\vec{e}_1(\vec{r}_0, \omega)|^2}{l}
\end{aligned} \tag{3.27}$$

Here, we have used the modal field normalized with average energy per unit length $|\vec{e}_1|^2$ defined for a 1D-symmetric inhomogeneous medium (Eq. 3.22) which can be solved using a 2D mode solver. Using Eq. (3.12), Eq. (3.25) and Eq. (3.26)

we find that,

$$\frac{P_{wg,cav}}{P_{wg}} = \frac{\Lambda_{cav}}{\Lambda_{wg}} = \frac{1}{2} \left(\frac{Q \lambda_0}{\pi l n_g} \right)^2 \quad (3.28)$$

Eq. (3.28) means that if a molecule lying in the vicinity of a standard dielectric waveguide scatters a power P_{wg} then, the molecule radiates a power $P_{wg,cav}$ enhanced by a factor $\Lambda_{cav}/\Lambda_{wg}$ given by Eq. (3.28). It is true if the waveguide forms a cavity of waveguide length l and both pump and Stokes are resonant. Thus as expected, the enhancement is high for small resonators, shorter wavelengths and high Q resonators.

3.6.2 Fluorescence and non-radiative transitions

We have treated the radiation and scattering problem classically and we have neglected the non-radiative decay process and interactions within the molecule. Moreover, *strong coupling regime* leading to Rabi oscillations is neglected. A complete analysis requires a quantum mechanical treatment which is outside the scope of this thesis. Our classical treatment is sufficient in many the typical cases of biochemical sensing in so called *weak coupling regime*, where the coupling between the dipole and the field is sufficiently low. The reader is referred to Loudon [34] for a detailed quantum mechanical description of the emission process that is needed to describe the process in strong coupling regime. The results discussed in this chapter are also applicable for the fluorescence process, if the emission process is dominated by radiative transitions.

4

NWERS of bulk material in the cladding

In the previous chapter we looked into efficiencies of scattering in different types of inhomogeneous dielectric media. In this chapter we specifically focus on evanescent Raman scattering near single-mode dielectric channel waveguides, which has 1D symmetry. Dielectric channel waveguides are very popular in integrated photonics as they confine light with the lowest *étendue* (§Appendix D) and also for its relative ease of fabrication using chemical etching processes. In this chapter we will also discuss experimental demonstration of Raman spectroscopy of bulk materials using a high index contrast, CMOS-compatible, integrated single-mode silicon nitride (Si_3N_4) waveguides in the context of nanophotonic waveguide enhanced Raman spectroscopy (NWERS). We also derive the dependence of collected Raman power with the waveguide parameters and experimentally verify the derived relations. Some sections of the text and figures have been adapted from some of my published papers [1], [48] - [50].

4.1 The efficiency of scattering

In Chapter 3, we saw that the efficiency of excitation and collection of Raman signal depends on waveguide dependent factor called *integrated luminosity* of the waveguide symbolized by $\Lambda_{1D}(\vec{r}, \omega)$ with the waveguide. We now investigate the total integrated power collected by a waveguide assuming that the scattering

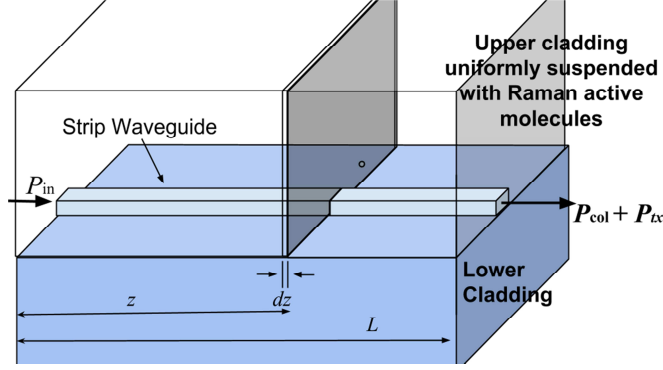


Fig. 4.1 | Schematic of our analysis applied to the strip waveguide geometry. The particles are assumed to be embedded with a uniform density on the upper cladding. Symbols are explained in the text. (Adapted from [48].) P_{in} is the input pump power, L is the length of the waveguide assumed to be oriented parallel to the z -axis P_{col} is the Raman signal power collected by the waveguide, and P_{tx} is the transmitted pump power.

molecules lie on top of a channel waveguide as its top cladding. We assume that the molecules are suspended uniformly in the upper cladding of the waveguides with a density ρ . For emitters forming a thin sheet of thickness dz orthogonal to the waveguide and covering the entire cladding area (see Fig. 4.1), the efficiency is given by the sum of the individual incoherent contributions:

$$\frac{dP_{col}}{P_{in}} = dz\rho\sigma \iint_{clad} \Lambda_{1D}(\vec{r}) d\vec{r} = dz\rho\sigma\eta_0 \quad (4.1)$$

where the integral in the top cladding region, $\eta_0 = \iint \Lambda_{1D}(\vec{r}) d\vec{r}$ is the *specific conversion efficiency* of the waveguide. The specific conversion efficiency η_0 for a given waveguide section is an important parameter. It has the unit of solid angle (sr), reminiscent of the collection efficiency of a diffraction-limited optical microscope described by Eq. (2.16). Like Λ_{1D} , it is determined uniquely by the electromagnetic mode as defined by the waveguide dielectric function.

Although we have assumed that the entire upper cladding is covered by the analyte molecules, a thickness of few e^{-1} lengths is sufficient to produce an equivalent result, as the interaction takes place with exponentially decaying evanescent tail of the mode in the cladding. For Si_3N_4 waveguides, the e^{-1} length is less than 80 nm, hence a 160 nm thick layer is enough to produce a result practically equivalent to an infinite semi-infinite cladding.

4.1.1 Efficiency for Strip waveguides

In Fig. 4.2 we show the theoretical conversion efficiency η_0 calculated for Si_3N_4 and SOI strip waveguides for normalized waveguide widths k_0w and fixed height

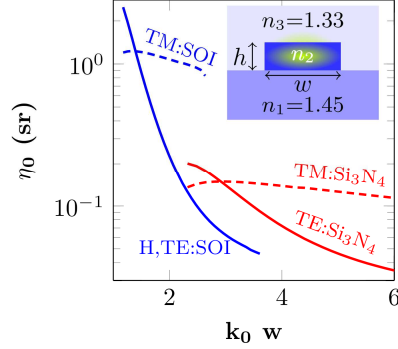


Fig 4.2 | Theoretical η_0 curves for strip waveguides as a function of the normalized waveguide width w for Si (blue) and Si_3N_4 (red) waveguide systems for fixed $h = 220$ nm. Solid lines: TE polarized excitation and collection. Dashed lines: TM polarized excitation and collection. Only the curve segments corresponding to a well-defined single mode operation are shown. **Inset:** a general strip waveguide (adapted from [1], [50]).

$h = 220$ nm corresponding to single mode operation of the waveguides. As the waveguide width is increased, η_0 increases to a maximum corresponding to an optimal mode confinement in the core and the cladding. Once this condition is reached, further increase in the width leads to a decrease in η_0 owing to more confinement of the modal field in the core. This reduces the interacting field in the upper-cladding region of the analyte. The discontinuity of the electric field at the core - top cladding interface of the TM modes leads to a higher evanescent field at the position of the analyte. Thus, higher index contrast waveguides with TM polarization generally perform better than TE polarized modes. The optimal widths for Si_3N_4 waveguides at 785 nm are near 260 nm and 300 nm for TE and TM excitation and collection respectively, while for SOI waveguides it is near 150 and 240 nm respectively.

4.1.2 Efficiency for slotted waveguides

As depicted in Fig 4.3(a), slotted waveguides have a narrow slot of width s in between the rails of the core material of rail width r . Due to the boundary conditions of the electromagnetic field, the existence of a narrow slot leads to a huge enhancement of the field in the slotted region, and hence also to the value of η_0 , at least for the TE-mode. For a fixed rail width $r = 275$ nm and thickness $h = 220$ nm, Fig 4.3(a) shows η_0 calculated for Si_3N_4 and Si slot waveguides for variable slot widths using Eq. (4.1). A significant increase in η_0 is observed as s is reduced for TE modes because of the enhancement of the TE-field in the slot region as s is decreased. In case of SOI waveguides, where the index contrast is higher and much higher field enhancement can be expected, the value of η_0 reaches up to 40

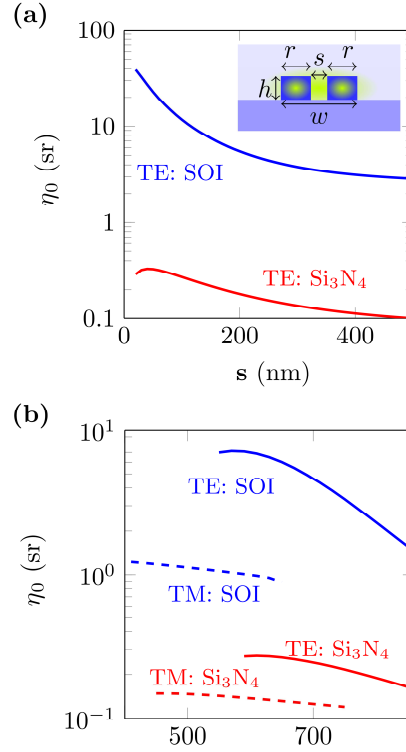


Fig. 4.3 | Theoretical conversion efficiency η_0 for slotted waveguides for SOI (blue) and Si₃N₄ (red) waveguide systems. **a)** Fixed $r = 350$ nm, $h = 220$ nm, as a function of slot width s for fundamental TE mode. **b)** Fixed $s = 150$ nm, $h = 220$ nm, as a function of waveguide width $w = s + 2r$. Solid lines: TE polarized excitation and collection. Dashed lines: TM polarized excitation and collection. (Adapted from [1], [50])

sr for $s = 20$ nm.

Fig 4.3(b) shows η_0 calculated for Si₃N₄ and SOI for a fixed slot width $s = 150$ nm and for various total widths w , inclusive of the slot width s (note: $r = (w - s)/2$). As observed in the case of strip waveguides, η_0 decreases when the waveguide width is increased as a result of the confinement of the mode in the core and consequent reduction of the interaction volume in the analyte region. Due to the continuity of the electric field, the field enhancement in the slot is much less in case of TM polarization leading to comparatively insignificant enhancement.

4.1.3 Equivalent length and enhancement

Comparing Eq. (4.1) and Eq. (2.16), we can define an equivalent length l_{eq} , which corresponds to the length of the waveguide that gives the same signal as that of

diffraction limited confocal microscopes.

$$l_{eq} = \frac{2}{\eta_0} \left(\frac{\lambda_0}{n} \right) \quad (4.2)$$

Depending on the index contrast, polarization and design of the waveguides, η_0 may typically vary from 0.1 sr to 50 sr. Thus a waveguide length $l < 20\lambda_0$ wavelengths is enough to provide an efficiency equivalent to that of a diffraction-limited confocal microscope. A single mode waveguide loss of 1dB/cm is typical for the considered integrated photonics platforms, allowing more than a centimeter of waveguide without significant loss of the pump or collected signal. This leads to 3-5 orders of magnitude enhancement of the signal compared to diffraction-limited free-space systems.

4.2 Considerations for coupling losses and waveguide losses

Now we consider a practical situation and consider coupling and waveguide losses. We refer again to Fig. 4.1. A pump laser with power P_{in} is incident on the input facet of the waveguides, of which a fraction gets coupled to the waveguide mode with coupling efficiency γ_{in} and propagates along the waveguide. During the propagation, molecules in the cladding are excited, and the scattered spontaneous Raman signal is collected via evanescent coupling to the same waveguide, as described by Eq. (4.1) in both forward and backward propagating directions. In the forward propagating configuration, only half of the collected power is measured at the output facet with an output coupling efficiency γ_{out} . Accounting for coupling losses and attenuation of the pump and collected signal in the waveguide, the ratio of signal power collected (P_{col}) at the end of the waveguide to the input power (P_{in}) is given by:

$$\begin{aligned} \frac{P_{col}(L)}{P_{in}} \equiv \xi(L) &= \frac{\rho\sigma\eta_0}{2} \gamma_{in}\gamma_{out} \int_0^L e^{-\alpha_p z} e^{-\alpha_s(L-z)} dz \\ &= \frac{\rho\sigma\eta_0}{2} \gamma_{in}\gamma_{out} e^{-\alpha_p L} \left[\frac{e^{\delta\alpha L} - 1}{\delta\alpha} \right] \end{aligned} \quad (4.3)$$

where α_p and α_s are the waveguide losses at the pump wavelength and at the Stokes wavelength respectively and $\delta\alpha = \alpha_p - \alpha_s$ is their difference. The factor of 1/2 accounts for a backward propagating signal that is not collected in the current configuration of our experimental setup. The term in brackets evolves to L when $\delta\alpha \rightarrow 0$.

If we assume that the coupling efficiencies from the waveguide end to the detector are equal for the pump and the Stokes signal, the Raman power collected at the end of the waveguide can be expressed in terms of the transmitted pump power

(P_{tx}) at the detector, which can be directly measured. Thus, for many practical cases, it is convenient to define a quantity $\zeta(l)$ that is independent of coupling and waveguide losses:

$$\zeta(l) \equiv \frac{P_{col}(l)}{P_{tx}(l)} = \frac{\rho\sigma\eta_0}{2} \left[\frac{e^{\delta\alpha l} - 1}{\delta\alpha} \right] = \frac{\eta_0}{2} \sigma\rho l (1 + \Delta) \quad (4.4)$$

Here, $\Delta = (l\delta\alpha)/2! + (l\delta\alpha)^2/3! + \dots$ is generally a negligible quantity for small waveguide lengths, small waveguide losses or small Stokes shifts. In a later section we show how the effect of Δ can be determined for an accurate measurement.

Eq.(4.1) - Eq.(4.4) are the main theoretical results of this chapter and express how the collected signal power depends on the input or transmitted pump power. In many situations, the quantity $\xi(L)$ is of practical interest, as the direct measure of the collected power for a given input power. However, it depends on coupling efficiencies and waveguide loss, which vary in the experiments. The quantity $\zeta(L)$ is independent of the coupling and the waveguide loss and can be used for the purposes of direct analysis of signal strength with respect to concentration, cross-section, waveguide geometry and length.

4.3 Experimental demonstration of evanescent Raman scattering

In this section we describe the experimental setup and the experimental results obtained for the silicon nitride waveguides, and compare with the results based on theoretical models described in previous sections. The details of the waveguide fabrication technology used for the experiments have been briefly discussed in §1.3.

4.3.1 Measurement setup

The setup used in our measurements is described in Fig. 4.4. A tunable Ti:sapphire laser is set to a pump wavelength of $\lambda_P = 785$ nm (red) after which the polarized beam passes through a half-wave plate ($\lambda_0/2$) in order to rotate the polarization to a TE-polarized beam. The pump beam then passes through a laser line filter (LLF) for side-band suppression before it is coupled into the chip by an aspheric lens (ASPH). The output beam is collected with an objective (OBJ) and passes through a polarizer P (set to either TE or TM depending on the measurement) before it is filtered by a dichroic mirror which reflects the pump beam and transmits all Stokes wavelengths (green). The Stokes light is collected into a fiber using a parabolic mirror collimator (PMC) after which the fiber is split by a fiber splitter (FS) of which 1% goes to a power meter (PM) and 99% to a commercial spectrometer either from *Avantes* (AvaSpec-ULS2048XL) or *Andor* (Shamrock 303i

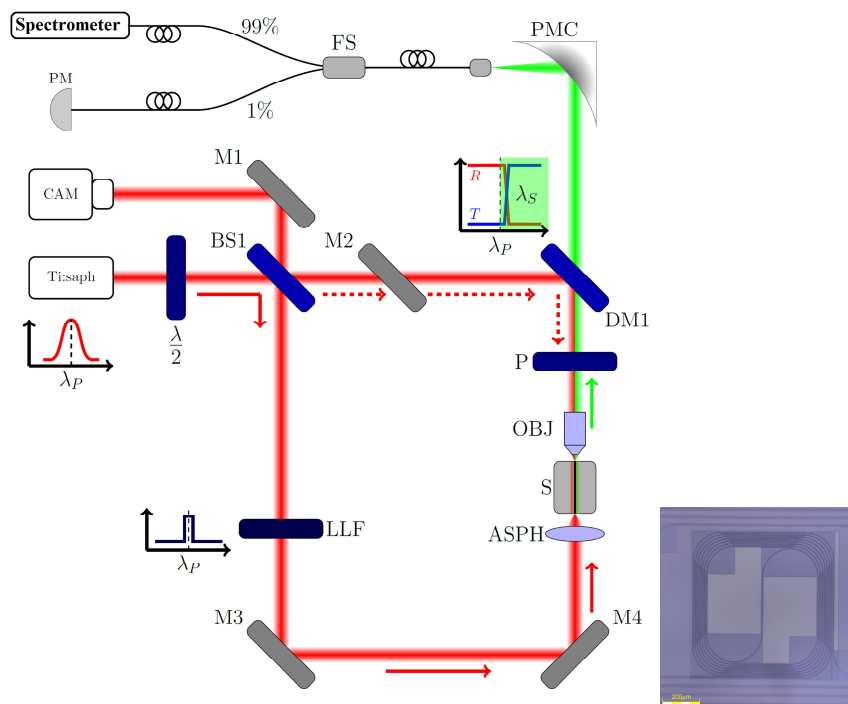


Fig. 4.4| Schematic of the experimental setup and a typical waveguide spiral. *Ti:saph*: tunable Ti:sapphire laser emitting the pump beam at $\lambda_P = 785$ nm, **PM**: power meter, **BS1**: beamsplitter, $\lambda_0/2$: half-wave plate, **LLF**: laser line filter for 785 nm, **P**: polarizer, **M**: fixed mirror, **OBJ**: objective (50X, NA=0.9), **ASPH**: aspheric lens (NA = 0.5), **S**: sample stage, **DM**: dichroic mirror, **PMC**: parabolic mirror collimator (refractive focal length = 15 mm, NA = 0.2), **FS**: fiber splitter, **CAM**: camera to observe the facet of the waveguide (adapted from [1] , courtesy of F. Peyskens). A typical chip with a typical waveguide spiral is also shown in the bottom inset.

spectrometer with iDus 416 cooled CCD camera). The 1% fiber tap is used during alignment and to measure the transmitted power.

4.3.2 Evanescent spectroscopy of bulk liquid

The analyte, which is pure isopropyl alcohol (IPA) here, is drop-casted on the chip containing the waveguides and covers the relevant waveguide region. The Raman signal of the analyte is collected via the same waveguide and measured with a commercial spectrometer as described in the previous section. For strip waveguides, a width w of 700 nm is chosen while for slot waveguides, a slot width $s = 150$ nm, and total waveguide width $w = 700$ nm is chosen. Both of the waveguides have a height $h = 220$ nm. The waveguides are 1cm in length and are coiled as spirals (typical footprint: $800 \mu\text{m} \times 500 \mu\text{m}$).

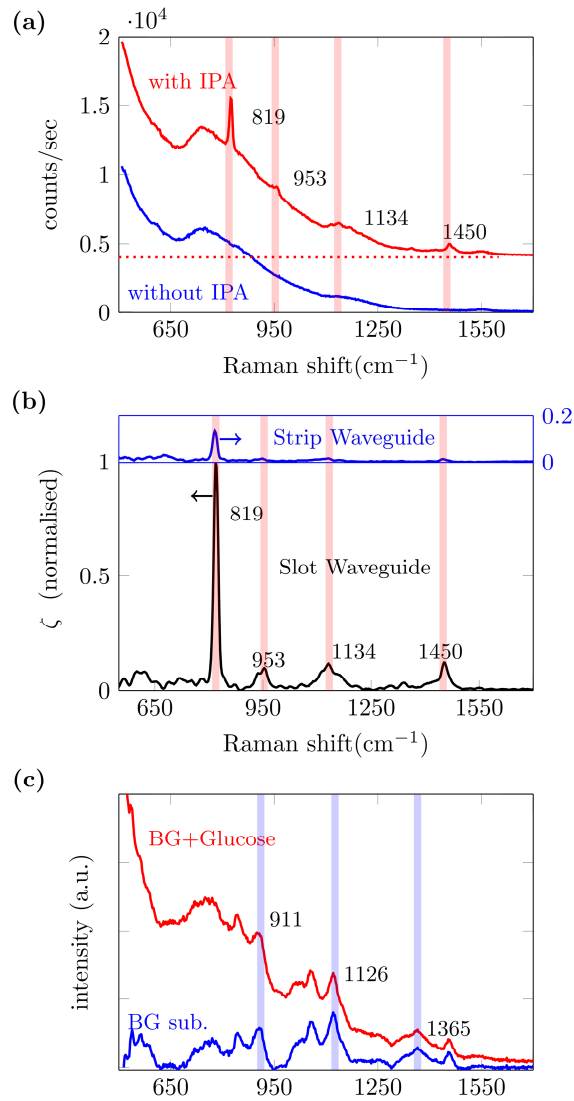


Fig. 4.5 | (a) Raman spectra measured from a 1.6 cm waveguide ($w = 700$ nm) without IPA (blue) and with IPA (red) on top. The spectrum with IPA is shifted vertically with zeros at the dashed red line. (b) Evanescently measured Raman spectra of IPA after background subtraction. The spectra are normalized to the 819 cm^{-1} peak (C-C-O stretch) of obtained from the slot waveguide ($w = 700$ nm, $s = 150$ nm), shown in black. The blue spectrum (with blue axes) is obtained by using a 700 nm wide Si_3N_4 strip. (c) Evanescently measured Raman spectra of 1M glucose solution before and after waveguide background subtraction obtained from the slot waveguide ($w = 700$ nm, $s = 150$ nm), the glucose peaks including 911 cm^{-1} (CCH symmetric stretch), 1126 (CO symmetric stretch), 1365 cm^{-1} (OCH, COH and CCH bend) and others can be seen. Adapted from [1], [50]

Fig. 4.5(a) shows the background observed from the waveguide before application of IPA and the Raman spectrum of IPA observed on it after application of IPA. The background was removed by subtracting the truncated polynomial fit to the background (described further in Appendix C) [51]. Fig. 7(b) shows typical Raman spectra of IPA obtained using such a procedure for a strip waveguide ($w = 700$ nm) and a slotted waveguide ($w = 700$ nm and $s = 150$ nm). We can clearly distinguish all the major peaks of IPA obtained using both waveguide types. As an alternate analyte we also apply a 1M glucose solution on top of the slot waveguide ($w = 700$ nm, $s = 150$ nm). In Fig. 5 (c) the spectra obtained from the glucose solution before and after background correction are shown. We observe strong peaks that match well with the known Raman spectrum of α -D glucose solution.

4.4 Validation of the Theoretical Model

One key highlight of Fig 4.5(b) is that about an eight-fold increase in the signal is observed for slotted waveguides compared to the strip waveguides, in accordance with the theory. To verify the theory further, in Fig. 4.6, the experimentally determined values of η_0 for various waveguide geometries and polarizations are compared with the theoretical values obtained using Eq. (4.3) and the signal corresponding to the 819 cm^{-1} vibration of IPA. The theoretical curves of η_0 as a function of waveguide width w are found to be within the error margin of the experimental data for both polarizations and the waveguide types studied (for details see [2]). These experimental results validate the theoretical model developed and discussed throughout earlier chapters and Sec I.

4.4.1 Sources of errors

For the measurement result shown in Fig 4.6, four chips containing different waveguide dimensions and geometries were diced from different locations on a wafer and measured three times for the experiments. A considerable spread in the measured values can be seen. This spread comes mainly from variation of the waveguide properties among the several waveguides on several chips and from the variation of the transmitted power caused by mechanical instability of the stages used for coupling, shot-noise of the laser and laser power drifts. The variation is particularly high for slotted waveguides due to variability of the slot width during the etching process. Variations in the thickness of SiO_2 and Si_3N_4 across the wafer during deposition also lead to the observed spread. Another important source of variation is side-wall roughness of the waveguides due to imperfect waveguide etching which has not been taken into account in our theory, but which may affect the coupling of the Raman signal to the waveguide.

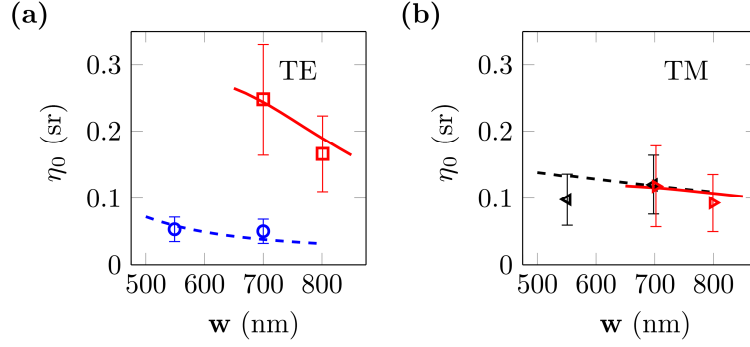


Fig. 4.6 The theoretical and experimental values of η_0 obtained for (a) TE modes and (b) TM modes of Si_3N_4 waveguides. The markers with error bars represent the estimated experimental errors [50]. The lines represent theoretical curves. The red solid lines are the theoretical curve for slot waveguides with $s = 150$ nm. The blue and black dashed lines are the theoretical curves for TE and TM polarizations respectively for strip waveguides. Circle: TE polarization, strip waveguides. Square: TE polarization, slot waveguides. Left handed triangles: TM polarization, strip waveguides. Right handed triangles: TM polarization, slot waveguides (adapted from [1], [50]).

4.5 Performance in comparison to the confocal microscopes

Having established the relevance of our model, we will now experimentally investigate the enhancement predicted by the model. In section I (Eq. 4.2), we introduced the equivalent length l_{eq} of the NWERS system which theoretically predicts an enhancement $\Phi = l_{eq}^{-1}$ per unit length per sr compared to a confocal microscope. The enhancement Φ is plotted in Fig. 4.7. In this section, we show that compared to the confocal microscopes, a 1 cm long silicon nitride (Si_3N_4) waveguide leads to more than three orders of magnitude higher signal. Such an enhancement of the signal contributes to a higher SNR for the waveguide systems compared to the dark-noise limited Raman microscopic systems. We also show that the use of the slotted waveguides increases the signal-to-noise Ratio (SNR) and collection efficiency in accordance with the theoretical results shown in Fig 4.7.

For experiments described in this chapter, strip waveguides with a width w of 700 nm is chosen while for slot waveguides, slot width $s = 150$ nm, and total waveguide width $w = 700$ is chosen. Both of the waveguides have the height $h = 220$ nm. As in the earlier experiments, the waveguides are 1cm in length and are coiled as spirals. To compare the on-chip approach with the conventional Raman microscope, we use a commercial confocal Raman microscope (WITec Alpha300R+). For both cases, the same excitation laser wavelength and the same

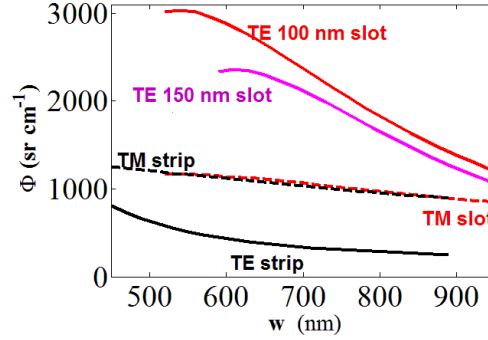


Fig. 4.7| Theoretical values for the enhancement factor per unit waveguide length for bulk sensing, Φ compared to the confocal microscope as a function of waveguide width for strip and slot silicon nitride waveguides and $\lambda_0 = 785$ nm.

spectrometer (AvaSpec-ULS2048XL) are employed. An inverted configuration is used for the microscope to avoid any artefacts, which may result due to contact with the surface of the liquid analyte or due to evaporation of the analyte. IPA was contained in a Raman grade low background quartz receptacle with 0.17 mm bottom thickness. Several objectives corrected for 0.17 mm cover slip were used for the measurement to optimally couple light in the 100 μm diameter collection fiber that also acts as the pin-hole. Among 60x/0.8 NA, 20x/0.5NA and 10x/0.3 NA objectives, *Nikon CFI Plan Fluor 10x/0.3* gave the highest signal and is used for the measurement of the spectra for comparison with the waveguide approach.

Fig. 4.7 shows the Raman spectra of the IPA droplets collected using slotted waveguides, strip waveguides and the commercial microscope. The spectra are normalized by the respective values of the peak at 819 cm^{-1} . Fig. 4.7 also shows the plot of SNR versus ζ defined by Eq. (4.4) for various measured spectra for the 819 cm^{-1} peak of IPA. We verify that photon counts of the spectrometer-CCD follow Poisson statistics (see Appendix B). Thus, we define SNR as:

$$SNR \equiv \frac{C_{819} - C_B}{\sqrt{C_{819}}} \quad (4.5)$$

where, C_{819} is the average number of photon counts of the 819 cm^{-1} IPA peak (including the background) and C_B is the average number of background photon counts near the bottom of the 819 cm^{-1} peak corresponding to the background from the waveguides. All the spectra are normalized for 10 mW input power and 10 s integration time. The effect of an estimated 8 dB/facet coupling losses in the measurement of the signal from the waveguides has also been taken into account to compare with the free-space approach.

In Fig. 4.7, we observe that the spectrum from the confocal microscopes con-

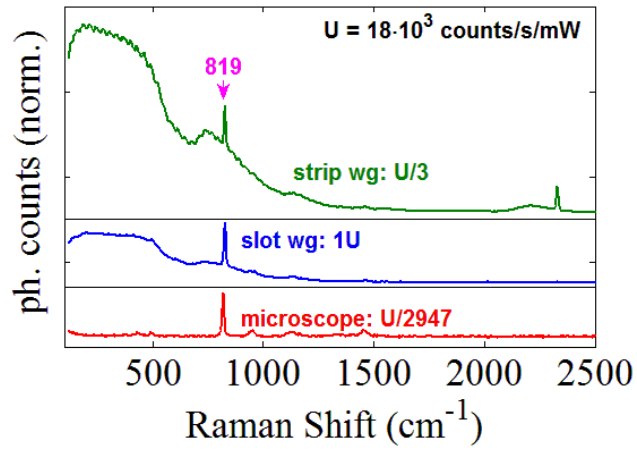


Fig. 4.7 | Raman spectra of IPA measured with the microscope (red, bottom), slot waveguide (blue, middle) and strip waveguide (green, top) and. The spectra are shifted vertically for clarity with their respective zeros shown by a black line, and normalized for the IPA peak at 819 cm^{-1} (shown with an arrow in magenta). (from [50])

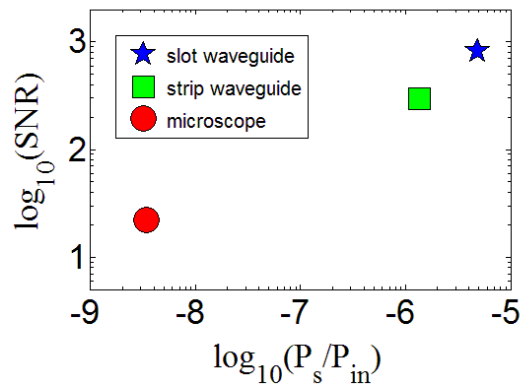


Fig. 4.8 | The SNR vs collection efficiency for microscope (red circle), strip waveguide (green square) and slot waveguide (blue star). (from [50])

tained only the dark-noise from the spectrometer and contained negligible background. This is anticipated because the signal was taken directly from IPA at the confocal volume and a low-background Raman grade quartz receptacle was used. In contrast, the spectrum collected from the waveguides is composed of the Raman signal from the analyte and the background originating from the Si_3N_4 core of the waveguide (discussed in detail in Chapter 7). Nevertheless, from Fig. 4.8 one can observe that in comparison to the confocal microscopic systems, about 3 orders of magnitude higher signal is obtained from the waveguides resulting in a large improvement in the SNR. Note that compared to the strip waveguides, the slotted waveguides have lower background relative to the corresponding IPA peak. This can be explained by the strong enhancement of the field in the slotted region resulting in a stronger interaction with the analyte (see Chapter 6). In contrast, for strip waveguides, the maximum intensity lies in the Si_3N_4 core region thus collecting more background from it. Use of a slotted waveguide configuration also leads to about an eight-fold enhancement in the signal strength compared to the strip waveguide. Therefore, a significantly higher SNR can be observed for the slotted waveguides.

In conclusion, because of the enhancement of the collected Raman signal in waveguide-based evanescent Raman spectroscopy, a higher SNR and collection efficiency are obtained in comparison to the confocal microscope despite the background noise from the waveguide core. The SNR can further be lowered by appropriate waveguide designs such as the slotted waveguide that enhances the interacting field intensity in the analyte region.

4.6 Closing Remarks

The reported experiments and simulations are performed for IPA as the analyte in the uppercladding. However, the experimental and theoretical assessments have also been performed using other liquid and solid analytes, such as, acetone, dimethyl sulfoxide, and spin coated photoresists. The confinement properties of the waveguide mode changes if the refractive index of the uppercladding varies; therefore, according to Eq. (4.1) the numerical values of the conversion efficiency will slightly differ. Nonetheless, the results discussed in this article are pertinent for analytes of general interest such as a glucose solution.

5

NWERS of Monolayers and thin layers

In the previous chapter we saw that for the bulk materials placed on the top of the waveguides, the use of Si_3N_4 waveguide provides a signal more than 2 orders of magnitudes compared to the free-space methods. The comparative advantage of the nanophotonic waveguide enhanced Raman spectroscopy (NWERS) approach is more prominent for a monolayer of molecules functionalized on top of the waveguides. It is because the evanescent interaction is much stronger near the surface of the waveguide (§3.5) in addition to integration of the signal along the waveguide. In this chapter, we discuss evanescent Raman spectroscopy of monolayers. It will be shown that this method provides a signal which is four orders of magnitude greater than that for the most ideal free-space Raman system, even with a one centimeter long waveguide. This huge enhancement of the signal leads to an integration time for a realistic waveguide system that is reduced by almost six orders of magnitude in comparison with a commercial Raman microscope system. The enhancement and reduced signal acquisition time open up new opportunities in the applications of Raman spectroscopy for monolayers, such as, monitoring of the biological and chemical processes with highly specific, quantitative and informative spontaneous Raman signals in real-time in the NIR wavelength region. We will also discuss observation of DNA hybridization process in real time and subsequently extract the relevant experimental parameters such as association constant and hybridization density. Furthermore, we show that the specificity of the Raman signal combined with the quantitative nature of the enhancement allows us to accurately detect and quantify sub-monolayers of biotin and streptavidin molecules. The content of this chapter has been submitted for peer reviewed publication with a

title, “Nanophotonic waveguide enhanced Raman spectroscopy of biological sub-monolayers on a CMOS-compatible platform”.

5.1 Importance of Raman spectroscopy of Monolayers

Monolayers or thin layers of materials are ubiquitous in nature and play a critical role in modern instrumentation and technology [52]. Many important physico-chemical and biological interactions of cells happen at the level of surfaces and interfaces, such as cell-membranes [53]- [54]. The study of layers at the bio-interfaces is crucial for applications ranging from clinical diagnostics, genomics, proteomics, and biomaterials to tissue engineering [52] - [60]. Furthermore, there is an emergence of numerous interesting physical processes and novel optoelectronic applications that use 2D monolayers of materials such as graphene [60] and graphene-like 2D materials [61] - [62]. Hence, a paramount importance is placed on understanding the structural, physical and biochemical properties of monolayers or very thin layers of molecules.

In monolayer research, there is a need for a precise tool that provides consolidated information about composition, molecular structure, and density of the surface molecules. Simultaneously characterizing the kinetics of the bio-chemical interactions at interfaces is equally important in many applications [52]- [59], such as the study of DNA hybridization. Obtaining such consolidated information from monolayers is particularly challenging because only a small number of molecules contribute to the signal. The prevalent techniques such as scanning probe microscopy (SPM) [63], X-ray based techniques [64] [65] and nuclear magnetic resonance microscopy [67] are often invasive, expensive, necessitate a long time for sample preparation and data acquisition, and require a restrictive environment for samples. As such, existing techniques for monolayer characterization are unsuitable for a variety of applications.

Raman spectroscopy is a powerful technique, and is particularly well-suited for identification and quantification of various physicochemical properties of molecules. Raman spectroscopy has been successfully used for the characterization of monolayers of materials such as graphene that have a high Raman scattering efficiency [68] or via a pump wavelength resonant to the fluorescence that allows for a huge enhancement in the Raman signal [69]. Very thin layers of small Raman cross-section molecules, such as nucleic acids, proteins or lipids, present a major challenge for this technique, because the associated signal acquisition times to obtain a sufficient signal-to-noise ratio (SNR) are impractically long. This is especially the case for near-infrared (NIR) wavelengths, where auto-fluorescence background from most of the biological materials is weak, yet, unfortunately the

Raman scattering cross-sections are also very small. Surface enhanced Raman scattering (SERS) has been used to mitigate this problem [70] [71] by means of electromagnetic enhancement due to surface plasmon resonance effects. SERS has been successfully used for an extreme signal enhancement, leading to enhancement that allow even detection of single molecules [72]. However, SERS signals depend strongly on geometrical features at the nanoscale and the resultant variations from one substrate to another necessitate sophisticated fabrication techniques for reproducibility and uniformity [72]- [74]. Tip enhanced Raman spectroscopy (TERS), a technique combining SPM with a SERS nano-tip to greatly enhance the signal, has been recently used to study polymer monolayers [75], albeit with the disadvantages of long integration time and inhomogeneity of signal strength inherent to SPM and SERS.

Here we report a real-time observation of immobilized DNA hybridization and an accurate and direct measurement of the density of sub-monolayers of biotin-streptavidin complex using this on-chip nanophotonic waveguide enhanced Raman spectroscopy (NWERS) technique. This prospect emerges as a consequence of electromagnetic enhancement and an increase in number of the probed molecules, bringing about an enormous reduction of the integration time for a practical SNR. The following section describes this matter in detail.

5.2 Collection efficiency for monolayers

For a monolayer of molecules with surface density ρ_s uniformly distributed over a transversely symmetric waveguide of length l , the total normalized surface conversion efficiency for the waveguide system is given by the sum of individual incoherent contributions from each molecule:

$$\begin{aligned} \frac{P_{w,s}}{P_{in}} &= \sigma \rho_s l \int_{line} \Lambda_{1D}(\vec{r}) d\vec{r} \\ &= l \rho_s \sigma \eta_s \end{aligned} \quad (5.1)$$

where, Λ_{1D} is the integrated luminosity of the waveguide introduced in Chapter 3. The line integral is defined along the interface between the core and upper cladding (Fig. 5.1) on an arbitrary section of a waveguide. We call the integral, η_s the *specific surface conversion efficiency* and given by Eq. (5.2).

$$\eta_s \equiv \int_{line} \Lambda_{1D}(\vec{r}) d\vec{r} \quad (5.2)$$

For the similar monolayer when excited and collected by a diffraction limited free-space system, the interaction area is limited by the beam waist. As we saw in Chapter 2, the power emitted *in every direction* when excited by a Gaussian beam is given by, $P_{DL,s} = P_{in} \sigma \rho_s$.

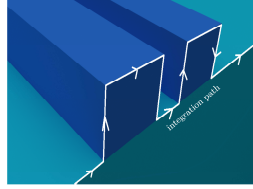


Fig. 5.1|The integration path to calculate η_s . The surface integral can be reduced to the line integral along the path (shown in white) for uniformly distributed molecules on top of the longitudinally invariant waveguide.

Hence,

$$\bar{P}_{w,s} \equiv \frac{P_{w,s}}{P_{DL,s}} = l\eta_s \quad (5.3)$$

Fig. 5.2 (a) shows the surface efficiency η_s calculated for Si_3N_4 strip and slot waveguides using the COMSOL mode solver for various geometries.

In a practical situation where a large NA optics is used for signal collection, only the signal emitted in the either of the half-spaces can be measured. In a similar manner, either of forward or backward propagating signals is generally measured using waveguide systems. Thus, Eq. (5.3) is also a good approximation for comparisons in practical situations.

5.3 Experiments

5.3.1 Demonstration of enhancement

To measure the Raman signal from the waveguides in comparison to the case of a Raman microscope, we functionalize a monolayer of Rhodamine molecules on an amino-silanized Si_3N_4 waveguide surface. The setup used to measure the collected Raman signal from the waveguides has been explained in §4.3.1. We use a $w = 850$ nm slotted waveguide with $s = 150$ nm (Fig. 1(c)). The measured spectrum is shown in Fig 2(b). For all waveguide measurements, an integration time of 4 s was enough to obtain a signal to noise ratio (SNR) of 50 or more. The noise is mainly dominated by the shot noise of the Raman signal and the background from waveguide.

Fig. 5.2(b) also shows the spectra measured from a Rhodamine-functionalized Raman-grade calcium fluoride (CaF_2) slide measured using a commercial Raman confocal microscope and a CCD detector with similar characteristics. To be able to measure much weaker Raman signals from the monolayers using a microscope, it is important to have a low background material because the microscope cannot discriminate the background from the other materials in the focal volume. We

use Raman grade calcium fluoride (CaF_2) microscope slides for the measurements with the Raman microscope as it exhibits very low Raman background compared to the stack of materials used for the fabrication of the waveguides. A 7 ± 2 nm layer of similar Si_3N_4 is deposited on CaF_2 slides and functionalized together with the Si_3N_4 waveguide samples to ensure that both of the samples have similar density of molecules. For the spectra obtained with the Raman microscope, the noise is mainly dominated by the dark noise of the detector, as the signal is very low. A pump power of 18 mW and integration time of 80 s was required to obtain a SNR of around 8.

Thus, even ignoring a total of 18 dB losses, mainly from coupling losses, we clearly observe a very strong enhancement of the Raman signal from the waveguides. For a fair comparison, we normalize the observed signal P_s with the transmitted pump power P_{tx} so as to correct for the variations in the coupling losses in the system which are extrinsic to the waveguide approach and can be eliminated by optimized coupling mechanism or by integrating the sources and detectors on the chip. The normalized collected power ζ , introduced in Chapter 4 and redefined for surface conversion efficiency in Eq. (5.4), is related directly to the intrinsic variables of the system and will be used for the comparison.

$$\zeta(l) \equiv \frac{P_{col}(l)}{P_{tx}(l)} = \frac{\rho\sigma\eta_s}{2} \left[\frac{e^{\delta\alpha l} - 1}{\delta\alpha} \right] = \frac{\eta_s}{2} \sigma\rho_s l (1 + \Delta) \quad (5.4)$$

Fig. 5.2 (c) confirms more than four orders of magnitude enhancement in the signal from only one centimeter of waveguide length, in accordance with the prediction from the theory shown in Fig. 5.2 (a). In addition, we see that compared to commercial microscopic systems, the enhancement of the NWERS signal leads to more than two orders of magnitude improvement in SNR.

Fig. 5.3 illustrates the evolution of SNR as the density of the molecules or the cross-section of the molecules is varied, also calculated using the data shown in Fig. 5.2(b) (see Appendix C for the details of calculation of SNR). More than two orders of magnitude improvement of SNR or limit of detection (LoD) is expected with the NWERS for the same pump power and the same integration time. If the shot noise from the waveguide background can be reduced, the improvement of SNR or LoD can approach to four orders of magnitude. Seen from a slightly different perspective, depending on the dominating source of noise and the concentration of analyte, the NWERS approach leads to 4 to 8 orders (see Appendix C) of reduction in the integration time compared to the free-space system for a similar SNR and pump power. Further, as can be seen in Fig 5.2(a), the surface efficiency value η_s is practically invariant with small variations in the waveguide dimensions that might occur during fabrication ($<4\%$ for a variation of 20 nm); hence η_s will remain very close to the calculated value in average [49]. Our results for NWERS break the impasse of impractically long integration times and unpredictable signal

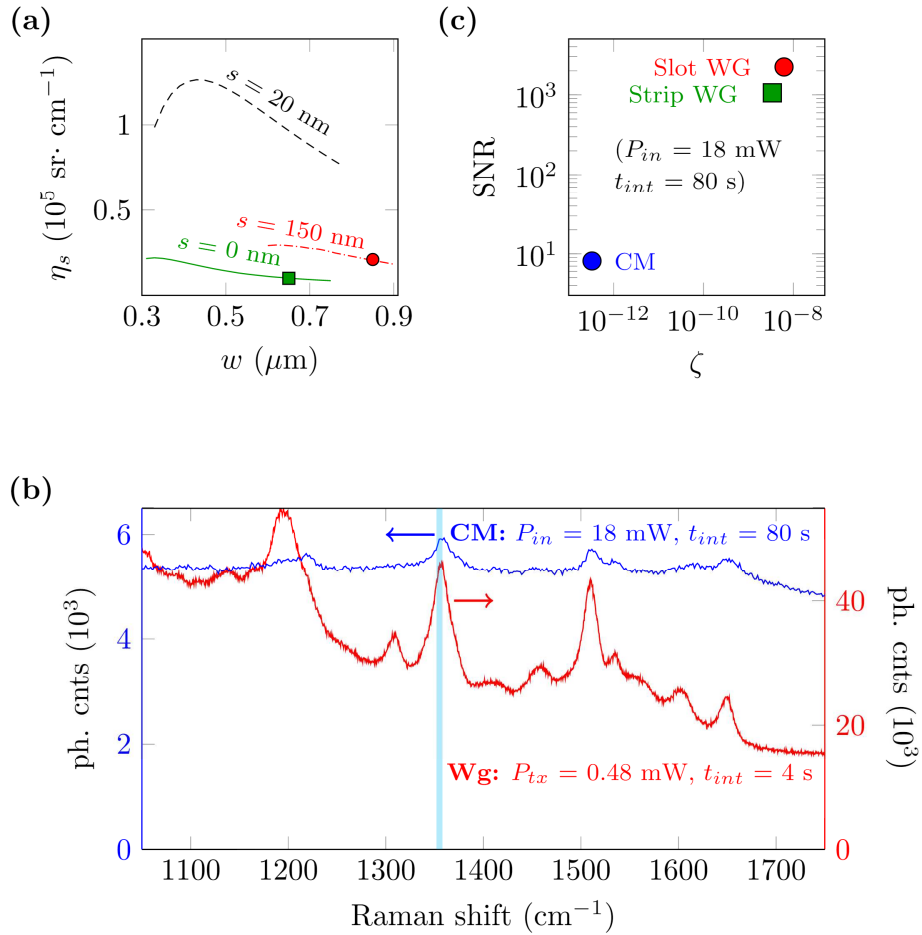


Fig. 5.2|Enhancement of signal and improvement of SNR with NWERS. (a) The calculated values of the η_s for NWERS system for $h = 220 \text{ nm}$, slot widths $s = 0, 20 \text{ nm}$ and 150 nm as a function of waveguide width w . The waveguides used in the experiments are marked with circles. (b) The measured spectra of a Rhodamine monolayer obtained from a commercial Raman microscope (CM, $P_{in} = 18 \text{ mW}$ and $t_{int} = 80 \text{ s}$, in blue with left blue axis) in contrast to the spectra obtained from the 1 cm slot waveguides (Wg, $P_{in} = 30 \text{ mW}$, $P_{tx} = 0.48 \text{ mW}$ and $t_{int} = 4 \text{ s}$, in red with right red axis). (c) SNR vs conversion ratio ζ for the 1355 cm^{-1} line (highlighted with cyan in (b)) from rhodamine monolayers obtained from a commercial microscope (CM), slotted waveguides (red) and strip waveguides (green).

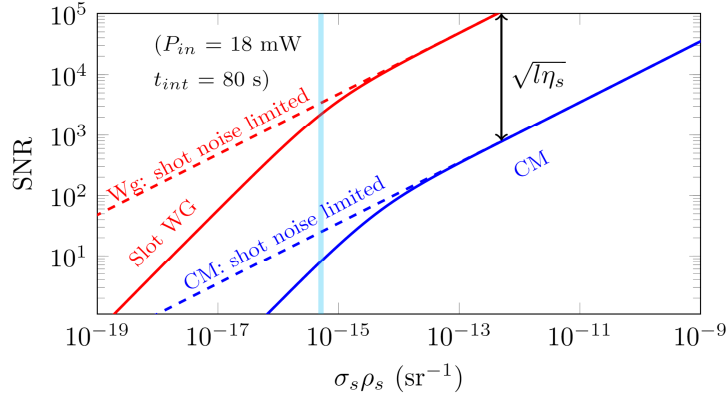


Fig. 5.3 Evolution of SNR for different $\rho_s \sigma$ based on the data presented in Fig. 5.2 (b) and highlighted by a cyan bar in the figure (solid lines). Evolution of SNR for the ideal cases, when shot-noise from the signal is the only source of noise, is also shown in dashed lines for the respective systems.

enhancement that several potential applications of Raman spectroscopy are facing. Such an asset of NWERS is implemented for two different applications described subsequently in this chapter. In the next section, we outline real-time observation of DNA hybridization on the surface of silicon nitride waveguides using NWERS.

5.4 DNA hybridization kinetics using spontaneous Raman signal

DNA microarrays are indispensable tools in modern biotechnology with a broad range of applications from gene expression profiling and drug discovery to forensics [57] [58]. In DNA microarrays, one of the strands of nucleic acid (probe DNA) is immobilized on a solid surface and the complimentary (cDNA) strand of nucleic acid in analyte solution is detected with extremely high specificity. During the hybridization process the analyte identifies and binds to its complementary target. This process is regarded as the most critical element of nucleic acid-based biosensor technology [77]. A reliable, cost-effective and sensitive quantification method for real-time analysis of DNA hybridization has been identified as a key necessity to broaden the range of applications of the DNA microarrays [57]. Here we demonstrate a real-time analysis of DNA hybridization using NWERS, with an enormous prospective for large scale integration and parallelization.

Oligonucleotide strands (DNA: 5' - /hexynyl/-TTT TTT TTT TCA CCA GCT CCA ACT ACC AC -3') of K-Ras gene - an important gene the activation of which is responsible for 17-25% of all human cancer tumors [78], are immobilized on our chips using *copper-catalyzed alkyne-azide 1,3-dipolar cycloaddition* reaction on a

silanized surface. The density of DNA probes was estimated to be about $6 \pm 1 \cdot 10^{12} \text{ cm}^{-2}$, based on measurement of P-concentration by total X-ray fluorescence spectroscopy. A 500 nM solution of cDNA with cy3 marker (5' - /cy3/- GTG GTA GTT GGA GCT GAA AAA AAA AA -3'), in a 0.5M NaCl/TE buffer is used as analyte for the hybridization process.

Initially, a 150 μl of buffer is drop-casted on the chip to measure the Raman spectra from the chip with immobilized hexynyl-DNA in buffer. At time $t = 60 \text{ s}$, 15 μl of cDNA is added on the chip and the changes of the Raman spectrum are monitored until a stationary regime is reached. The changes in the Raman spectrum are directly related to the hybridization kinetics (see Appendix C) hence a stationary Raman spectrum indicates a saturation of the reaction. The hybridization reaction saturates in about 250 s after application of the cDNA solution. Figure 5.4(a) shows the spectrogram of the observed Raman spectra collected from the chip as it evolves during the hybridization process. Each spectrum is measured every two seconds with about 0.25 mW effective powers in the waveguide and corrected for the background from the waveguide (Chapter 8). Fig. 5.4(b) shows the Raman spectra of the immobilized hexynyl-DNA complex in buffer (at $t = 6 \text{ s}$) and Raman spectra of the DNA hybridization duplex (hexynyl-DNA-cDNA-Cy3) after the hybridization reaction saturates ($t = 250 \text{ s}$). The reaction kinetics can be quantified via one of the peaks corresponding to cDNA. In our case, we choose the 1392 cm^{-1} line of cy3 for its distinctive nature.

As seen in Fig. 5.4(c), the reaction kinetic observed using the 1392 cm^{-1} Raman line fits well with the first order Langmuir equation [79]- [80] (see Appendix C): $\zeta(\tau) = \zeta_{\infty} \{1 - e^{-K_1 \rho_A \tau}\}$. In the present case, $\zeta(\tau)$ is the normalized Raman signal intensity collected through the waveguide at a time τ after the start of the reaction, ζ_{∞} is the normalized Raman signal corresponding to the total number of binding sites i.e Raman signal at the time of saturation ρ_A is the concentration of the reacting analyte on the chip ($\rho_A = 45.4 \text{ nM}$ in this study). The least-square-error fit to the above equation yielded a goodness of fit $R^2 = 0.95$. The association constant K_1 is estimated to be $2.9 \pm 0.6 \cdot 10^5 \text{ M}^{-1} \text{ s}^{-1}$ from the fit. A higher temperature $\sim 26^\circ \text{ C}$ of our experiments may explain the slightly higher value we obtained compared to values reported in the literature ($1.2 \cdot 10^5 \text{ M}^{-1} \text{ s}^{-1}$ for 20° C) [79]- [80] under otherwise similar experimental conditions such as chain length, target concentration and probe density.

Although cDNA with a marker label is used in this proof of concept experiment, a natural next step is a label-free measurement of hybridization kinetics using NWERS. For this purpose changes in the Raman spectra of the nucleic acids during hybridization have to be identified and quantified. The current spectra are overwhelmed by the Raman signal from cy3 dye, hence are not suitable for identification of such changes during hybridization.

Since ζ_{∞} in Fig. 5.4, is the normalized Raman signal corresponding to a

known probe density, we can use Eq. (5.4) to accurately determine the spontaneous scattering cross-section of the analyte molecules corresponding to a Raman peak (see §5.6). Once the cross-section of a molecule is determined, the NWERS technique can be used to calculate the loading density of the probes, in a future experiment, without a need for determination of probe density that would otherwise require specialized techniques such as XFS. In the next section we discuss this application of NWERS for a robust quantification of the surface loading in another important biological assay based on biotin-avidin binding. There are several indirect techniques for the study of hybridization kinetics [79]- [81]. The appeal of the proposed NWERS is its simplicity and a direct correspondence of the spontaneous Raman signals with the number of the probed molecules. This makes NWERS intrinsically robust against the non-specific binding, photo damage, and photo bleaching that constitute a major source of error in most of the existing techniques, such as those based on fluorescence, X-rays or a microbalance.

5.5 Quantification of surface loading for a submonolayer of biotin and biotin-streptavidin complex

Thanks to its unique structure and small size, biotin shows specific and very strong non-covalent binding to particular proteins such as avidin and histone, without significantly altering the biological activity of the molecules in its surrounding [82]- [85]. Hence, biotin-based assays have been an indispensable tool in modern biotechnology [82] for the detection and localization of specific proteins, nucleic acids, lipids, and carbohydrates. Here, we demonstrate that NWERS can allow direct detection of amino-silane precursor generally used for functionalization, biotin, and NeutrAvidin and can be used for quantification of the biotin-StreptAvidin loading density when applied to the biotin based assays.

To this end, we incubate biotinylated chips with unconjugated NeutrAvidin and StreptAvidin conjugated with Rhodamine red. These avidin derivatives are known to bind with high specificity to the biotinylated surface of the chips [84]. Fig. 5.5(a) depicts a schematic of molecules attached to the waveguides at various stages of functionalization process. Typical Raman spectra obtained from the chips corresponding to these stages are shown in Fig 5.5(b). We see several peaks corresponding to the molecules that are present at the specific stages of functionalization. Specifically, spontaneous Raman signals from monolayers of functionalized *3-aminopropyltriethoxysilane* [86]– (henceforth, referred to as amino-silane (AS)), biotin [71], [87] covalently bound to AS (AS-B), NeutrAvidin [87] non-covalently bound to functionalized biotin (AS-B·NA), and StreptAvidin-Rhodamine [88] [89] conjugate bound to functionalized biotin (AS-B·SA-Rh) can all be detected with acquisition times in the order of a few seconds with a SNR >10.

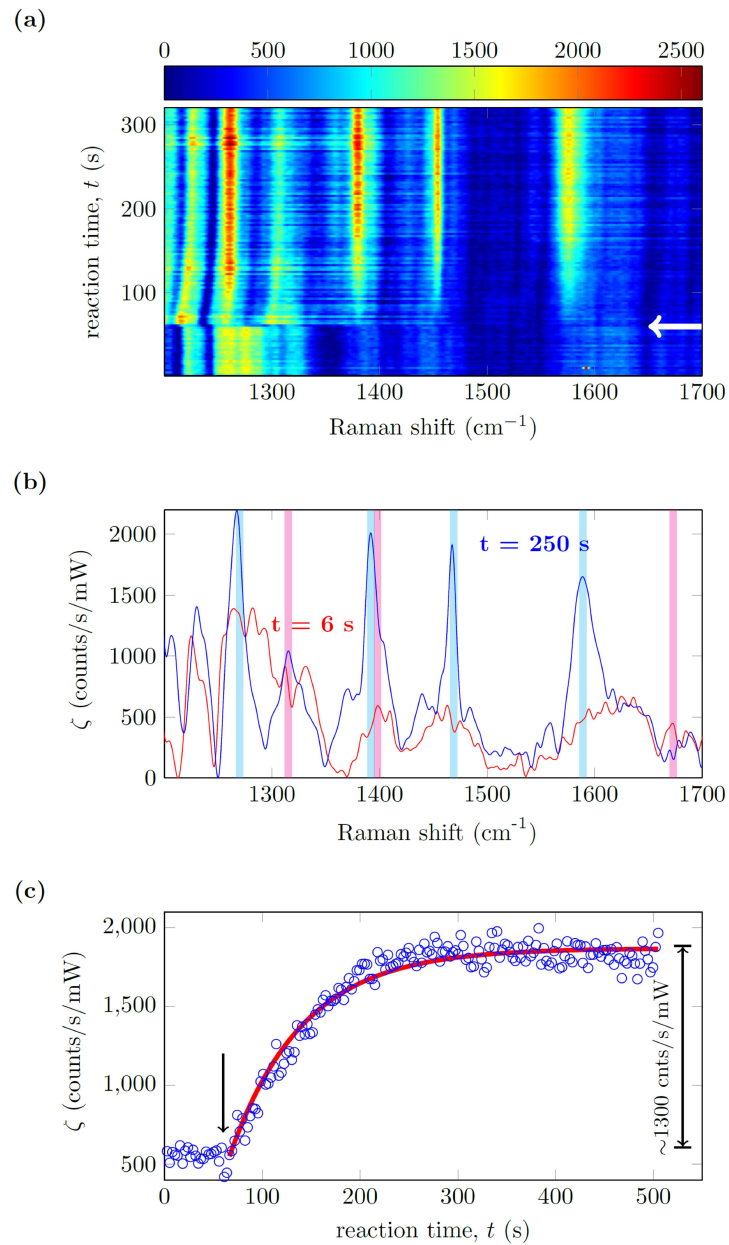


Fig. 5.4] Real time observation of DNA hybridization process using NWERS. (a) Raman spectrogram as a function of reaction time t . cDNA-Cy3 was added at $t = 60$ s (indicated by an arrow). (b) The Raman spectra before addition of the cDNA ($t = 6$ s, red) and after the saturation of hybridization reaction ($t = 250$ s, blue). Cyan and magenta are respectively Raman lines from cy3 and nucleic acids (c) The Raman signal (blue circles), corresponding to the 1392 cm^{-1} line of cy3, follows the first order reaction equation (red line) with goodness of fit $R^2 = 0.952$.

Functionalized AS display broadband features centered at $\sim 1600 \text{ cm}^{-1}$, $\sim 1415 \text{ cm}^{-1}$ and $\sim 1165 \text{ cm}^{-1}$ respectively assigned [86] to amide deformations, C-N stretch in primary amines, and CH_2 deformations. The important features [71] [87] of the AS-B spectra are centered around $\sim 1310 \text{ cm}^{-1}$ ($\gamma\text{-CH}_2$), $\sim 1442 \text{ cm}^{-1}$ ($\delta\text{-CH}_2$, $\delta\text{-CH}_3$) and $\sim 1630 \text{ cm}^{-1}$ (Biotin Ureido ring stretching). Similarly, the spectra with biotin-avidin [71] [87] contained all the features of the biotin precursor and some extra peaks centered at $\sim 1132 \text{ cm}^{-1}$ (Trp W7), $\sim 1250 \text{ cm}^{-1}$ (Amide III), $\sim 1550 \text{ cm}^{-1}$ (Trp W3), $\sim 1668 \text{ cm}^{-1}$ (Amide I). The spectrum due to AS-B-SA-Rh complex is overwhelmed by the spectral features of Rhodamine, which has more than an order of magnitude higher cross-section compared to that of the precursor molecules. Incidentally we note that, under assumptions of identical loading density across all the functionalized chips, the respective peak amplitudes assigned to different molecules can be used to estimate their relative Raman cross-sections.

To accurately determine the number of streptavidin molecules attached to the surface of our chips, we measure the signal from streptavidin–Rhodamine red conjugate from the biotinylated chip containing the waveguides of lengths 1 cm, 2 cm, 3 cm and 4 cm. The normalized collected power ζ (for the 1513 cm^{-1} Rhodamine line) was measured for different lengths of waveguides using a spectrometer with calibrated CCD. The chip containing Rhodamine is selected, as Rhodamine is a well-studied Raman reporter and its cross-section is well documented. From literature we estimate σ for the 1513 cm^{-1} line of Rhodamine used for the experiment to be about $2.8 \cdot 10^{-27} \text{ cm}^2 \cdot \text{sr}^{-1} \cdot \text{molecule}^{-1}$ at 785 nm [88]- [89] and use $\eta_s = 2.1 \cdot 10^4 \text{ sr} \cdot \text{cm}^{-1}$. Using these values of $\sigma\eta_s$ and the measured ζ , we can determine experimental values of $\rho_s\sigma(1 + \Delta) = 2\zeta/(l\sigma\eta_s)$ for different waveguide lengths. These values are nearly equal to the number of molecules adsorbed on the waveguides, aside from the contribution of the factor Δ shown in Eq. (5.4). To determine this contribution we fit the observed data with Eq. (5.4) as a model using the least-square error fitting algorithm. Fig 5.5(c) shows the plot for $2\zeta/(l\sigma\eta_s)$ as a function of waveguide length l with respective experimental errors. The dominating source of error in our measurements is the vibration of the coupling mechanism discussed in Chapter 4. A goodness of fit $R^2 = 0.995$ is obtained and yields a surface loading of $1.0 \pm 0.2 \cdot 10^{11} \text{ molecules/cm}^2$ and $\delta\alpha = -1.3 \pm 0.2 \text{ dB/cm}$. Our value for surface density is about 1% of a closely packed monolayer of streptavidin molecules ($\sim 1 \cdot 10^{13} \text{ molecules/cm}^2$) [90]. Thus, we see that neglecting Δ leads to about 15% underestimation of surface density values for a 1 cm waveguide for $\sim 105 \text{ nm}$ difference of the pump and Stokes wavelengths, and for waveguide loss of $\sim 2.5 \text{ dB/cm}$ at 785 nm.

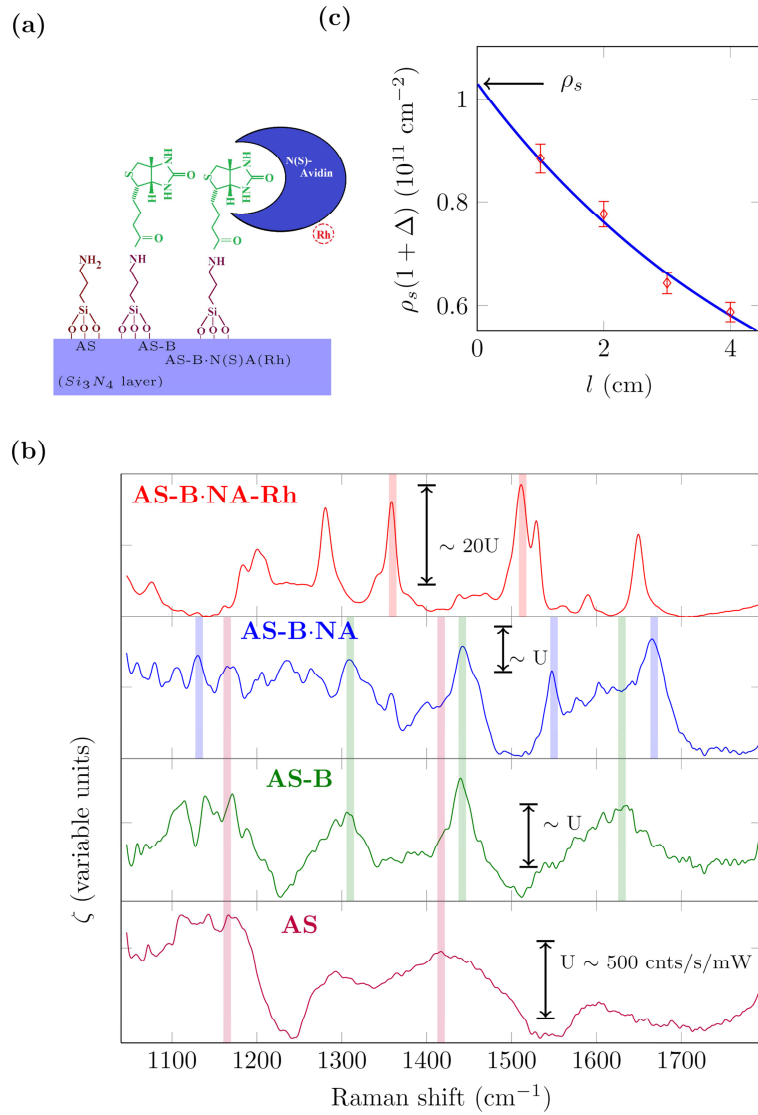


Fig. 5.5|Detection and quantification of Biotin-Avidin monolayers (a) Schematic of immobilized monolayers at different stages of functionalization. APTES amino-silane (AS), biotin (B) covalently bound to AS (AS-B), NeutrAvidin (NA) or Streptavidin conjugated with Rhodamine (SA-Rh) attached to AS-B with non-covalent bond (AS-B·NA(SA-Rh)) are depicted. (b) Raman spectrum of AS (brown), AS-B (green), AS-B·NA (blue) and B-AS-B·SA-Rh (red). The vertical transparent lines of respective colors indicate the Raman peaks due to the corresponding molecules as found in the literature. (c) Dependence of the $\rho_s(1 + \Delta)$ as a function of waveguide length calculated using 1513 cm^{-1} Rhodamine Raman signal obtained from B-AS-B·SA-Rh attached to biotin. The red diamonds are the experimental values and the blue line is the least squared error fit with Eq. (5.4) as a model. Estimated molecular density ρ_s is shown by an arrow corresponding to $l \sim 0$, where the effect of Δ is negligible.

5.6 Determination of the cross-section of cy3

The value of ζ_∞ corresponding to the 1392 cm^{-1} line of Cy3 molecules was experimentally determined to be $1.3 \cdot 10^3$ counts/s/mW (Fig 5.4 (c)). The detector sensitivity is determined to be $1.9 \cdot 10^{15}$ counts/s/mW. This allows us to calculate $\zeta_\infty = 6.7 \cdot 10^{-13}$ in absolute units. We take $\eta_s = 2.1 \cdot 10^4 \text{ sr cm}^{-1}$ obtained from the simulations. As discussed in the main text, the surface efficiency value η_s is tolerant to small variations in the waveguide that might occur during fabrication hence we expect η_s to be very close to the simulated value. X-ray fluorescence spectroscopy data provides us the density of the DNA probes $\rho_s = 6 \pm 1 \cdot 10^{-13}$. Hence, using Eq. (5.4) for a 1 cm long waveguide, we determine $\sigma(1 + \Delta)$ for the 1392 cm^{-1} line of Cy3 to be $1.1 \pm 0.2 \cdot 10^{-29} \text{ cm}^2 \text{sr}^{-1} \text{molecule}^{-1}$. As seen Fig. 5.5 (c), Δ accounts for about 15% underestimation of the parameters for the 1 cm waveguide. Thus, $\sigma = 1.3 \pm 0.2 \cdot 10^{-29} \text{ cm}^2 \text{sr}^{-1} \text{molecule}^{-1}$ for the 1392 cm^{-1} line of Cy3 when pumped at 785 nm.

5.7 Raman spectroscopy of cell-membranes

In this section, the membranes of cells fixed on a photonic chip will be investigated using NWERS technique. We will see that the enhancement and exponential nature of the evanescent interaction allow for selectively probing the membrane with higher efficiency and higher selectivity compared to a confocal microscope.

5.7.1 Importance of Raman spectroscopy of Cell-membranes

The cell membrane is a complex arrangement of phospholipids, proteins and carbohydrates. These membrane-bound molecules regulate most of the vital biological activities of the cells by controlling the trans-membrane and intracellular transport. Due to the lack of sensitive, selective and in-situ tools, the study of these membrane-bound molecules is largely done in isolation from the cells or from the membranes. Damaging methods of enrichment such as centrifugation are used to enhance the signal. The fact that about 60 % of all drugs target the activity of native membrane molecules underscores the importance of having a selective Raman tool for the study of cell membranes in its natural state [93]. Here we report the possibility of using a lab-on-a-chip method to obtain selective Raman spectra from the cell-membranes of the cells grown directly on a chip.

5.7.2 Biocompatibility of Silicon Nitride and growth process

First we note that the SiO_2 and Si_3N_4 materials used for our waveguides are not adverse to the overall cell growth and are routinely used as biocompatible materials for the cell culture [94]. Further, as shown in Fig. 5.6 and Fig. 5.7, the cells

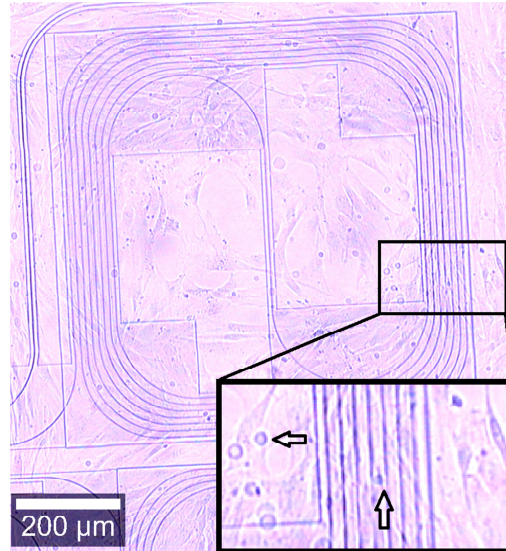


Fig.5.6] Microscope image of the HeLa cells grown on top of a Si_3N_4 waveguide spiral carrying the pump laser as well as the Raman signal. The rectangular selection in the base zooms in a section of the top of the spiral where the cells and possibly their organelles, such as the nucleus, (shown with arrows) can be seen.

adhere to the waveguide and the membrane following its topography, such that the evanescent tail of the waveguide mode interacts with the membrane, allowing one to probe exclusively the region very close to the waveguides. For 850 nm wide slotted waveguides (inclusive of a 150 nm slot region) we use the collected Raman signal halves every 20 nm away from the waveguide surface.

HeLa cells (ATCC) were cultured in Advanced Dulbecco's Modified Eagle's Medium (GIBCO-LT-12491-015) supplemented with 2% fetal bovine serum (GIBCO-LT-10500-056) and 1 % penicillin-streptomycin-L-glutamine (GIBCO-LT-10378-016), and grown in culture flasks containing a Si_3N_4 chip and a CaF slide in an incubator at 37 °C and 5% CO_2 . CaF slide was used to obtain the spectra with a confocal microscope for comparison. Prior to fixation, cells were washed in the phosphate buffered saline (PBS). Fixation on the Si_3N_4 chip and CaF slide was performed for 10 minutes in 4% paraformaldehyde solution, after which cells were washed three times and stored in PBS.

5.7.3 Spectrum of the cells

Fig. 5.8 illustrates the background-subtracted Raman spectra of HeLa cells measured using a commercial confocal microscope (WITec Alpha300R+ confocal Raman microscope) by specifically focusing at the cell membrane using a z-scan,

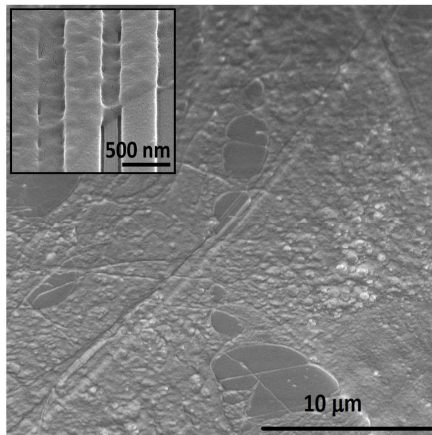


Fig. 5.7 | A SEM micrograph of a cell fixed to the surface of the Si_3N_4 - SiO_2 chip. A good adhesion of the cells with the surface of the chip is observed.

with a confocal height of $1.5 \mu\text{m}$. This limited z -resolution inhibits a selective probing of the cell membrane, a problem which is resolved using our on-chip approach. The figure also shows two background-subtracted example spectra of the cells grown on the chip and measured by evanescently exciting and collecting the membrane molecules using the waveguide. The typical integration times were less than 10 s for an effective pump power of $500 \mu\text{W}$ in the waveguide to obtain a signal-to-noise ratio (SNR) > 50 . To obtain a spectrum with a similar SNR using similar pump power, the integration time needed for a confocal microscope would be > 500 s.

To simulate cell membranes consisting of only lipids, the spectrum of a lipid bilayer formed on the chip using the vesicle [95] (using vesicles formed by 4:4:2 mixture of dioleoyl phosphatidylethanolamine, dioleoyl phosphatidyl choline, and Cholesterol) and evanescently measured using the waveguides is displayed. In contrast to the spectrum of the lipid bilayer, the spectra of the cells additionally contain distinctive peaks [96] due to proteins and nucleic acids. The spectra measured using the waveguide have some similarity with the one obtained using the confocal microscope, but several distinctive peaks due to proteins and nucleic acids become more prominent with the waveguide due to exclusivity and localization of the Raman interaction near the membranes.

Interestingly, the spectra of the cells differ from one waveguide to another while retaining certain general characteristics, such as the peaks related to lipid. A possible reason for this difference between the spectra of the membranes can be the complex and heterogeneous nature of the cell membrane that alters significantly depending on the stress conditions of the individual cells in their respective

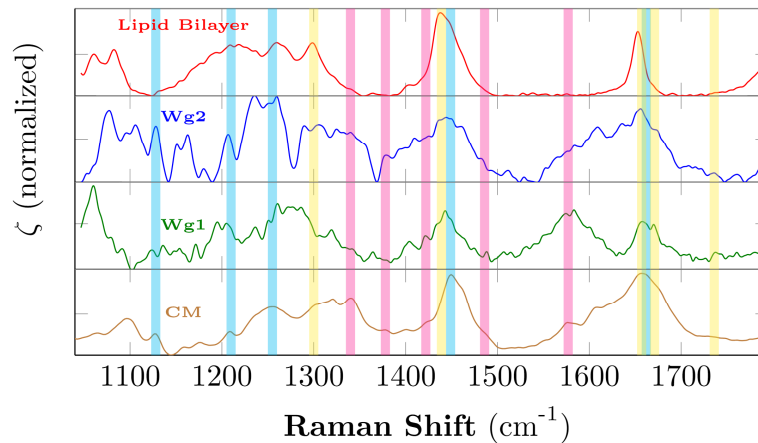


Fig. 5.8] Raman spectra obtained from the confocal area commercial confocal microscope (CM) with $100\mu\text{m}$ diameter fiber as the pinhole of the cells grown on Raman grade CaF slides, NWERS spectra from the cells grown on top of the chips containing the waveguides (Wg1, Wg2) and the spectra from the lipid bilayer formed on top of the waveguide. Light cyan, yellow and pink lines are due to nucleic acids, lipid and proteins respectively [96]. The typical integration times were less than 10 seconds for an effective pump power of $500\mu\text{W}$ in the waveguide. Identical spectrometers were used for all the measurements.

microenvironments. Other reasons could be the presence of specific cell debris on the waveguide, or the location of specific parts of the cell in the slotted region where the evanescent interaction is maximal. A more detailed study is needed to ascertain the origin of the various peaks and to explain the spectral differences. Nevertheless, our study suggests that the on-chip method is suitable to the study of cell membranes in their native state and can bring down the integration times to the order of sub-seconds (with $\text{SNR} > 10$ instead of > 50) leading to a pathway for real-time analysis.

5.8 Closing Remarks

As a proof-of-concept demonstration, here we focused on the biologically relevant problem of detection and quantification of biotin and DNA assays. We emphasize that there are several surface immobilization techniques developed for silica and silicon nitride surfaces [91] [92] which can be readily employed for the analysis of different monolayers using NWERS.

Further when it comes to the cell-membranes, the evanescently excited and collected Raman spectra provide several distinctive features that can be assigned to proteins and nucleic acids. These peaks are not as distinct in the spectra ob-

tained with a confocal microscope. We ascribe these features of the Raman spectra collected using the waveguides to the exclusivity and localization of the evanescent Raman interaction near the membrane-waveguide contact region. Further, the increased interaction area with the optical mode results in an enhanced signal compared to a commercial confocal microscope. The enhanced signal results in a signal acquisition time below 10 s for a $\text{SNR} > 50$. Our preliminary study suggests that the on-chip method using the nanophotonic waveguides is suitable for studying cell membranes in their native state, while also bringing down the integration times to the order of sub-seconds with a reasonable SNR. This leads to a pathway for a real-time analysis of the interactions that happen in the cell-membranes.

Thus, our lab-on-a-chip-based technique offers a simple and apposite alternative to existing techniques which suffer from several problems, such as high expense, photo-damage, the necessity of a vacuum for operation, photo-bleaching, heating and inability to detect non-specific binding, etc.

6

Dependence of the efficiency on channel waveguide parameters

In the previous chapters, the dependence of efficiency of Raman scattering with width of silicon nitride (Si_3N_4) and silicon on insulator (SOI) waveguides was briefly discussed. In addition the theoretical model developed therein were experimentally verified. Having established the relevance of our model, we elaborate the results discussed in the previous chapters to ascertain parameters of relevance and extend the theoretical analysis to TiO_2 and SOI waveguides. Some text has been adapted from the some of my published papers [97], [49].

6.1 Role of index contrast in the enhancement and scattering

To understand the enhancement effects inherent to the waveguides and the role of refractive index contrast, we investigate a common planar/slab waveguide with a silica undercladding, an air uppercladding ($n_1=1$), and variable core index n_c and core thickness d (inset Fig. 6.1). A scattering molecule is located at the air undercladding on top of the core. We investigate two common CMOS compatible core materials, Si ($n_c = 3.45$) and Si_3N_4 ($n_c = 1.89$), for the two orthogonal dipole orientations with respect to the slab waveguide surface. Fig. 6.1 shows the power P coupled to the fundamental TE and TM modes of a slab waveguide from a dipole located at the surface of the waveguide, normalized to the total free-space emission

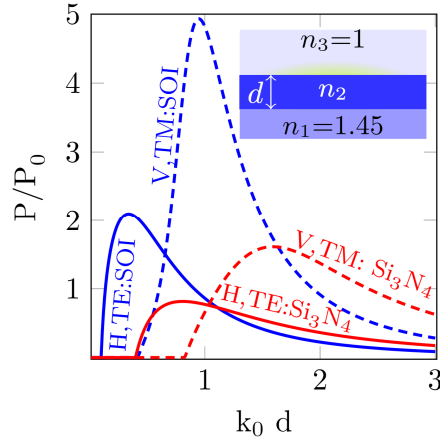


Fig. 6.1 (a) Normalized power P/P_0 coupled to the fundamental TE (solid) and TM (dashed) modes of a slab waveguide as a function of normalized waveguide width $k_0 d$, for Si (blue) and Si_3N_4 (red) cores. The powers are calculated for dipoles on the core surface and oriented vertical (V) and horizontal (H) to it. **Inset:** a generic slab waveguide (adapted from [97], [49])

P_0 of the dipole, calculated using Eq. (3.15). Depending on the orientation of the dipole and polarization of the mode, a strong coupling of the dipole emission (even exceeding P_0) can be observed. The same conclusions hold for the case of excitation from the waveguide modes (for example by comparing Eq. (3.15) and Eq. (3.17)). These results from slab waveguides underscore the critical role of waveguide geometry and index contrast for efficient excitation and collection [46]. We will discuss the implications of this result in more detail in later sections. Interestingly, for both material systems, at the respective wavelengths they are popularly used for their transparency (Si_3N_4 : 785 nm and Si: 1550 nm), the optimal slab thicknesses are near 120 nm and 240 nm, respectively for TE and TM excitation.

6.2 A generic channel waveguide immersed in a medium

In chapter 3 we saw that the efficiency of scattering to a channel waveguide mode depends on the effective area of the modal field (reciprocal of the intensity of the power normalized modal field) at the position of the scattering particle. To evanescently sense a collection of particles, the overlap of the particle-positions with the normalized modal field intensity of the evanescent part of the guided mode is to be determined. On the one hand, higher index contrast and larger core geometry confines light more in the core than in the cladding, thus reduces the effective sensing volume. But, on the other hand, higher confinement leads to increased intensity of the evanescent field for a given input power. Hence, the role of index contrast and

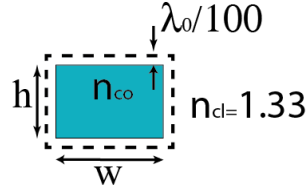


Fig. 6.2 | The channel waveguide geometry investigated in this article. Water cladding surrounds a rectangular Silicon or Silicon Nitride channel waveguide. The molecules are suspended uniformly, either all over the bulk of the cladding (bulk sensing) or adsorbed on the waveguide forming a layer of thickness $\lambda_0/100$ around the waveguide (surface sensing). Aspect ratio a is defined as $a = w/h$.

waveguide geometry on the overall efficiency of a scattering process needs to be clarified. This is the purpose of this section. In order to simplify the problem we assume there is no substrate and the waveguide is surrounded by the analyte from all the sides as shown in Fig. 6.2.

As is the case for common sensing scenarios discussed in the previous chapters, we distinguish two cases, a) bulk-sensing, where the particles are spread across the whole of the cladding volume, and, b) surface-sensing, where the particles are adsorbed on the waveguide such that they lie within a thin layer around the waveguide (Fig. 6.1). For simplicity, first we investigate a channel waveguide surrounded by water cladding. We will numerically evaluate the overall efficiencies as a function of the normalized waveguide area (A) and aspect ratio (a) for Silicon ($n = 3.5$) and Silicon Nitride ($n = 2$) waveguides in water ($n = 1.33$) cladding.

We assume the product of scattering cross-section and the volume density of the molecules to be $\rho\sigma = 1.8 \times 10^{-5} \text{ cm}^{-1} \text{ sr}^{-1}$ (corresponding to the mean Rayleigh scattering cross-section of 1M hydrogen molecules, so that Note that the $1 \cdot 10^8$ corresponds to an absolute conversion efficiency of $5.5 \cdot 10^{-4} \text{ sr/cm}$.) It is emphasized that these representative parameter values we have chosen does not affect the generality of our results because the efficiency of scattering η scales linearly with $\rho\sigma$ as discussed in earlier chapters.

Fig. 6.3 shows the calculated η as a function of the waveguide area A and aspect ratio a for Silicon (Si) and Silicon Nitride (Si_3N_4) waveguides for bulk sensing and surface sensing for a layer of thickness $\lambda_0/100$ around the waveguide. The maximal efficiency, η_{max} is approximately 5.3×10^{-8} for Si waveguides for bulk sensing. The η_{max} for bulk sensing using high index Si waveguides is about 2.4 times larger than that for Si_3N_4 case, while it is about 4.2 times for surface sensing. This implies that surface sensing is more sensitive to index contrast than bulk sensing.

In Fig. 6.3, we observe strong dependence of η on A and a . For all the sensing scenarios, we observe that the optimal η corresponds to a relatively symmetric waveguide ($0.5 < a < 2$) for both of the quasi-TE and quasi-TM modes. This is

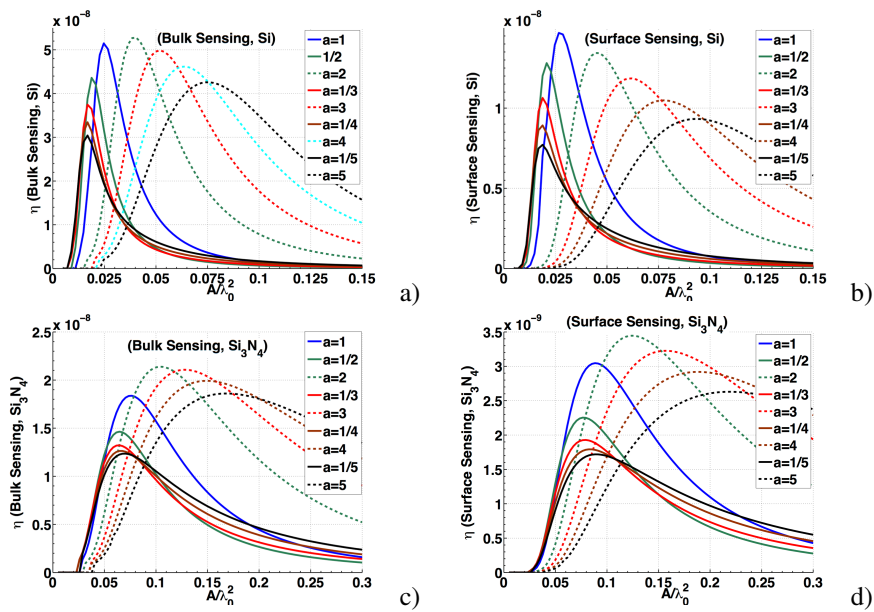


Fig. 6.3] Overall efficiency as function of core area (A), normalized to square of free-space wavelength, for several aspect ratios (a) for the fundamental quasi-TE modes of **a)** Si waveguide for bulk sensing, **b)** Si waveguide for surface sensing, **c)** Si_3N_4 waveguide for bulk sensing and **d)** Si_3N_4 waveguide for surface sensing. Pump is assumed to be of the same polarization. Note that due to symmetry of the problem, the fundamental quasi-TE mode for $a = 1/x$ is the same as the fundamental quasi-TM mode for $a = x$, and for $a = 1$ quasi-TE and quasi-TM modes are degenerate. Note that the $1 \cdot 10^8$ corresponds to an absolute conversion efficiency of $5.5 \cdot 10^{-4}$ sr/cm.

rather surprising knowing that, for a given area, a nonsymmetrical waveguide has a larger sensing surface. This means that the effective sensing area is determined predominantly by the modal field properties rather than by the actual sensing area. We also see that the optimal η is less dependent on a for bulk sensing compared to surface sensing. For example, the optimal η for Si (Si_3N_4) waveguides changes by 36% (25%) as we go from $a = 1$ to $a = 5$, while for bulk sensing, the change is only about 19% (13%). Further, the A corresponding to optimal η , for a given a , is higher for surface sensing than for bulk sensing. For instance, for $a = 2$, the optimal A for surface sensing is $0.004 \lambda_0^2$ higher than for bulk sensing with Si waveguide while it is $0.048 \lambda_0^2$ higher for Si_3N_4 waveguides. This observation means that a higher optical confinement in the core leads to higher intensity at the waveguide surface and is favored for optimal surface sensing compared to bulk sensing.

6.3 Integrated channel waveguides on a substrate

In order to simplify the problem assumed a substrate-less waveguide in the previous chapter. In this section we compare three popular waveguide platforms silicon-on-insulator (SOI) waveguide platform [98] and an emerging waveguide platform based on Titanium oxide (TiO_2). To be in line with the experimental parameters used for the experiments with the Si_3N_4 waveguides, we perform simulations with an excitation wavelength $\lambda_0 = 785$ nm. The refractive indices of the core, SiO_2 undercladding and IPA upper cladding are respectively taken to be $n_{\text{sin}} = 1.89$, $n_{\text{ox}} = 1.45$ and $n_{\text{ipa}} = 1.37$. In case of SOI waveguides, $\lambda_0 = 1550$ nm was chosen because of a low optical absorption. The refractive index of silicon is taken to be $n_{\text{si}} = 3.44$. As for TiO_2 waveguides, the refractive index $n_{\text{TiO}_2} = 2.4$ reported in [99] is used. For the TiO_2 case we study η_0 at $\lambda_0 = 785$ nm and also at $\lambda_0 = 1064$ nm. The latter choice of λ_0 corresponds to a material wavelength comparable to that of SOI (at $\lambda_0 = 1550$ nm) and Si_3N_4 (at $\lambda_0 = 785$ nm). The aforementioned choice of the comparable material wavelengths ensures similar fabrication constraints and practical waveguide dimensions for single mode operation. The height of the waveguides is fixed at $h = 220$ nm for all waveguide types, which is a typical deposition thickness during the fabrication of Si_3N_4 and TiO_2 waveguides, and also a typical silicon thickness for SOI waveguides. The conversion efficiency η_0 was calculated using Eq. (4.1) with COMSOL finite elements mode solver.

In Fig. 6.4 we show theoretical conversion efficiency η_0 for randomly distributed particles lying uniformly in the upper cladding of Si_3N_4 , TiO_2 and SOI strip waveguides of several waveguide widths w corresponding to the single mode operation of the waveguides. As the waveguide width is increased, initially η_0 increases to a maximum corresponding to an optimal mode confinement in the core and the cladding. Once this condition is reached, further increase in the width

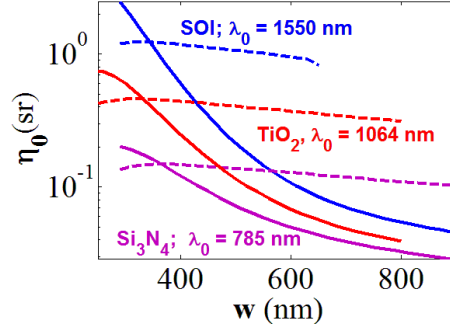


Fig. 6.4 | Theoretical conversion efficiency curves for strip waveguides as a function of total waveguide width w for different material systems and the corresponding excitation wavelengths. Blue, red and magenta colors are respectively for SOI, TiO_2 and Si_3N_4 cores. Solid lines: TE polarized excitation and collection. Dashed lines: TM polarized excitation and collection. Only the curve segments corresponding to single mode operation from the cut-off width are shown. Note that y-axis in log scale.

leads to a decrease in η_0 owing to more confinement of the modal field in the core. We observe this irrespective of the waveguide type, polarization or core material. This is because the increase in the waveguide width increases the confinement of the mode in the core thereby reducing the interacting field in the upper cladding region of the analytes. For strip waveguides, TM polarization generally performs better than TE polarized modes and its sensitivity to the waveguide width is smaller. The discontinuity of the electric field at the core - top cladding interface of the TM modes leads to higher field at the analyte location. The increased field and larger interaction volume present on the top cladding for TM modes (owing to high width-height aspect ratio) results in higher η_0 . Since the electric field in the TM mode is discontinuous in the perpendicular direction, only substantial changes in waveguide height h vary the TM field significantly. For a typical 600 nm wide strip waveguide, TM excitation in comparison to the TE excitation, leads to more than 2.5, 4 and 5 times more efficiency respectively for Si_3N_4 (at $\lambda_0 = 785$ nm), TiO_2 ($\lambda_0 = 1064$ nm), and Si ($\lambda_0 = 1550$ nm) waveguides.

In Fig. 6.5, η_0 for slotted waveguides with various slot widths $s = 10$ nm, 50 nm, and 150 nm, and waveguide widths w (inclusive of the slot) is shown for Si_3N_4 , TiO_2 and SOI waveguides. In case of TE polarized modes, slotted waveguides generally perform much better than strip waveguides and the value of η_0 increases as s decreases. This can be attributed to the enhancement of the TE-field in the slot region as s is decreased. However, there is an optimum s whence η_0 starts to decrease. This originates from a reduction in the interaction volume within the slot region as s is decreased. The optimum s is near 50 nm, 30 nm and 10 nm for respectively Si_3N_4 (operating at $\lambda_0 = 785$ nm), TiO_2 waveguides ($\lambda_0 = 1064$ nm) and SOI waveguides ($\lambda_0 = 1550$ nm). As expected, due to the

continuity of the electric field, the field enhancement in the slot is much less in case of TM polarization (Fig. 6.6); hence, the effect of s is not significant in case of TM polarization.

In Fig. 6.6 we compare the conversion efficiency η_0 of TiO_2 waveguides for $\lambda_0 = 785$ nm and $\lambda_0 = 1064$ nm. η_0 is generally higher for $\lambda_0 = 1064$ nm because the field is confined more to the cladding where analyte is located. Due to a shorter material wavelength, the modal field is more confined to the high index TiO_2 region when excited at 785 nm, compared to excitation at 1064 nm. Consequently, the optimal slot width for TiO_2 ($\lambda_0 = 785$ nm) is narrower: about 10 nm compared to about 30 nm $\lambda_0 = 1064$ nm. For $\lambda_0 = 785$ nm η_0 also increases weakly for wider slots (such as $150 \text{ nm} > s > 100 \text{ nm}$). This can be understood with the help of Fig. 6.6.

In Fig. 6.7, we show the conversion efficiency η_0 of slot waveguides with $s = 100$ nm, as a function of the total waveguide width w for different material systems. We observe a strong enhancement in η_0 with the increase in the index contrast of the waveguide. Higher index contrast leads to a lower mode area, higher modal field intensity and higher field discontinuity, thus giving rise to a stronger evanescent field for interaction. From the simulation data presented in Fig. 6.5 and Fig. 6.7, we can conclude that a slot of width $s = 100$ nm leads to about 90, 20 and 7 fold higher efficiency respectively for SOI (excited at $\lambda_0 = 1550$ nm), TiO_2 ($\lambda_0 = 1064$ nm), Si_3N_4 ($\lambda_0 = 785$ nm) slot waveguides of $w = 600$ nm compared to the strip waveguide of the same dimension.

6.4 Closing Remarks

In this chapter we explored the effect of geometry and index contrast for the efficiency of the waveguides. We also explored the possibility to use SOI and TiO_2 platforms as an alternative integrated waveguide platform to use as Raman spectroscopy.

When comparing different waveguide systems operating at different excitation wavelengths, however, the corresponding change in the scattering cross-section also has to be taken into account. As the scattering cross-section varies approximately as λ_0^{-4} (Chapter 2), the total collected power also varies in a similar manner. We can include this correction factor and compare the respective net efficiencies for slot waveguides ($w = 600$ nm and $s = 100$ nm), Si_3N_4 waveguides ($\lambda_0 = 785$ nm), TiO_2 waveguides ($\lambda_0 = 1064$ nm) and the SOI waveguides ($\lambda_0 = 1550$ nm). After the λ_0^{-4} correction at these respective operating wavelengths, SOI is about twice as efficient, and TiO_2 is about 30% more efficient than Si_3N_4 waveguides owing to their higher index contrast.

Note that in Fig. 6.4 and Fig. 6.6, $\eta_0 > 4\pi$ sr, for SOI waveguides in a certain range of waveguide dimensions. This is a result of high importance. To appreci-

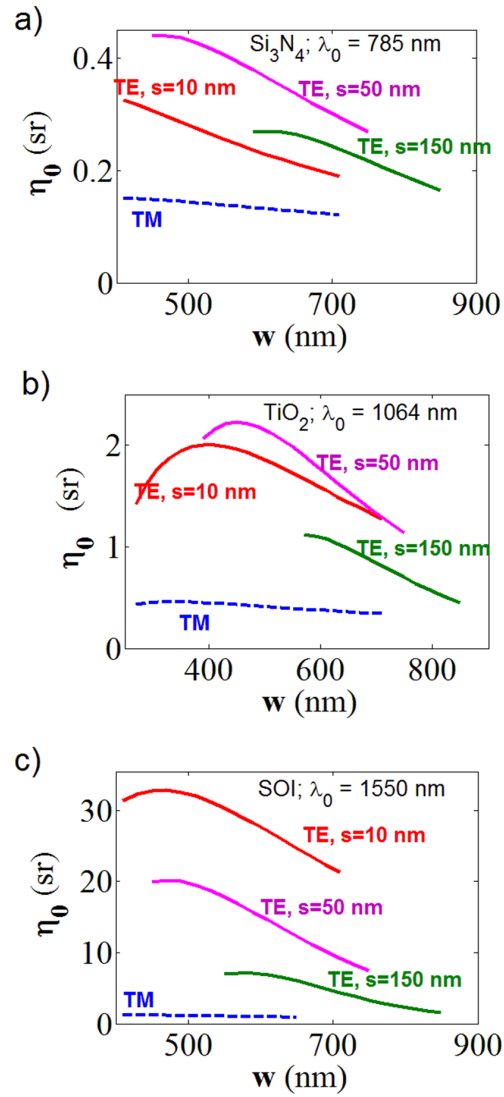


Fig. 6.5 | Theoretical conversion efficiency curves for slot waveguides for a) Si_3N_4 core with $\lambda_0 = 785$ nm, b) TiO_2 core with $\lambda_0 = 1064$ nm c) silicon core with $\lambda_0 = 1550$ nm. The solid lines: TE polarized excitation and collection. Dashed lines: TM polarized excitation and collection. Green, magenta and red lines are respectively for slot width of 150 nm, 50 nm and 10 nm. Only the curve segments corresponding to single mode operation from the cut-off width are shown.

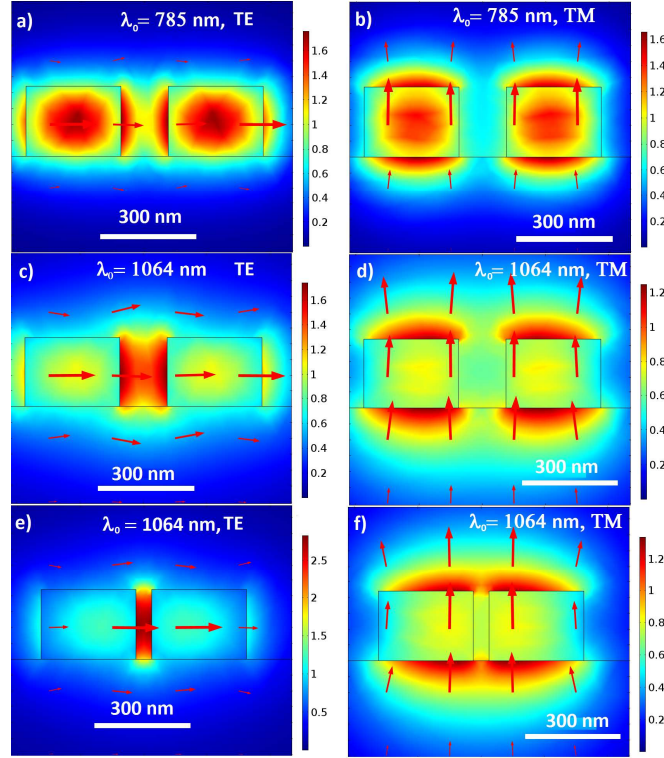


Fig. 6.6 | Plot of the modal field of the TiO₂ slot waveguides for **a**) TE polarization for $s = 150$ nm, $w = 750$ nm, $\lambda_0 = 785$ nm, **b**) TM polarization for $s = 150$ nm, $w = 750$ nm, $\lambda_0 = 785$ nm, **c**) TE polarization, $s = 150$ nm, $w = 750$ nm, $\lambda_0 = 1064$ nm **d**) TM polarization for $s = 150$ nm, $w = 750$ nm, $\lambda_0 = 1064$ nm **e**) TE polarization for $s = 50$ nm, $w = 650$ nm, $\lambda_0 = 1064$ nm **f**) TM polarization for $s = 50$ nm, $w = 650$ nm, $\lambda_0 = 1064$ nm. The arrow shows the electric field vector at a given location.

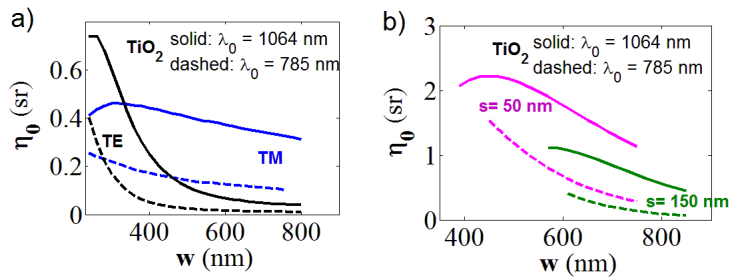


Fig. 6.7 | Theoretical conversion efficiency curves for TiO₂ **a**) strip **b**) slot waveguides with $\lambda_0 = 785$ nm (dashed lines) and $\lambda_0 = 1064$ nm (solid lines). Black and blue curves: strip waveguides. Green: slot waveguides, $s = 150$ nm. Magenta: slot waveguide, $s = 50$ nm. The values of η_0 for TM polarization for all the slot widths (data not shown) do not differ significantly from the values for strip waveguides. Only the curve segments corresponding to single mode operation from the cut-off width are shown.

ate this, we apply Eq. (4.1) for free space beams with $\eta_0 = 4\pi$ and integrate dz arbitrarily. This is possible in an ideal situation when we can collect the scattered light perfectly from total solid angle of 4π sr, and if particles are excited with a diffraction-less beam so that dz in Eq. (4.1) can be integrated arbitrarily. Thus, we conclude that due to enhanced excitation and emission (Purcell enhancement, Chapter 3) near the high index contrast waveguides, the overall efficiency of excitation and collection of a practical single mode waveguide can be higher than the ideal free space excitation and collection. For a realistic diffraction-limited free-space microscope system, however, the collection and excitation depth of focus are limited due an inverse relationship between the collection angle and the depth of focus. Hence, NWERS approach in general, performs much better than realistic free space optical systems.

If the upper cladding refractive index varies, the confinement properties of the waveguide mode also changes. Consequently, the conversion efficiency will vary via Eq. (4.1). Nevertheless, the qualitative conclusions discussed in this chapter are applicable for analytes with refractive index in the range 1.3-1.44. For analytes with refractive indices significantly different from IPA ($n = 1.37$), η_0 can be calculated using Eq. (4.1).

7

The Background from the waveguides and Signal-to-noise Ratio considerations

In chapters 3 and 4 we briefly discussed how the limit-of-detection or SNR of the integrated waveguide systems is limited by the waveguide background luminescence (WGBL) originating from the waveguide material. In appendix B we calculate how SNR of the system is dependent on the intensity of this WGBL. In this chapter we will experimentally investigate the properties of the WGBL, measure its strength and suggest an empirical formula for its general characteristics in order to aid understanding its origin. Based on the experimental results, we will also develop a subtraction method to recover weak signal from the WGBL.

7.1 The origin of the waveguide WGBL

In this section we investigate the dependence of the WGBL with waveguide materials, pump-frequency, deposition method, pump power, and temperature in order to identify and ascertain its origin.

7.1.1 Raman features in the WGBL

Fig. 7.1 shows the WGBL from an air-cladded, 0.7 cm long, 700 nm wide strip waveguide measured using the excitation and collection from the fundamental TE

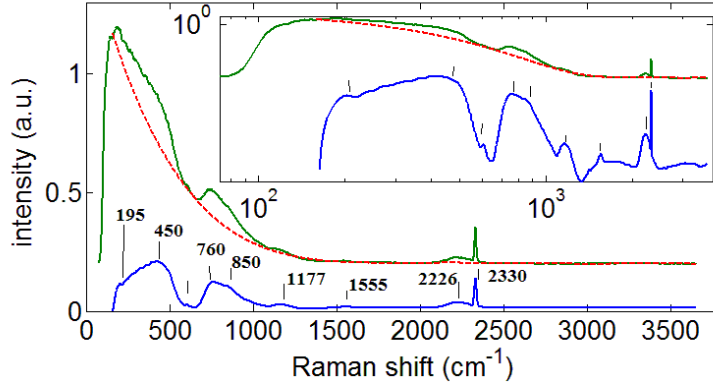


Fig. 7.1 Complete WGBL from a 0.7 cm long, 700 nm wide air-cladded strip waveguide measured (green solid line) using excitation and collection from the fundamental TE mode, the 5th order polynomial fit to the WGBL (red dashed line) and the polynomial subtracted Raman component in the WGBL (blue lower line). In the inset, we also show the same spectra in log-log scale so that several small peaks are visible.

mode. The WGBL contains several narrow-band and broadband peaks. In order to separate these features with the slowly varying component (defined by the red dashed line) and identify the origin of the peaks, we implement a 5th order polynomial fit to the WGBL and subtract the polynomial. The subtraction yields a spectrum very similar to the infrared absorption spectrum measured for silicon-nitride thin-films [100–102]. The major peaks centered at 450 cm⁻¹, 850 cm⁻¹, 1175 cm⁻¹ and 2226 cm⁻¹ are assigned respectively to Si breathing, Si-N stretch, N-H bending, N-H₂ bending and Si-H stretch [100]– [102]. The strong narrowband peak at 2330 cm⁻¹ may be due to interstitial N₂ formed in the core material during the deposition process [103]. Thus, we conclude that the WGBL mainly contains Raman peaks originating from the waveguide core material, and depends on [100] – [103] the waveguide core deposition process and its chemical composition.

7.1.2 Dependence with materials

Several peaks corresponding to Si₃N₄ deposition chemistry suggested that the most of the Raman features in the WGBL originates from the core. However, the WGBL may also have contribution from SiO₂ which forms the lower cladding. In order to identify the dominating source of the WGBL, we performed a confocal Raman z-scan of a stack of material that were used to fabricate the waveguide. The stack contained a 220 nm PECVD Si₃N₄ top layer on 2.4 μm silicon dioxide, which was deposited on a silicon-substrate using the same deposition chemistry. The spectra were measured using a commercial confocal Raman microscope (WITec) with a 532 nm laser, focused through a 0.9 NA air objective with a 20

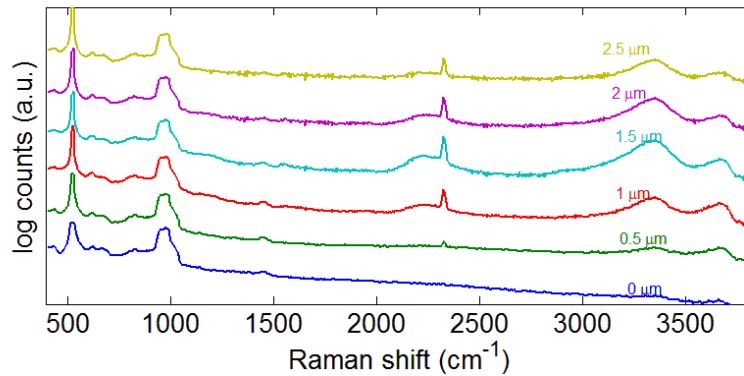


Fig. 7.2 A confocal Raman z-scan of a 220 nm PECVD Si_3N_4 top layer on $2.4 \mu\text{m}$ silicon dioxide, deposited on a silicon-substrate confirms the major contribution to the WGBL originates from Si_3N_4 . The peaks at 520 cm^{-1} and 960 cm^{-1} are ascribed to the peaks from Si. The spectra presented are offset for clarity. Adapted from [104].

mW pump power on sample and a 60 second integration time. Fig. 7.2 displays the Raman spectra of the z-scan. For the z corresponding to the silicon substrate, we see the well-known silicon Raman peaks at 520 cm^{-1} and 960 cm^{-1} . When moving up in the material stack, we can identify Raman contributions specific to Si_3N_4 discussed before. Further, a similar z-scan measurement was performed in a silicon dioxide–silicon material stack. The z-scan measurement of this stack showed no such Raman peaks thus confirming that the peaks indeed originate from the Si_3N_4 core region.

Furthermore, we fabricated waveguides using Si_3N_4 rich material deposited using different deposition methods and compared the spectra of the corresponding WGBL. The relative WGBL strength varied strongly with the type of Si_3N_4 deposited (Fig. 7.3). Hence, we conclude that the major contribution of the WGBL originates from the core material. In the hindsight, it is not surprising since the confinement factor of the light in the core is generally $> 50 \%$.

7.1.3 Dependence on pump frequency

Having established the origin of the narrow peaks in the WGBL, we now investigate the nature of the broad and slowly-varying feature of the WGBL that was approximated by the fifth order polynomial function in the last section (Fig 7.1). Generally such a polynomial background emission in a Raman measurement is associated with auto-fluorescence arising from the electronic transitions of the material itself. A common strategy to discern the auto-fluorescence is to excite the material with wavenumbers that differ by some significant amount ($> 500 \text{ cm}^{-1}$) and

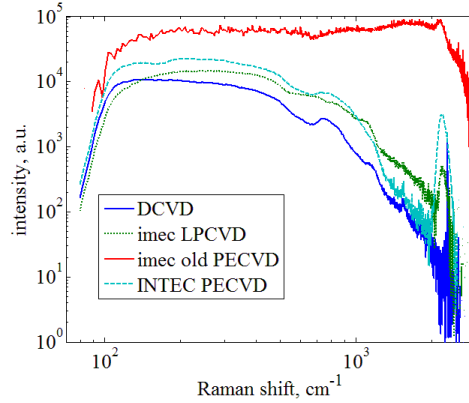


Fig. 7.3 The WGBL originating from waveguides fabricated on various Si_3N_4 rich thin-films (SNRF) deposited using different deposition chemistries. **DCVD** is the PECVD deposited SNRF used for fabrication of the waveguides used in our experiments discussed in Chapters 4 and 5. **INTEC PECVD** and **imec old PECVD** are respectively SNRF deposited with a recipe developed at University of Ghent clean room at Zwijnaarde and at imec in Leuven before optimized DECVD was developed.

measure the emission spectra. A substantial change in the intensity of the background typically means that the WGBL is due to auto-fluorescence, as the intensity of the fluorescence depends on the pump frequency and the spectral features in the fluorescence signal in wavenumbers does not shift with the pump wavenumbers. Raman signal however shifts by the same wavenumbers as the shifts in the pump wavenumbers. The mitigation strategy for the fluorescence is then to pump at the wavelength that minimizes the fluorescence or to use a subtraction algorithm that removes all the common mode fluorescence signal.

In Fig 7.4, we show the WGBL generated by fundamental TE mode of a 700 nm wide strip waveguide when excited at 785 nm and 830 nm wavelengths, which corresponds to about 800 cm^{-1} difference in wavenumbers. We observe a negligible difference, which we attribute to the difference in the quantum-efficiency of the detectors for the two spectra in absolute wavenumbers. In Fig 7.4, we also plot the spectrum obtained from the z-scan measurement data shown in Fig 7.2 measured using the excitation at 532 nm. This spectrum is collected at $z = 1.5 \mu\text{m}$ and corresponds to the strongest signal originating from the silicon-nitride in the stack and is normalized to the same scale. Apart from the peaks at 520 and 960 cm^{-1} ascribed to Si there is no significant difference in the WGBL spectrum. Thus, based on these measurements, we conclude that the WGBL spectra does not differ significantly within the wavelengths 532 nm - 830 nm pump wavelengths. This conclusion excludes the possibility that the major contribution of the WGBL originates from the auto-fluorescence of the core material.

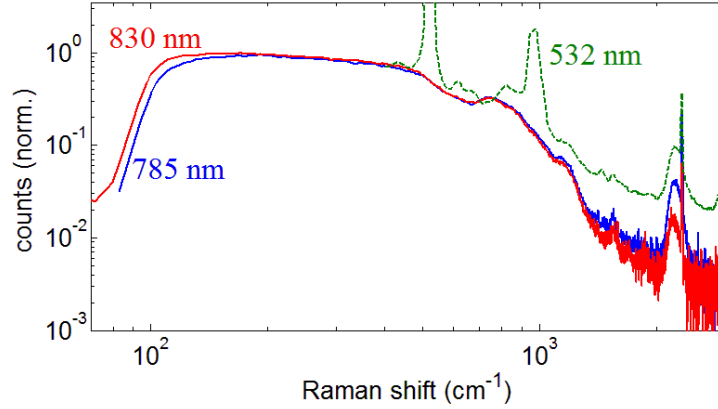


Fig. 7.4| WGBL spectra measured at three different pump wavelengths. The green-dashed spectra at 532 nm is from Fig 7.2 for $z = 1.5 \mu\text{m}$ normalized to same scale. A significant difference in the WGBL is not observed.

7.1.4 Dependence with pump power

In order to ascertain if the origin of the WGBL is a nonlinear process, such as the self-phase modulation, we varied the pump power from 60 mW to 380 mW, with about 8 dB in-coupling losses. Figure 7.5 displays the WGBL spectra obtained from a strip waveguide of $w = 700 \text{ nm}$ and $h = 220 \text{ nm}$ for different input pump powers. To quantify the variation of the total spectra for different input powers, we implemented a least-square algorithm that finds a normalization scalar ϕ that rescales the entire spectrum S_i to S_{60} , the spectrum with 60 mW, such that, $\sum_{\nu} (S_i(\nu) - \phi S_{60})^2$ is minimized. The rescaling using a scalar ensures that only difference in the spectral shape is quantified using the calculated residue, removing any common-mode amplitude variations that may arise from the differences in coupling losses. The normalized spectra is plotted in Fig 7.5. The corresponding mean-squared errors (residue) are less than 1 % for the whole range of spectrum and powers investigated. We conclude that the shape of the WGBL does not depend on the investigated input powers. We attribute the small amount of observed residue to the shot noise and the fluctuations that depend on the input power and the dark noise of the detector. If the WGBL originated from a non-linear process, the shape of the spectra should have noticeably been influenced by the input power during the 6 fold increase in the waveguide power. The spectrum produced by a non-linear processes, such as the self-phase modulation, are characterized by a significant changes in the spectrum shape with the input power.

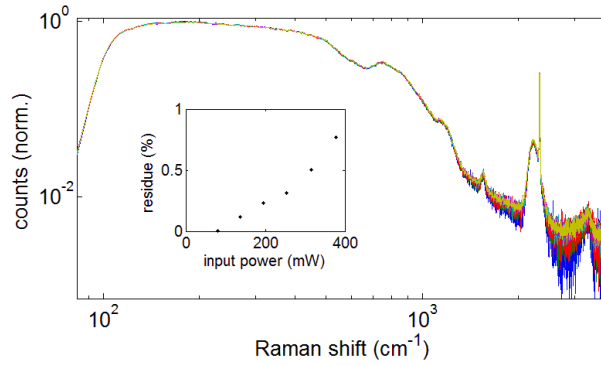


Fig. 7.5| The WGBL spectra obtained from a strip waveguide of $w = 700$ nm and $h = 220$ nm waveguide for different input pump powers. The spectra are normalized by a factor obtained using the least-squared-error algorithm. The corresponding mean-squared errors (residue) are less than 1%. The spectral residue is plotted in the inset.

7.1.5 Origin of the broad feature in the background

Based on the experiments discussed earlier, the theoretical treatments in the literature on the Raman spectrum of amorphous materials [105, 106, 119, 122] the origin and the shape of the broad feature of the WGBL without the Raman peaks identified earlier (described by dashed line in Fig. 7.1), is possibly related to breaking of momentum selection rules due to amorphous nature of the waveguide material. For amorphous materials characterized by a short correlation length l_c of the dielectric function (compared to the wavelength of the pump $l_c < \lambda/10$), Suker et. al. [105] derived a frequency dependent amplitude in terms of the density of states ($g(\omega_s)$), Bose-Einstein distribution function and a frequency dependent photon-phonon coupling coefficient ($C(\omega_s)$). However, their equation may not directly applicable in the case of waveguides, because of the ambiguity in the frequency dependence of the photon-phonon coupling coefficients [106], and the lack of understanding on how the optical and thermal confinement properties of the waveguides affect $C(\omega_s)$. It was shown that $C(\omega_s)$ may have a complicated spectral dependence [122]. Needless to say, more theoretical and experimental investigation is needed to understand and ascertain the behavior and the origin of the WGBL.

7.2 Determination of the WGBL efficiency

We have seen that the WGBL depends on the material of the waveguide core. The ratio $R_{S/B}$ between the signal counts from analyte C_S and the counts due to the WGBL C_{BG} , neglecting the dark counts of the detector, can then be written as:

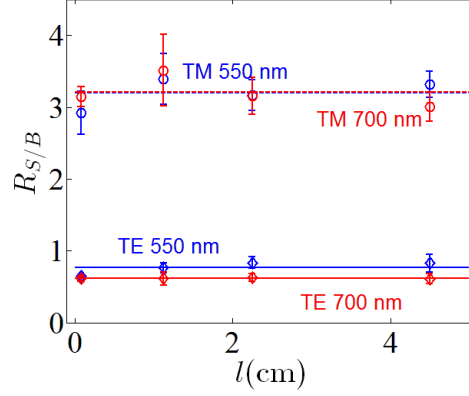


Fig. 7.8 | The ratio of signal to the WGBL counts ($R_{S/B}$) as a function of length for 819 cm^{-1} IPA line. $R_{S/B}$ remains practically a constant. The values are extracted from at least three chips measured three times from the experimental data already discussed in §. 4.6.

$$\begin{aligned}
 R_{S/B}(\nu) &= \frac{C_S(\nu)}{C_{BG}(\nu)} \\
 &= \frac{\eta_s}{\eta_{BG}} \frac{\rho_S \sigma_S}{\beta_{BG}} \\
 &= \chi(\nu) \sigma_S \rho_S
 \end{aligned} \tag{7.1}$$

where, $\frac{\eta_s}{\eta_{BG}} \equiv \eta_{S/B}$ is the ratio of analyte signal conversion efficiency to the WGBL conversion efficiency given by the ratio of the integral of the integrated-luminosity of the waveguides respectively in the core region and the analyte region:

$$\eta_{S/B} = \frac{\eta_s}{\eta_{BG}} = \frac{\iint_{clad} \Lambda_{1D}(\vec{r}) d\vec{r}}{\iint_{core} \Lambda_{1D}(\vec{r}) d\vec{r}} \tag{7.2}$$

and χ is the signal-to-background (S-B) conversion factor, defined as

$$\chi = \frac{\eta_{S/B}}{\beta_{BG}} \tag{7.3}$$

Eq. (7.1) can be used to plot $R_{S/B}$ as a function of concentration of analyte in an experiment, from which the signal to WGBL conversion factor $\chi(\nu)$ can be determined. Once $\chi(\nu)$ is determined, one can measure the concentration or cross-section of the analyte present in the cladding in an absolute manner, without having to measure the transmitted pump power that is needed if we use Eq. (4.4).

However, here we take a slightly different route to calculate the WGBL efficiency β_{BG} , in order to avoid ambiguity due to variations in the concentration during the measurement. This also serves to verify several implicit assumptions, such as linear dependence of WGBL with the lengths, that were made to arrive at Eq. (7.1). In Fig 7.8, we show $R_{S/B}$ for pure IPA (819 cm^{-1} line) for different

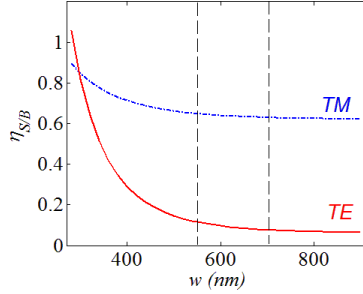


Fig. 7.9 | Calculated ratio of the signal to the WGBL conversion efficiencies $\eta_{S/B}$ as a function of waveguide width for Si_3N_4 waveguides with $h = 220$. Dashed lines are points corresponding to the widths investigated experimentally in Fig. 7.3 and Fig.7.5.

waveguide lengths for different waveguide geometries for both TE and TM polarizations. Since both analyte signal and WGBL counts depend in a similar (presumably, linear) way to the waveguide length, and both signals undergo similar attenuation and coupling losses, their ratio is independent of various experimental factors. Fig. 7.8 essentially confirms the independence of $R_{S/B}$ with respect to variation of length for strip waveguides of width 500 nm and 700 nm and for both TE and TM polarizations. In doing so, the figure also reaffirms a linear dependence of the waveguide -WGBL to the length of the waveguide, as the linear dependence of the signal is already established in Chapter 4.

Eq. (7.2) is helpful to calculate $\eta_{S/B}$ for any given waveguide using standard mode solvers. Fig. 7.9 displays the plot of $\eta_{S/B}$ for Si_3N_4 strip waveguides of various widths w and fixed $h = 220$ nm for the fundamental TE and TM modes. We observe that $\eta_{S/B}$ is enhanced by a factor of 8.8 for TM polarization compared to TE polarization due to the lower mode confinement of TM modes to the waveguide material, the result which we have observed also in Fig. 7.8 with the same factor with a proportionality constant related to Raman efficiency β_{BG} of the background.

In fact, the data presented in Fig. 7.8 (the average of $R_{S/B}$) and data presented in Fig. 7.9 (the calculated $\eta_{S/B}$) can be used to estimate β_{BG} via Eq. (7.1) - Eq.(7.3). Fig. 7.10 show the plot of the signal-to-background ratio $R_{S/B} = C_S/C_B$ vs the corresponding $\eta_{S/B}$ for the two polarization modes and waveguide widths investigated. Since, the product of the concentration of pure IPA and the cross section of its 819 cm^{-1} line is known ($\sigma\rho = 6.22 \cdot 10^{-9} \text{ sr}^{-1}\text{cm}^{-1}$), the Raman scattering efficiency of the WGBL β_{BG} can be calculated to be $1.2 \pm 0.1 \cdot 10^{-9} \text{ sr}^{-1}\text{cm}^{-1}$. This value is about six times smaller than the value for pure IPA. Once β_{BG} is determined at one frequency it is straight forward to extrapolate in the entire Stokes region of interest by using a measured spectrum of the WGBL as shown

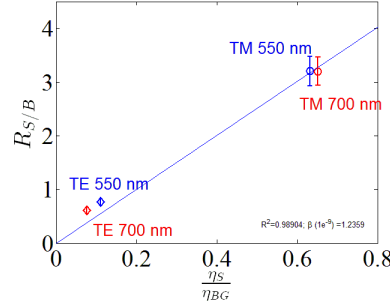


Fig. 7.10 Average ratio of signal to the WGBL counts ($R_{A/B}$) plotted against the calculated $\eta_{S/B}$. The R^2 of the fit is 0.989 and yields $\beta_{BG} = 1.2 \pm 0.1 \cdot 10^{-9} \text{sr}^{-1} \text{cm}^{-1}$ at the 819 cm^{-1} Raman line of IPA.

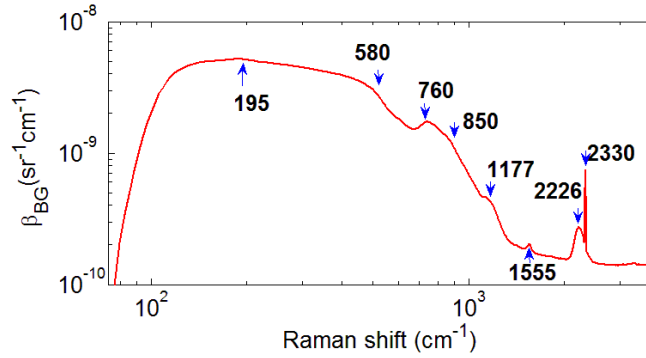


Fig. 7.11 The WGBL efficiency spectrum for the entire Stokes region based on the value determined at the 819 cm^{-1} .

in Fig 7.11. For an arbitrary analyte this value of WGBL β_{BG} completely determines the signal-to-background ratio in a measurement, once the corresponding cross-section, along with the relevant specific conversion efficiencies η_s and η_{BG} are known.

7.3 Modeling and subtraction of the WGBL

In chapters 3 and 4, we saw that the SNR performance of the NWERS system is superior compared to an idealized free-space system, despite the presence of the WGBL. Nevertheless, any existing WGBL needs to be subtracted, particularly in the case of low concentration when the signal from the analyte is weak. As we discussed in this chapter the WGBL is experimentally stable, can be well-characterized and modeled allowing a minimized subtraction error. In this section

we describe a simple model of the WGBL and a simple WGBL subtraction algorithm.

We model the measured NWERS signal S_{MES} as:

$$S_{MES}(\lambda) = R_{ANL}(\lambda) + P_{SIN+ANL}(\lambda) + R_{SIN}(\lambda) \quad (7.4)$$

Here R_{ANL} is the Raman signal exclusively from the analyte, $P_{SIN+ANL}$ is the polynomial WGBL from the Si_3N_4 core discussed in §7.1, possibly with some polynomial contribution from the analyte too, R_{SIN} is the Raman signal from the Si_3N_4 core discussed in §7.1. A reference spectrum from the waveguide, measured without the analyte is:

$$S_{REF}(\lambda) = P_{SIN}(\lambda) + \alpha R_{SIN}(\lambda) \quad (7.5)$$

The polynomial background P_{SIN} and $P_{SIN+ANL}$ can be approximated by using the asymmetric cost function algorithm [51] that finds the polynomial that minimize the cost defined as the mean squared difference between the spectrum and the polynomial. After subtraction of the WGBL polynomial this becomes:

$$\tilde{S}_{MES} = S_{MES} - P_{SIN+ANL} = R_{ANL} + R_{SIN} + e_1 \quad (7.6)$$

and,

$$\tilde{S}_{REF} = S_{REF} - P_{SIN} = \alpha R_{SIN} + e_2 \quad (7.7)$$

where e_1 and e_2 are small residual errors that might have remained during the subtraction process. The Raman signal contribution from the core R_{SIN} in Eq. (7.4) can now be obtained from the \tilde{S}_{REF} by calculating the linear scaling factor α using least square algorithm that minimizes the cost defined as follows:

$$C = \left(\tilde{S}_{MES}(\lambda) - \frac{\tilde{S}_{REF}(\lambda)}{\alpha} \right)^2 \quad (7.8)$$

An approximate Raman spectrum of the analyte on top of the waveguide is then given by:

$$R_{ANL} = \tilde{S}_{MES} - \frac{\tilde{S}_{REF}}{\alpha} + e \quad (7.9)$$

The approximate spectrum may contain some residual WGBL e that has not been completely removed during the process. The residual WGBL e is then removed using a variant of the low order asymmetric Whittaker method developed by Eilers [107].

Fig. 7.13 illustrates the WGBL subtraction algorithm discussed previously. First the reference spectrum S_{REF} of the waveguides without the analyte is measured as shown in Fig. 7.13(a). The third order polynomial part of the WGBL,

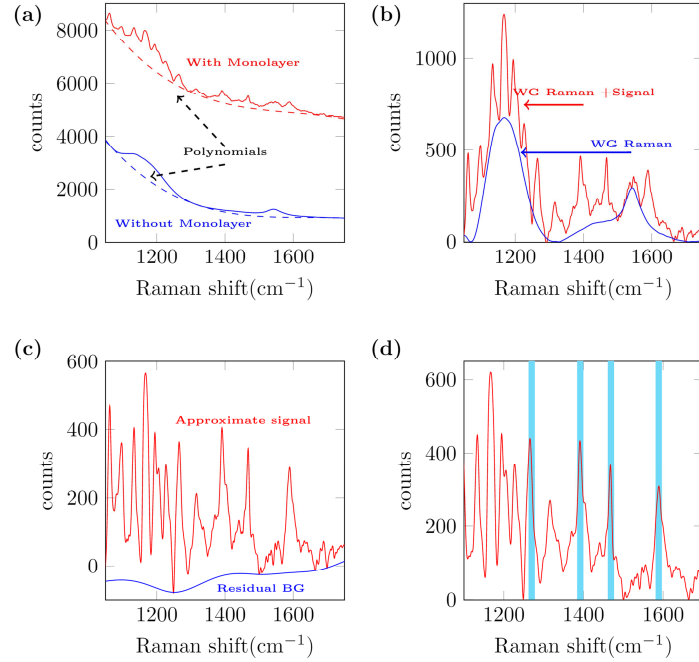


Fig. 7.13 | Illustration of the WGBL subtraction algorithm as applied to a monolayer of DNA-cDNA-Cy3 hybridization in chapter 5. (a) Raw spectrum of the waveguides with and without monolayers and the corresponding third order polynomial approximations of the polynomial component of the WGBL. (b) The difference of the spectra and corresponding polynomials shown in (a). The difference spectrum obtained from the waveguide without analyte is rescaled to that with analyte. (c) The difference between the rescaled WGBL without and with the analyte, giving an approximate Raman spectrum of the analyte alone. Any residual WGBL is subtracted to obtain the final spectrum of the analyte shown in (d). (d) The final Raman spectrum indicating the major Raman lines corresponding to Cy3.

obtained using the asymmetric cost function algorithm is then subtracted yielding an approximate WGBL \tilde{S}_{REF} (Fig. 7.13(b)). The polynomial-subtracted WGBL consists mainly of a homogeneously broadened Raman spectrum R_{SIN} of the deposited Si_3N_4 . This Raman spectrum of the waveguide is then re-scaled, as necessary, to the similar spectra \tilde{S}_{MES} obtained with analyte and subtracted yielding an approximate signal spectrum of the analyte R_{ANL} . The residual e that may have cropped in during the process is removed to get the final spectra as shown in Fig. 7.13 (d).

7.4 Closing Remarks

In this chapter we experimentally investigated the origin of the WGBL. Based on the experimental results discussed, we can conclude the following:

1. Various peaks observed in the WGBL can be assigned to different vibrations due to the molecules and impurities confined in the core during the deposition process. The waveguide core forms the dominating source of the WGBL.
2. The broad background feature of the spectrum can be modeled as a 5th order polynomial. However, our preliminary studies show that this feature is most probably related to the Raman scattering of amorphous materials and can be studied with Bose-Einstein statistics or its high temperature approximation, namely, Maxwell-Boltzmann statistics. A thorough theoretical analysis of phonon-photon coupling factor and a temperature dependent measurement of the spectra is needed to understand and ascertain the origin of WGBL, and to subsequently develop strategies to reduce the WGBL.
3. The maxima of the Raman efficiency of the WGBL is about $5 \cdot 10^{-9} \text{ sr}^{-1} \text{ cm}^{-1}$ which is about 3 times smaller than Raman efficiency of 819 cm^{-1} line of the pure isopropyl alcohol.
4. The use of special designs such as slotted waveguide and the use of TM polarization leads to smaller background relative to the signal.
5. The background can be modeled and subtracted using a very simple background subtraction method.

8

Perspectives on integration with plasmonic structures, resonators and spectrometers, and General conclusions

The potential of waveguiding to enhance Raman signal was recognized [19] as early as 1980 and used in various forms, such as hollow core fiber [21] for gases, liquid core waveguides [22] for transparent liquids and, as discussed in introduction, also in thin-films [18], [20]. However, these techniques, along with all many other techniques for Raman spectroscopy not discussed in this thesis are not easily integrable on a chip so as to allow mass fabrication of a low cost lab-on-a-chip device. The major appeal of the waveguide based approach presented in this thesis is its use of as with CMOS-compatible process and its inherently microscope-free nature. In this thesis I demonstrated this lab-on-a-chip approach for quantitative spontaneous Raman sensing of bulk and monolayers of materials.

In this chapter we will explore some directions on which the work presented in this thesis is developing towards, mainly via integration with plasmonic structures, integrated resonators and spectrometers, and conclude with some perspectives for further developments. First we discuss our efforts to integrate plasmonic structures on chip.

8.1 Integration with plasmonic nanoantennas and comparison

For the case of evanescent waveguide sensing discussed in this thesis, the most significant component of signal enhancement is due to a large interaction volume distributed over the length of the waveguide. Hence, these sensors are suitable for sensing relatively larger analyte volumes. The Purcell-enhancement component of these waveguides cannot be increased arbitrarily and a very high enhancement, needed for e.g. single molecule detection, is not possible using standard designs.

To overcome with this limitation of the NWERS approach, we have also been working towards an alternative approach of using the waveguides with integrated nanoplasmonic structures. In this approach, the enhancement is the result of a plasmonic resonance effect at discrete ‘hot-spots’, i.e. regions of extreme localization of the electric field. Hence, waveguides integrated with nanoantennas are suitable for studying very small number of localized molecules. We have theoretically shown that for integrated nanoantennas, an enhancement as high as 10^{10} is possible [108]. Hence, single molecule detection in an integrated framework may be possible with such hybrid nanophotonic-plasmonic waveguides. The reader is referred to F. Peyskens’ Ph.D thesis (Ghent University, 2016) for more details.

Depending on the dimensions and the geometry of the antennas and the waveguide, we estimated that each integrated antenna discussed in this paper has an equivalent Si_3N_4 rib waveguide length of 250-2500 nm. This equivalent length is the physical length of a bare Si_3N_4 waveguide (without any gold) that is required to generate the same signal as one integrated nanoplasmonic antenna. As a rough estimate, 1 μm of a Si_3N_4 rib waveguide produces the same Raman signal as 1 plasmonic nanoantenna integrated on top of the waveguide. However, for the nanoantennas, the loss associated with gold absorption, elastic scattering, surface roughness etc. is about $e_p \sim e_s \sim 0.5$ dB per antenna [1, 113, 114]. The loss per antenna is quite high compared to the 10^{-4} dB/ μm for waveguides without the antenna. For bulk sensing, the integration of nanoplasmonic antennas is hence completely redundant because the signal generated by bare waveguides will be much larger due to the large waveguide length and small waveguide loss. On-chip SERS will however outperform the bare waveguide sensing case when particular analytes are adsorbed on the metal surface. In that case one can make use of the extreme local Raman enhancement of the plasmonic hotspots, which can be orders of magnitude higher than the field enhancement of dielectric rib or slot waveguides.

8.2 Integrated resonators

Another route to reduce the required number of probed molecules is by using integrated resonators, such as ring resonators or by fabricating Fabry–Pérot type

resonators using Bragg reflectors. If both pump and Stokes frequencies are resonant with a Q-factor Q , we also saw (S3.6.1) that for a resonator of length l and the collected signal enhances compared to the simple waveguide by a factor given by,

$$\frac{P_{ring}}{P_{wg}} = \frac{1}{2} \left(\frac{Qn}{\pi n_g} \frac{\lambda_0}{l} \right)^2 \quad (8.1)$$

While reducing the number of probe volume these resonators also enhance the signal. Several designs in this route have been fabricated and will soon be measured.

8.3 Comparison with techniques based on refractive index sensing

The data presented in Fig. 5.3 allows us to quantify the 1σ detection limit in terms of the Raman efficiency ($\rho_s\sigma$) in the order of 10^{-19} sr $^{-1}$. For the dimensions of our waveguides ($\sim 10^{-4}$ cm 2), using the surface loading value ($\sim 10^{11}$ molecules/cm 2) evaluated in §5.5 we calculate $\sim 10^7$ molecules loaded onto the waveguide; from this we calculate a detection limit of $\sim 10^4$ (~ 0.1 attomole) rhodamine molecules. Some techniques such as surface plasmon resonance (SPR) [115, 117] and dielectric refractive index (DRI) sensors (such as whispering gallery mode (WGM) [116] sensors) measure adsorption reactions via an extremely sensitive resonance shifts occurring due to minute changes in the refractive index near a surface. For these sensors, the local refractive index sensitivity as high as $\Delta n/n \sim 10^{-6}$ has been reported [116, 120]. In terms of molecular sensitivity, as low as attomolar detection limit has been reported [121] in a RNA micro-array based on SPR. As such, these two quantities are not comparable because of differences in the experimental premises. Nevertheless, from their respective detection limit values, we can conclude that NWERS technique outperforms SPR sensors for high Raman cross-section molecules as rhodamine. For small cross-section molecules, the corresponding molecular sensitivity is comparable. Maturing over more than three decades of research, several SPR technologies, such as *Biacore*, has been successfully commercialized as massively parallelizable biomolecular analytical system. Although nascent NWERS technology is inherently parallelizable, as of now, the parallelization density of several thousand biomolecular interactions as possible with SPR sensors may not be achievable with NWERS. Recently, a sophisticated combination of SPR and WGM techniques was used to monitor single molecule nucleic acid interactions [118]. In contrast, NWERS technique intrinsically depends on moderate electromagnetic enhancement of the spontaneous Raman signal collected from a large number of molecules. Hence, in terms of molecular sensitivity, NWERS is inherently non-

competitive with this technique. However, it is important to note that these techniques are indirect measurement techniques, as they measure change in the refractive index of the surface, hence offer a limited information compared to the rich information provided by a Raman spectrum from NWERS. Further, since the SPR/WGM signals lack a direct molecular signature, these techniques are prone to errors occurring from non-specific binding, or due to changes in the refractive index of the buffer, a regularly occurring problem in molecular biochemistry. In addition, as discussed in the previous sections, NWERS technique can potentially echo the advantages of SPR and WGM techniques by the integration of ring resonators and plasmonic nanoantennas, with added value of specificity and richness of Raman signal. It is for the direct correspondence of the Raman signals with the biochemistry of the molecule, and the properties described in the next section that the proposed NWERS technique is truly unique and useful.

8.4 General Conclusions

In this thesis we discussed an integrated-waveguide approach for on-chip spontaneous Raman spectroscopy using the evanescent field of the dielectric waveguide for excitation and collection. The effects of the waveguide parameters and polarization of the modes on the overall evanescent excitation and collection efficiency of spontaneous Raman scattering were discussed and validated experimentally. Here we reiterate the major significance of the results presented in this thesis.

8.4.1 Microscope-less

Microscope is a costly and bulky part of a Raman system commonly employed in laboratories. It has several moving parts and optics that needs to be aligned precisely. The results presented in this thesis shows that Raman spectroscopy is possible using all-integrated optics platform, without any moving parts. This is facilitated by the smallest étendue of the single mode waveguides described next.

8.4.2 Smallest étendue enabling integration with compact spectrometers and light sources

The étendue is an important parameter characterizing the throughput of optical power in an optical beam or optical systems (described in appendix D). As a light beam propagates in an optical system, étendue either remains constant or increases, a statement known as the principle conservation of étendue. Thus, small étendue is always preferred in an optical system design. Small étendue of light ensures maximal illumination on the detector for a given optical power, hence allows for a small spectrometer size with a high resolution. The étendue of the fundamental modes of

the waveguides are the smallest by definition. Hence, the light collected in a single mode waveguide can be analyzed by the smallest integrated spectrometers with a high resolution and high power efficiency. Similarly, coupling of light from a source to an optical system is also governed by the conservation of étendue. Many of the single mode laser sources are thus directly integrable to the single mode waveguide system as the sensing apparatus, where both excitation and collection light travel. Hence, low étendue of the NWERS sensors discussed in this thesis warrants a compact all-integrated sensor with a single mode laser source, a high resolution and compact spectrometer, and possibly filters and detectors all integrated on a single chip, without loss of a significant amount of light. The readers are referred to Appendix D for a formal proof of the role of étendue the mode number on the integration of the spectrometer.

8.4.3 High Performance

As discussed (Chapter 3 and Chapter 4), NWERS is based on enhanced interaction volume and enhanced scattering efficiency of spontaneous Raman scattering near nanophotonic waveguides. For a monolayer of analyte on top of one centimeter silicon nitride waveguide, NWERS delivers a signal that is more than four orders of magnitude higher in comparison to a confocal Raman microscope. Similarly for bulk, more than about three orders of magnitude signal is expected compared to a confocal Raman microscope.

8.4.4 CMOS compatible

In the past 50 years the electronics industry has invested billions of dollars in developing the CMOS fabrication infrastructure that has scaled up in volume and precision, while at the same time scaled down in cost per device. One of the most important characteristic of our waveguides is its compatibility with CMOS fabrication infrastructure. Silicon nitride used for our waveguides are routinely used as lithographic mask in CMOS fabrication processes. Using the same infrastructure for fabrication of the devices and integration of light sources and detectors provides a mass-fabrication platform which we envisage would lead a way to a point-of-need Raman devices

8.5 Closing Remarks: Applications

In this thesis we have focused more on conceptual developments and proof-of-concept demonstrations of the use of NWERS approach. Nevertheless, we discussed a few proof-of-concept applications of the NWERS approach for Raman spectroscopy, namely,

1. Raman spectroscopy of bulk liquids and solutions.
2. Raman spectroscopy of the solid materials constituting the waveguide itself.
3. Raman spectroscopy of monolayers of biotin/streptavidin etc.
4. Real-time observation of hybridization of DNA monolayers.
5. Raman spectroscopy of cell membranes.

It is important to explore a variety of potential applications of the NWERS. The technique is particularly suited for point-of-need applications to really take the advantages of the compactness and sensitivity that we have discussed. Needless to say, exploration of each of these potential applications of NWERS, in their own right, require a substantial research effort and time.

A

Calculation of Green's Dyadic and density of states

According to Poynting's theorem [36], the out of phase component of the oscillating current density \vec{J} and the corresponding driving electric field \vec{E} , dissipates a power P as follows

$$P = \frac{dW}{dt} = -\frac{1}{2} \int \Re\{\vec{J}^* \cdot \vec{E}\} dV \quad (\text{A.1})$$

An oscillating current density $\vec{J}(\vec{r})$ at an arbitrary location \vec{r} can be written in terms of an oscillating dipole \vec{d} at a location \vec{r}_0 , also oscillating at the same angular frequency ω , such that,

$$\vec{J}(\vec{r}) = -i\omega \vec{d} \delta(\vec{r} - \vec{r}_0) \quad (\text{A.2})$$

Using Eq. (A.1) and Eq. (A.2), the dissipation of the dipole can be calculated as:

$$P = -\frac{1}{2} \int \Re\{\vec{J}^* \cdot \vec{E}\} = \frac{\omega}{2} \Im\{\vec{d}^* \cdot \vec{E}(\vec{r}_0)\} \quad (\text{A.3})$$

If the current \vec{J} is not subject to other dissipation pathways, such as thermal losses, the dissipation power given by Eq. (A.3) is directly related to the radiated electromagnetic field. Eq. (A.3) can be simplified further if the impinging field $\vec{E}(\vec{r}_0)$ in Eq. (A.3) is expressed as a radiation from a similar dipole located at the

same location. This can be done by using a second order tensor (dyadic) called Green's dyadic function $\overleftrightarrow{G}(\vec{r}, \vec{r}_0)$. The Green's dyadic $\overleftrightarrow{G}(\vec{r}, \vec{r}_0)$ describes the field $\vec{E}(\vec{r})$ at a point \vec{r} from a point dipole source located at a position \vec{r} is given by:

$$\vec{E}(\vec{r}) = \omega^2 \mu_0 \overleftrightarrow{G}(\vec{r}, \vec{r}_0) \vec{d} \quad (\text{A.4})$$

Using Eq. (A.3) and (A.4), and unit vectors in the direction of \hat{d} we obtain:

$$P = \frac{\omega^3 |\vec{d}|^2 \mu_0}{2} \left[\hat{d} \cdot \Im \left\{ \overleftrightarrow{G}(\vec{r}_0, \vec{r}_0) \right\} \cdot \hat{d} \right] \quad (\text{A.5})$$

Thus, we see that the dissipation of electromagnetic energy by a dipole is determined by the magnitude of the dipole strength and imaginary component of the Green's dyadic in the direction of the dipole. Green's dyadic is related to vector potentials and related the radiation fields with the source field. For a complete treatment of Green's Dyadic the readers are referred to chapter 2 of [35]. In brief, in an isotropic and homogenous space, the dyadic Greens function \overleftrightarrow{G} is given by :

$$\overleftrightarrow{G}(\vec{r}, \vec{r}_0) = \left[\overleftrightarrow{I} + \frac{1}{k^2} \nabla \nabla \right] \frac{e^{ik|\vec{r}-\vec{r}_0|}}{4\pi |\vec{r}-\vec{r}_0|} \quad (\text{A.6})$$

$$\begin{aligned} \overleftrightarrow{G}(\vec{r}, \vec{r}_0) = \\ \left[\overleftrightarrow{I} + \frac{1}{k^2} \nabla \nabla \right] \frac{1}{4\pi} \left(\frac{1}{|\vec{r}-\vec{r}_0|} + \frac{ik}{2!} - \frac{k^2 |\vec{r}-\vec{r}_0|^2}{3!} + \dots \right) \end{aligned} \quad (\text{A.7})$$

Here, the term outside the square brackets is well-known scalar Green's function, used as the source of scalar waves. The dyadic terms inside the square brackets accounts for the transverse nature of the radiation. The expansion in Eq. (A.6) allows us to distinguish the real and imaginary part and calculate the near field approximation of the Green's function. In an isotropic and homogeneous medium only the dyadic components in the direction the dipole (as represented by \hat{d}) give rise to a non-zero contribution. In such a case, the square bracketed term reduces to the trace of the dyadic. Using expansion in Eq. (A.6), taking the limit $|\vec{r}-\vec{r}_0| \rightarrow 0$, we obtain:

$$\begin{aligned} \left[\hat{d} \cdot \Im \left\{ \overleftrightarrow{G}(\vec{r}_0, \vec{r}_0) \right\} \cdot \hat{d} \right] &= \Im \left\{ Tr \left[\overleftrightarrow{G}(\vec{r}_0, \vec{r}_0) \right] \right\} \\ &= \frac{1}{4\pi} \left(\frac{k}{2} \right) [2] \\ &= \frac{k}{4\pi} \end{aligned} \quad (\text{A.8})$$

Hence, using Eq. (A.5)

$$P = \frac{\omega^3 |\vec{d}|^2 \mu_0}{2} \frac{2}{3} \mathfrak{S} \left\{ \text{Tr} \left[\overleftrightarrow{G}(\vec{r}_0, \vec{r}_0) \right] \right\} = \frac{\omega^3 |\vec{d}|^2 \mu_0}{2} \frac{2}{3} \left(\frac{k}{4\pi} \right) \quad (\text{A.9})$$

$$P = n \frac{\omega^4}{12\pi\epsilon_0 c^3} |\vec{d}_\omega|^2 \quad (\text{A.10})$$

Eq. (A.8) gives the total space-time-averaged power radiated by a dipole in a homogenous medium with refractive index n . The $2/3$ factor in front of the trace in Eq. (A.3) originates from the averaging of the Green's function over the three possible dipole orientations and two polarizations because of the rotational symmetry of the problem. In Eq. (A.7), 2 is the trace of the dyadic part of the Green's function, i.e square bracketed terms.

In Eq. (A.8) the square bracketed term is the Green's function for the free space evaluated in the direction of dipole. Because of the symmetry of a homogeneous medium, one cannot assign a specific direction to the dipole. Hence, we need to average over three possible dipole orientations and two possible polarizations of the radiation field, which leads to an extra factor of $2/3$ (in front of the square-brackets). However, as we discuss in Chapter 3, if the dipole is constrained to emit at a particular direction and polarization, such as in case of scattering or a cavity, where the incoming field or the normalized field of the cavity determines the scattering direction and polarization, the power of emission is given by:

$$P_{3/2} = \frac{\omega^3 |\vec{d}|^2 \mu_0}{2} \left[\frac{k}{4\pi} \right] = n \frac{\omega^4}{8\pi\epsilon_0 c^3} |\vec{d}|^2 \quad (\text{A.11})$$

It is useful for discussion in Chapter 3 to express Greens dyadic in terms of **density of states** $D(\vec{r}, \omega_0)$ defined as the number of available modes per unit frequency per unit volume [35, 43]:

$$D(\vec{r}, \omega_0) \equiv \frac{6\omega}{\pi c^2} \left[\hat{d} \cdot \mathfrak{S} \left\{ \overleftrightarrow{G}(\vec{r}_0, \vec{r}_0) \right\} \cdot \hat{d} \right]$$

This allows to write Eq. (A.5) in terms of density of states which is calculated explicitly in Chapter 3 for diferent cases in several inhomogeneous media,

$$P = \frac{\pi\omega^2}{4\epsilon\epsilon_0} |\vec{d}|^2 D(\vec{r}_0, \omega_0) \quad (\text{A.12})$$

B

Calculation of Signal-to-noise ratio

Here we discuss the signal-to-noise performance of the WGBL shot-noise limited NERS system for low concentration in comparison with the dark-noise limited free-space system.

We verified that the photon counts statistics of the CCD detector follows a Poisson distribution (Fig B.1 and Fig B.2). It follows that the SNR can be defined as:

$$SNR \equiv \frac{C_v - C_{BG}}{\sqrt{C_v}} \quad (\text{B.1})$$

where C_v is the average number of photon counts of the signal peak at wavenumber ν and C_{BG} is the average number of photon counts near the bottom of the peak that correspond to the WGBL (see Chapter 7). In terms of experimental variables such as input power P_{in} , signal integration time t_{int} , the product of scattering cross-section and the density of the molecules (β_s for signal and β_{BG} for the background), interaction length l and detector dark noise equivalent power D , the SNR can be expressed as:

$$SNR = \theta \frac{P_{in} \eta_s l \beta_s \sqrt{t_{int}}}{\sqrt{P_{in} l (\eta_s \beta_s + \eta_{BG} \beta_{BG}) + D}} \quad (\text{B.2})$$

Where, θ is square root of the detector sensitivity which will be omitted in the following. Here we have implicitly used the experimental fact that dark counts are linear with the integration time and that the noise follows the Poisson statistics (Fig

B.2). Here, we have considered the waveguide materials act as a source of WGBL light emitting in the same frequency, which is quantified by $\eta_{BG}\beta_{BG}$.

High concentration limit If the shot noise originating from the signal is the dominant source of noise, i.e. $\eta_s\beta_s > \eta_{BG}\beta_{BG} > D$, Eq. (B.2) can be written as:

$$SNR = \sqrt{lP_{in}t_{int}\eta_s\beta_s} \quad (B.3)$$

In this situation, the SNR for the NERS system is larger than the ideal free-space system by a factor $\sqrt{l\eta_s}$ for the same integration time and input power. To obtain a similar SNR, the integration time needed is then reduced by a factor $l\eta_s$ for the NERS system compared to an ideal free-space system.

Low concentration limit For a waveguide system detecting a very low analyte concentration, β_{BG} is the dominating source of noise, hence, the SNR for the waveguide SNR_{WG} can be written as:

$$SNR_{WG} = \sqrt{lt_{int}P_{in}} \frac{\eta_s\beta_s}{\sqrt{\eta_{BG}\beta_{BG}}} \quad (B.4)$$

Similarly for an ideal free-space system without any source of WGBL, SNR is limited only by the dark noise of the detector; hence the SNR for a dark limited system SNR_{DL} is given by

$$SNR_{DL} = P_{in}\beta_s\sqrt{\frac{t_{int}}{D}} \quad (B.5)$$

Hence, for the same integration time and input power,

$$\frac{SNR_{WG}}{SNR_{DL}} = \eta_s\sqrt{\frac{l}{P_{in}} \frac{D}{\eta_{BG}\beta_{BG}}} \quad (B.6)$$

For a low concentration, and similar SNR, the reduction in integration time for a NERS system compared to the ideal free-space system is a quadratic function of the surface conversion efficiency η_s since

$$\frac{t_{int,DL}}{t_{int,WG}} = \eta_s^2 \frac{l}{P_{in}} \frac{D}{\eta_{BG}\beta_{BG}} \quad (B.7)$$

As we saw in chapter 8, we have estimated $\eta_{BG}\beta_{BG} \sim 10^{-9}\text{cm}^{-1}$ and $D \sim 2$ fW for the CCD used in our measurement operating at maximum cooling at -80°C . Then, for 1 cm waveguide and 1 mW pump, the reduction in integration time is $t_{DL}/t_{WG} \sim 10^{-3}\eta_s^2$. For the waveguide investigated in this paper, $\eta_s \sim 2 \cdot 10^5$ (surface sensing). Hence, the reduction in the integration time is $\sim 8 \cdot 10^5$. For bulk sensing, η_s has to be replaced with $\phi = l_{eq}^{-1} \sim 10^3$ introduced by Eq. (4.2) consequently the reduction in integration time is a bit less $\sim 10^3$.

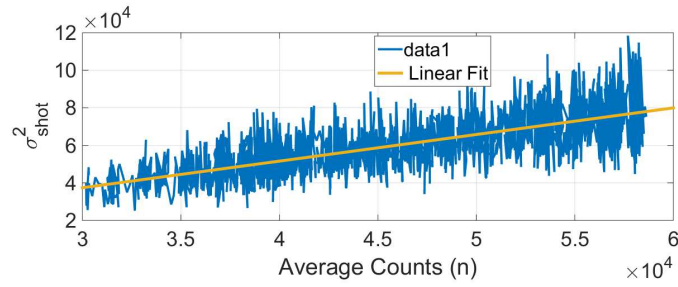


Fig. B.1 Shot noise as a function of the average number of counts for Andor iDus spectrometer. Shot noise associated with the thermal source light spectrum calculated by measuring 100 spectra. The golden linear line has slope of (1.41 ± 0.33) , implying that $\sigma = (1.19 \pm 0.23) n$. Adapted from Master's Thesis of Ali Raza (2015, Ghent University)

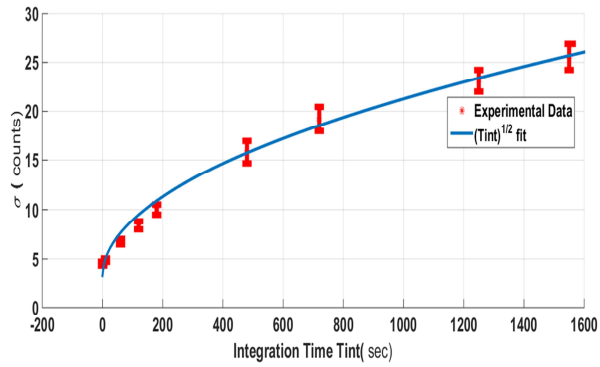


Fig. B.2 Dark noise of a spectrometer (Andor iDus) as a function of integration time. The noise variance follows $\sigma \propto t^{\frac{1}{2}}$. Adapted from Master's Thesis Ali Raza (2015, Ghent University)

C

DNA hybridization kinetics

Here we develop a model of Raman signal dependence as a function of DNA hybridization. We consider a probe monolayer of DNA immobilized on top of the photonic chip with a total surface density ρ_t . The free (unoccupied) immobilized probe DNA with average surface density ρ_f and the target cDNA in the analyte solution with surface density $\rho_{a,s}$ (with a proportional volume density ρ_a) produce the hybridization duplex with surface density ρ_h , such that $\rho_t = \rho_h + \rho_f$. The reaction can be described by the following kinetic equation.

$$\rho_f + \rho_{a,s} \rightleftharpoons \rho_h \quad (\text{C.1})$$

Here K_1 is the association constant that describes the binding rate of DNA and cDNA, while K_{-1} is the dissociation constant which describes the rate of dissociation of hybridization duplex into the surface DNA and cDNA.

Assuming no other interactions between the species occur, the hybridization rate can be described by a first order rate equation as follows.

$$\frac{d\rho_h}{dt} = K_1\rho_f\rho_a - K_{-1}\rho_h \quad (\text{C.2})$$

The unoccupied DNA density ρ_f participating in the reaction is the difference between total probe DNA concentration ρ_t and hybridized DNAs concentration, i.e $\rho_f = \rho_t - \rho_h$. Thus,

$$\frac{d\rho_h}{dt} = -\rho_h(K_1\rho_a + K_{-1}) + \rho_a\rho_tK_1 \quad (\text{C.3})$$

We assume that the concentration ρ_a of the target cDNA on top of the waveguide remains constant and is sufficiently low to affect the signal from hybridization complex. Then, the measured Raman signal from the hybridization is proportional to the density of the hybridization complex ρ_h as per Eq. (4.4). Hence, we obtain Eq. (C.4) for the evolution of the Raman signal.

$$\zeta(\tau) = \zeta_\infty \left(1 - e^{-(K_1\rho_a + K_{-1})\tau}\right) \quad (\text{C.4})$$

where, $\zeta(\tau)$ is the normalized Raman signal intensity, defined by Eq. (4.4) in the main article, collected through the waveguide at a time τ after the start of the reaction, ζ_∞ is the normalized Raman signal corresponding to the total number of binding sites i.e.the Raman signal at the time of saturation. For the hybridization of DNA with a chain length > 20 , as in our case, typically [79]-[80] $K_{-1} \ll 10^{-4} \text{s}^{-1}$ while $K_1 > 10^5 \text{M}^{-1}\text{s}^{-1}$, thus, for a concentration $\rho_a > 10 \text{nM}$, the equation is reduced to:

$$\zeta(\tau) = \zeta_\infty \left(1 - e^{-\tau K_1 \rho_a}\right) \quad (\text{C.5})$$

D

Étendue of a beam, number of modes and spectrometer size

The étendue G of a light beam, forming a solid angle $d\Omega$ (with corresponding cone half angle α , and numerical aperture NA) crossing an area S whose normal is oriented at an angle θ with the beam (Fig D.1), is defined as

$$G = \int n^2 dS \int \cos \theta d\Omega = \pi S n^2 \sin^2 \alpha = \pi S (NA)^2 \quad (\text{D.1})$$

Étendue is an important parameter characterizing the divergence and concentration of optical power in optical beams or in optical systems. In case of optical systems, étendue is sometimes also called throughput of the system as it determines the amount of light that can pass through the system. As a light beam propagates in an optical system, étendue either remains constant or increases, a statement known as the principle conservation of étendue [111]. Thus, small étendue is always preferred in an optical system design. Small étendue of light ensures maximal illumination on the detector for a given optical power, hence allows for a small spectrometer size with a high resolution. The étendue of the fundamental modes of the waveguides are the smallest by definition. Hence, the light collected in a single mode waveguide can be analyzed by the smallest integrated spectrometers with a high resolution and high power efficiency. Similarly, coupling of light from a source to an optical system is also governed by the conservation of étendue. Many of the single mode laser sources are thus directly integrable to the single mode waveguide system as the sensing apparatus, where both excitation and collection

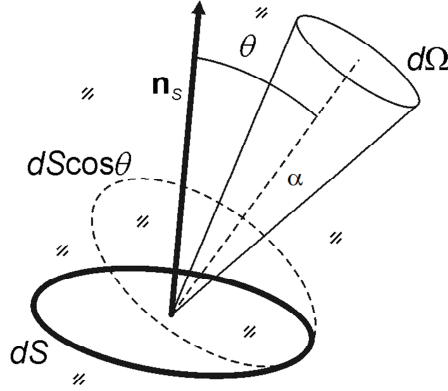


Fig. D.1 | Illustration of several quantities used in the definition of étendue of a light source or a beam. Adapted from Wikipedia.

light travel. Below we prove that smallest étendue leads to smallest spectrometer size.

For a circular beam, it is convenient to define one dimensional equivalent the étendue of a beam, called beam parameter product, which is the product of beam divergence α and the beam waist w_0 , the smallest size of the beam. For a diffraction limited Gaussian beam it is given by $w_0 \cdot \frac{\lambda}{\pi w_0} = \frac{\lambda}{\pi}$. The quality of an arbitrary beam is measured in terms of a parameter called M^2 number which measures the beam parameter product of the beam in comparison to the diffraction limited beam. The half-angle of the divergence α of such an arbitrary beam is then given by [111, 112],

$$\alpha = M^2 \frac{\lambda}{\pi w_{in}} \quad (\text{D.2})$$

Let's assume a spectrometer in a Czerny-Turner configuration (Fig. D.2). Let's assume that the beam waist w_{in} lies at the entrance of the spectrometer and an aperture size D of the optics (determined by the smallest size of the optics, including the grating). The Bragg condition for the grating in the spectrometer stipulates that,

$$\sin \theta_{out} - \sin \theta_{in} = m \frac{\lambda}{\Lambda} \quad (\text{D.3})$$

For simplicity we take $\theta_{in} \sim 0$, hence, for a small shift $\Delta\lambda$ in wavelength, the change in output angle is given by

$$\Delta\theta_{out} \approx m \frac{\Delta\lambda}{\Lambda} \quad (\text{D.4})$$

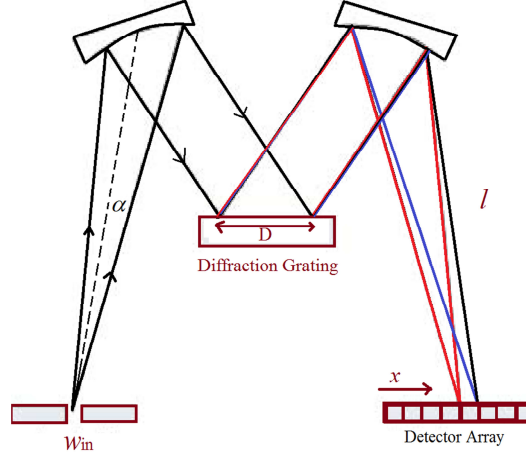


Fig. D.2 A spectrometer in Czerny-Turner configuration. The smallest aperture size D , beam divergence α , M^2 of the input mode and the device beam path l of the spectrometer and determines the spectral resolution.

Which leads to a shift of the spot position in the image plane given by

$$\Delta x_{out} = 2lm \frac{\Delta\lambda}{\Lambda} = w_{in} \quad (\text{D.5})$$

The spectral resolution $\Delta\lambda$ of a spectrometer is determined by the requirement that the shift in the image spot Δx is larger than or equal to the spot-size of the image $\Delta x_{out} \geq 2w_{out} = 2w_{in}$, where the system is assumed to be of unity magnification and the pitch of the detector array is assumed to be small enough compared to the width of ($\ll w_{out}$). This leads to following relationship for the spectral resolution

$$\frac{\Delta\lambda}{\lambda} = M^2 \frac{2\Lambda}{\pi m D} \quad (\text{D.6})$$

Thus, the resolution of a spectrometer is proportional to M^2 of the beam, which is a function of étendue of the beam or the optics. A diffraction-limited beam has an M^2 factor of 1 and smaller values of M^2 are physically not possible. A multimode beam of order (n, m) , for example Hermite–Gaussian beam for TEM_{nm} resonator mode, has an M^2 factor of $(2n+1)$ in the x direction, and $(2m+1)$ in the y direction [111, 112]. Hence, the resolution of a system increases as the order of mode of the beam, and fundamental mode $n = m = 0$ ensures smallest resolution of the spectrometer. Further, we see that the aperture size D of the spectrometer for a given resolution is smallest for $M^2 = 1$.

References

- [1] Dhakal, A., Peyskens, F., Clemmen, S., Raza, A., Wuytens, P., Zhao, H., Le Thomas, N. and Baets, R., 2016. Single mode waveguide platform for spontaneous and surface-enhanced on-chip Raman spectroscopy. *Interface Focus*, 6(4), p.20160015. § 1, 2, 4, 4.2, 4.3, 4.4, 4.5, 4.6, 8.1
- [2] Long, D.A., 2002. *The Raman Effect: A Unified Treatment of the Theory of Raman Scattering by Molecules*, John Wiley & Sons Ltd. West Sussex, England § 1.1, 1.3, 2, 2.2, 2.3, 2.3, 4.4
- [3] Ferraro, J.R., 2003. *Introductory Raman spectroscopy*. Academic press. § 1.1
- [4] Laserna J. J. , *Modern Techniques in Raman Spectroscopy.*, John Wiley & Sons (1996) § 1.1
- [5] Sir C. V Raman, Nobel Lecture, December 11, 1930 § 1.1
- [6] McCreery, R.L., 2005. *Raman spectroscopy for chemical analysis* (Vol. 225). John Wiley & Sons. § 1.1, 1.2, 2.5, 2.5.2
- [7] Cialla, D., Deckert-Gaudig, T., Budich, C., Laue, M., Möller, R., Naumann, D., Deckert, V. and Popp, J., 2009. Raman to the limit: tip-enhanced Raman spectroscopic investigations of a single tobacco mosaic virus. *Journal of Raman Spectroscopy*, 40(3), pp.240-243. § 1.1, 2.4
- [8] Dochow, S., Beleites, C., Henkel, T., Mayer, G., Albert, J., Clement, J., Krafft, C. and Popp, J., 2013. Quartz microfluidic chip for tumour cell identification by Raman spectroscopy in combination with optical traps. *Analytical and bioanalytical chemistry*, 405(8), pp.2743-2746. § 1.1
- [9] Kneipp, K., Wang, Y., Kneipp, H., Perelman, L.T., Itzkan, I., Dasari, R.R. and Feld, M.S., 1997. Single molecule detection using surface-enhanced Raman scattering (SERS). *Physical review letters*, 78(9), p.1667. 1.1
- [10] Begley, R.F., Harvey, A.B. and Byer, R.L., 1974. Coherent anti-Stokes Raman spectroscopy. *Applied Physics Letters*, 25(7), pp.387-390. § 1.1

- [11] Le Ru, E. and Etchegoin, P., 2008. *Principles of Surface-Enhanced Raman Spectroscopy: and related plasmonic effects*. Elsevier. § 1.1
- [12] Fan, M., Andrade, G.F. and Brolo, A.G., 2011. A review on the fabrication of substrates for surface enhanced Raman spectroscopy and their applications in analytical chemistry. *Analytica Chimica Acta*, 693(1), pp.7-25. § 1.1
- [13] Snyder A. W. and Love J. D. , *Optical Waveguide Theory* Chapman and Hall New York, 1983. § 1.2, 3.4.2, 3.5
- [14] Pavesi, L. and Lockwood, D.J., 2004. *Silicon photonics* (Vol. 1). Springer Science & Business Media. § 1.2
- [15] Soref, R., 2010. Silicon photonics: a review of recent literature. *Silicon*, 2(1), pp.1-6. § 1.2
- [16] Subramanian, A.Z., Ryckeboer, E., Dhakal, A., Peyskens, F., Malik, A., Kuyken, B., Zhao, H., Pathak, S., Ruocco, A., De Groote, A. et al., 2015. Silicon and silicon nitride photonic circuits for spectroscopic sensing on-a-chip. *Photonics Research*, 3(5), pp. B47-B59. § 1.2
- [17] Hu, Z., Glidle, A., Ironside, C.N., Sorel, M., Strain, M.J., Cooper, J. and Yin, H., 2012. Integrated microspectrometer for fluorescence based analysis in a microfluidic format. *Lab on a Chip*, 12(16), pp.2850-2857. § 1.2
- [18] Kanger, J.S., Otto, C., Slotboom, M. and Greve, J., 1996. Waveguide Raman spectroscopy of thin polymer layers and monolayers of biomolecules using high refractive index waveguides. *The Journal of Physical Chemistry*, 100(8), pp.3288-3292. § 1.2, 8
- [19] Rabolt, J.F., Santo, R. and Swalen, J.D., 1980. Raman measurements on thin polymer films and organic monolayers. *Applied Spectroscopy*, 34(5), pp.517-521. § 1.2, 8
- [20] Bradshaw, J.T., Mendes, S.B. and Saavedra, S.S., 2005. Planar integrated optical waveguide spectroscopy. *Analytical Chemistry*, 77(1), pp.28-A. § 1.2, 8
- [21] Benabid, F., Knight, J.C., Antonopoulos, G. and Russell, P.S.J., 2002. Stimulated Raman scattering in hydrogen-filled hollow-core photonic crystal fiber. *Science*, 298 (5592), pp.399-402. § 1.2, 8
- [22] Zhang, Y., Shi, C., Gu, C., Seballos, L. and Zhang, J.Z., 2007. Liquid core photonic crystal fiber sensor based on surface enhanced Raman scattering. *Applied Physics Letters*, 90(19), p.193504. § 1.2, 8

- [23] Moss, D.J., Morandotti, R., Gaeta, A.L. and Lipson, M., 2013. New CMOS-compatible platforms based on silicon nitride and Hydex for nonlinear optics. *Nature Photonics*, 7(8), pp.597-607. § 1.3
- [24] Zhao, H., Kuyken, B., Clemmen, S., Leo, F., Subramanian, A., Dhakal, A., Helin, P., Severi, S., Brainis, E., Roelkens, G. and Baets, R., 2015. Visible-to-near-infrared octave spanning supercontinuum generation in a silicon nitride waveguide. *Optics letters*, 40 (10), pp.2177-2180. § 1.3
- [25] Subramanian, A.Z., Neutens, P., Dhakal, A., Jansen, R., Claes, T., Rottenberg, X., Peyskens, F., Selvaraja, S., Helin, P., Dubois, B. and Leyssens, K., 2013. Low-loss singlemode PECVD silicon nitride photonic wire waveguides for 532–900 nm wavelength window fabricated within a CMOS pilot line. *Photonics Journal, IEEE*, 5 (6), pp.2202809. § 1.3, 1.1
- [26] Romero-García, S., Merget, F., Zhong, F., Finkelstein, H. and Witzens, J., 2013. Silicon nitride CMOS-compatible platform for integrated photonics applications at visible wavelengths. *Optics express*, 21(12), pp.14036-14046. § 1.3
- [27] Haglund, E.P., Kumari, S., Westbergh, P., Gustavsson, J.S., Roelkens, G., Baets, R. and Larsson, A., 2015. Silicon-integrated short-wavelength hybrid-cavity VCSEL. *Optics Express*, 23(26), pp.33634-33640. § 1.3
- [28] Brouckaert, J., Bogaerts, W., Dumon, P., Thourhout, D.V. and Baets, R., 2007. Planar concave grating demultiplexer fabricated on a nanophotonic silicon-on-insulator platform. *Lightwave Technology, Journal of*, 25(5), pp.1269-1275. § 1.3
- [29] Martens, D., Subramanian, A.Z., Pathak, S., Vanslebrouck, M., Bienstman, P., Bogaerts, W. and Baets, R.G., 2015. Compact silicon nitride arrayed waveguide gratings for very near-infrared wavelengths. *Photonics Technology Letters, IEEE*, 27(2), pp.137-140. § 1.3
- [30] Momeni, B., Hosseini, E.S. and Adibi, A., 2009. Planar photonic crystal microspectrometers in silicon-nitride for the visible range. *Optics express*, 17(19), pp.17060-17069. § 1.3
- [31] Tu, X., Song, J., Liow, T.Y., Park, M.K., Yiyang, J.Q., Kee, J.S., Yu, M. and Lo, G.Q., 2012. Thermal independent silicon-nitride slot waveguide biosensor with high sensitivity. *Optics express*, 20(3), pp.2640-2648. § 1.3
- [32] Barwicz, T., Popovi, M., Rakich, P., Watts, M., Haus, H., Ippen, E. and Smith, H., 2004. Microring-resonator-based add-drop filters in SiN: fabrication and analysis. *Optics express*, 12(7), pp.1437-1442. § 1.3

- [33] Zhang, Z., Liu, D., de Felipe, D., Liu, A., Keil, N. and Grote, N., 2013. Polymer embedded silicon nitride thermally tunable Bragg grating filters. *Applied Physics Letters*, 102(18), p.181105. §1.3
- [34] Loudon, R., 2000. *The quantum theory of light*. OUP Oxford. §2, 2.2, 3.6.2
- [35] Novotny, L. and Hecht, B., 2012. *Principles of nano-optics*. Cambridge university press. §2, 3.1, A, A
- [36] Jackson, J.D., 1999. *Classical electrodynamics*. Wiley. §2, 2.2, A
- [37] Dhakal, A., Wuytens, P., Peyskens, F., Subramanian, A., Skirtach, A., Le Thomas, N. and Baets, R., 2015, May. Nanophotonic lab-on-a-chip Raman sensors: A sensitivity comparison with confocal Raman microscope. In *BioPhotonics (BioPhotonics), 2015 International Conference on IEEE*. Florence §2, 2.7.1, 2.7.1
- [38] Pampaloni, F. and Enderlein, J., 2004. Gaussian, hermite-gaussian, and laguerre-gaussian beams: A primer. *arXiv preprint physics/0410021*. §2.7
- [39] W. Herr, B. J. Holzer, and B. Muratori, “Chapter 6.4 Concept of luminosity,” in *Accelerators and Colliders* (Springer Berlin, 2013), pp. 140–146. §2.7
- [40] Turrell, G. and Corset, J. eds., 1996. Raman microscopy: developments and applications. *Academic Press*, pp. 43 §2.7.1
- [41] Purcell, E.M., 1946. Spontaneous emission probabilities at radio frequencies. *Physical Review*, 69, p.681 §3, 3.2
- [42] Yablonovitch, E., 1987. Inhibited spontaneous emission in solid-state physics and electronics. *Physical review letters*, 58, (20), p.2059. §3
- [43] Xu, Y., Lee, R.K. and Yariv, A., 2000. Quantum analysis and the classical analysis of spontaneous emission in a microcavity. *Physical Review A*, 61 (3), p.033807. §3.1, A
- [44] Rigneault, H. and Monneret, S., 1996. Modal analysis of spontaneous emission in a planar microcavity. *Physical Review A*, 54 (3), p.2356 §3.4.1
- [45] Jun, Y.C., Kekatpure, R.D., White, J.S. and Brongersma, M.L., 2008. Non-resonant enhancement of spontaneous emission in metal-dielectric-metal plasmon waveguide structures. *Physical Review B*, 78(15), p.153111. §3.4.1
- [46] Dhakal, A., Subramanian, A., Baets, R. and Le Thomas, N., 2012. The role of index contrast in the efficiency of absorption and emission of a luminescent particle near a slab waveguide. In *16th European Conference on Integrated Optics (ECIO-2012)*. §6.1

- [47] Kogelnik, H. and Weber, H.P., 1974. Rays, stored energy, and power flow in dielectric waveguides. *JOSA*, 64(2), pp.174-185. §3.4.1, 3.4.2
- [48] Dhakal, A., Subramanian, A.Z., Wuytens, P., Peyskens, F., Le Thomas, N. and Baets, R., 2014. Evanescent excitation and collection of spontaneous Raman spectra using silicon nitride nanophotonic waveguides. *Optics letters*, 39 (13), pp.4025-4028. §4, 4.1
- [49] Dhakal, A., Raza, A., Peyskens, F., Subramanian, A.Z., Clemmen, S., Le Thomas, N. and Baets, R., 2015. Efficiency of evanescent excitation and collection of spontaneous Raman scattering near high index contrast channel waveguides. *Optics express*, 23 (21), pp.27391-27404. §5.3.1, 6, 6.1
- [50] Dhakal, A., Wuytens, P., Raza, A., Peyskens, F., Subramanian, A.Z., Clemmen, S., Le Thomas, N. and Baets, R.,, "Lab-on-a-chip Raman sensors outperforming Raman microscopes," in *CLEO 2016*, USA § 4, 4.2, 4.3, 4.5, 4.6, 4.8, 4.9
- [51] Mazet, V., Carteret, C., Brie, D., Idier, J., & Humbert, B., 'Background removal from spectra by designing and minimising a non-quadratic cost function', *Chemom. Intell. Lab. Syst.* 121-133. 76 (2) (2005) §4.3.2, 7.3
- [52] Ulman, A., 2013. *An Introduction to Ultrathin Organic Films: From Langmuir-Blodgett to Self-Assembly*. Academic press. §5.1
- [53] Gennis, R.B. ed., 2013. *Biomembranes: molecular structure and function*. Springer Science & Business Media. §5.1
- [54] Richter, R.P., Bérat, R. and Brisson, A.R., 2006. Formation of solid-supported lipid bilayers: an integrated view. *Langmuir*, 22(8), pp.3497-3505. §5.1
- [55] Lu, B., Smyth, M.R. and O'Kennedy, R., 1996. Tutorial review. Oriented immobilization of antibodies and its applications in immunoassays and immunosensors. *Analyst*, 121(3), pp.29R-32R. §
- [56] Heller, M.J., 2002. DNA microarray technology: devices, systems, and applications. *Annual review of biomedical engineering*, 4(1), pp.129-153. §
- [57] Southern, E., Mir, K. and Shchepinov, M., 1999. Molecular interactions on microarrays. *Nature genetics*, 21, pp.5-9. §5.4
- [58] Castner, D.G. and Ratner, B.D., 2002. Biomedical surface science: Foundations to frontiers. *Surface Science*, 500(1), pp.28-60. §5.4
- [59] Chilkoti, A. and Hubbell, J.A., 2005. Biointerface science. *MRS Bulletin*, 30(03), pp.175-179. §5.1

- [60] Bonaccorso, F., Sun, Z., Hasan, T. and Ferrari, A.C., 2010. Graphene photonics and optoelectronics. *Nature photonics*, 4(9), pp.611-622. § 5.1
- [61] Xu, M., Liang, T., Shi, M. and Chen, H., 2013. Graphene-like two-dimensional materials. *Chemical reviews*, 113(5), pp.3766-3798. § 5.1
- [62] Castellanos-Gomez, A, 2016. Why all the fuss about 2D semiconductors? *Nature Photonics*, 10, 202–204. § 5.1
- [63] Poggi, M.A., Gadsby, E.D., Bottomley, L.A., King, W.P., Oroudjev, E. and Hansma, H., 2004. Scanning probe microscopy. *Analytical chemistry*, 76(12), pp.3429-3444. § 5.1
- [64] Lee, P.A., Citrin, P.H., Eisenberger, P.T. and Kincaid, B.M., 1981. Extended x-ray absorption fine structure—its strengths and limitations as a structural tool. *Reviews of Modern Physics*, 53(4), p.769. § 5.1
- [65] Cesareo, R., 2010. *X-Ray Fluorescence Spectrometry*. Wiley-VCH Verlag GmbH & Co. KGaA. § 5.1
- [66] Ray, S., & Shard, A. G. Quantitative analysis of adsorbed proteins by X-ray photoelectron spectroscopy. *Analytical chemistry*, 83(22), 8659-8666 (2011). §
- [67] Degen, C.L., Poggio, M., Mamin, H.J., Rettner, C.T. and Rugar, D., 2009. Nanoscale magnetic resonance imaging. *Proceedings of the National Academy of Sciences*, 106(5), pp.1313-1317. § 5.1
- [68] Ferrari, A.C. and Basko, D.M., 2013. Raman spectroscopy as a versatile tool for studying the properties of graphene. *Nature nanotechnology*, 8(4), pp.235-246. § 5.1
- [69] Kagan, M.R. and McCreery, R.L., 1995. Quantitative surface Raman spectroscopy of physisorbed monolayers on glassy carbon. *Langmuir*, 11(10), pp.4041-4047. § 5.1
- [70] Kneipp, K., Kneipp, H., Itzkan, I., Dasari, R.R. and Feld, M.S., 2002. Surface-enhanced Raman scattering and biophysics. *Journal of Physics: Condensed Matter*, 14(18), p.R597. § 5.1
- [71] Galarreta, B.C., Norton, P.R. and Lagugne-Labarthe, F., 2011. SERS Detection of Streptavidin/Biotin Monolayer Assemblies. *Langmuir*, 27 (4), pp.1494-1498. § 5.1, 5.5

- [72] Lim, D.K., Jeon, K.S., Hwang, J.H., Kim, H., Kwon, S., Suh, Y.D. and Nam, J.M., 2011. Highly uniform and reproducible surface-enhanced Raman scattering from DNA-tailorable nanoparticles with 1-nm interior gap. *Nature nanotechnology*, 6 (7), pp.452-460. §5.1
- [73] Liu, X., Shao, Y., Tang, Y. and Yao, K.F., 2014. Highly uniform and reproducible surface enhanced raman scattering on air-stable metallic glassy nanowire array. *Scientific reports*, 4. §
- [74] Peyskens, F., Dhakal, A., Van Dorpe, P., Le Thomas, N. and Baets, R., 2016., Surface enhanced Raman spectroscopy using a single mode nanophotonic-plasmonic platform. *ACS Photonics*. 3 (1), pp 102-108 §5.1
- [75] Opilik, L., Payamyar, P., Szczerbinski, J., Schuřz, A.P., Servalli, M., Hungerland, T., Schluřter, A.D. and Zenobi, R., 2015. Minimally Invasive Characterization of Covalent Monolayer Sheets Using Tip-Enhanced Raman Spectroscopy. *ACS nano*, 9 (4), pp.4252-4259. §5.1
- [76] Jun, Y.C., Briggs, R.M., Atwater, H.A. and Brongersma, M.L., 2009. Broadband enhancement of light emission in silicon slot waveguides. *Optics Express*, 17 (9), pp.7479-7490. §3.5.1
- [77] Ouldrige, T.E., řulc, P., Romano, F., Doye, J.P. and Louis, A.A., 2013. DNA hybridization kinetics: zippering, internal displacement and sequence dependence. *Nucleic acids research*, 41 (19), pp.8886-8895. §5.4
- [78] Kranenburg, O., 2005. The KRAS oncogene: past, present, and future. *Biochimica et Biophysica Acta (BBA)-Reviews on Cancer*, 1756 (2), pp.81-82. §5.4
- [79] Okahata, Y., Kawase, M., Niikura, K., Ohtake, F., Furusawa, H. and Ebara, Y., 1998. Kinetic measurements of DNA hybridization on an oligonucleotide-immobilized 27-MHz quartz crystal microbalance. *Analytical Chemistry*, 70(7), pp.1288-1296. §5.4, C
- [80] Jeng, E.S., Barone, P.W., Nelson, J.D. and Strano, M.S., 2007. Hybridization Kinetics and Thermodynamics of DNA Adsorbed to Individually Dispersed Single-Walled Carbon Nanotubes. *Small*, 3(9), pp.1602-1609. §5.4, C
- [81] Sorgenfrei, S., Chiu, C.Y., Gonzalez Jr, R.L., Yu, Y.J., Kim, P., Nuckolls, C. and Shepard, K.L., 2011. Label-free single-molecule detection of DNA-hybridization kinetics with a carbon nanotube field-effect transistor. *Nature nanotechnology*, 6(2), pp.126-132. §5.4
- [82] Hermanson, G.T., 2013. *Bioconjugate techniques*. Academic press. §5.5

- [83] Weber, P.C., Ohlendorf, D.H., Wendoloski, J.J. and Salemme, F.R., 1989. Structural origins of high-affinity biotin binding to streptavidin. *Science*, 243(4887), pp.85-88. §
- [84] Diamandis, E.P. and Christopoulos, T.K., 1991. The biotin-(strept) avidin system: principles and applications in biotechnology. *Clinical chemistry*, 37(5), pp.625-636. § 5.5
- [85] Langer, P.R., Waldrop, A.A. and Ward, D.C., 1981. Enzymatic synthesis of biotin-labeled polynucleotides: novel nucleic acid affinity probes. *Proceedings of the National Academy of Sciences*, 78(11), pp.6633-6637. § 5.5
- [86] Bistričić, L., Volovšek, V. and Dananić, V., 2007. Conformational and vibrational analysis of gamma-aminopropyltriethoxysilane. *Journal of molecular structure*, 834, pp.355-363. § 5.5
- [87] Fagnano, C., Fini, G. and Torreggiani, A., 1995. Raman spectroscopic study of the avidin—biotin complex. *Journal of Raman Spectroscopy*, 26(11), pp.991-995. § 5.5
- [88] Shim, S., Stuart, C.M. and Mathies, R.A., 2008. Resonance Raman Cross-Sections and Vibronic Analysis of Rhodamine 6G from Broadband Stimulated Raman Spectroscopy. *ChemPhysChem*, 9(5), pp.697-699. § 5.5
- [89] Kagan, M.R. and McCreery, R.L., 1994. Reduction of fluorescence interference in Raman spectroscopy via analyte adsorption on graphitic carbon. *Analytical Chemistry*, 66(23), pp.4159-4165. § 5.5
- [90] Hoff, J.D., Cheng, L.J., Meyhöfer, E., Guo, L.J. and Hunt, A.J., 2004. Nanoscale protein patterning by imprint lithography. *Nano letters*, 4(5), pp.853-857. § 5.5
- [91] Arafat, A., Giesbers, M., Rosso, M., Sudhölter, E.J., Schroën, K., White, R.G., Yang, L., Linfood, M.R. and Zuillhof, H., 2007. Covalent biofunctionalization of silicon nitride surfaces. *Langmuir*, 23(11), pp.6233-6244. § 5.8
- [92] Zhang, F. and Srinivasan, M.P., 2004. Self-assembled molecular films of aminosilanes and their immobilization capacities. *Langmuir*, 20(6), pp.2309-2314. § 5.8
- [93] Yıldırım, M.A., Goh, K.I., Cusick, M.E., Barabási, A.L. and Vidal, M., 2007. Drug—target network. *Nature biotechnology*, 25(10), pp.1119-1126. § 5.7.1
- [94] Carter, E.A., Rayner, B.S., McLeod, A.I., Wu, L.E., Marshall, C.P., Levina, A., Aitken, J.B., Witting, P.K., Lai, B., Cai, Z. and Vogt, S., 2010. Silicon

- nitride as a versatile growth substrate for microspectroscopic imaging and mapping of individual cells. *Molecular Biosystems*, 6 (7), pp.1316-1322. § 5.7.2
- [95] Richter, R.P., Bérat, R. and Brisson, A.R., 2006. Formation of solid-supported lipid bilayers: an integrated view. *Langmuir*, 22 (8), pp.3497-3505. §5.7.3
- [96] Krafft, C., Knetschke, T., Siegner, A., Funk, R.H. and Salzer, R., 2003. Mapping of single cells by near infrared Raman microspectroscopy. *Vibrational Spectroscopy*, 32 (1), pp.75-83. §5.7.3, 5.8
- [97] Dhakal, A., Peyskens, F., Subramanian, A., Le Thomas, N. and Baets, R.G., 2013, July. Enhancement of light absorption, scattering and emission in high index contrast waveguides. In *Optical Sensors*, Puerto Ricco (pp. ST2B-5). Optical Society of America. §6, 6.1
- [98] Bogaerts, W., Baets, R., Dumon, P., Wiaux, V., Beckx, S., Taillaert, D., Luysaert, B., Van Campenhout, J., Bienstman, P. and Van Thourhout, D., 2005. Nanophotonic waveguides in silicon-on-insulator fabricated with CMOS technology. *Lightwave Technology, Journal of*, 23 (1), pp.401-412. §6.3
- [99] Häyrynen, M., Roussey, M., Säynätjoki, A., Kuittinen, M. and Honkanen, S., 2015. Titanium dioxide slot waveguides for visible wavelengths. *Applied optics*, 54(10), pp.2653-2657. §6.3
- [100] Tsu, D.V., Lucovsky, G. and Mantini, M.J., 1986. Local atomic structure in thin films of silicon nitride and silicon diimide produced by remote plasma-enhanced chemical-vapor deposition. *Physical Review B*, 33(10), p.7069. § 7.1.1
- [101] Narikawa, S., Kojima, Y. and Ehara, S., 1985. Investigations of NH and Si-N bonding configurations in hydrogenated amorphous silicon nitride films by infrared absorption spectroscopy. *Japanese journal of applied physics*, 24(11A), p.L861. §7.1.1
- [102] Smith, D.L., Alimonda, A.S., Chen, C.C., Ready, S.E. and Wacker, B., 1990. Mechanism of SiN_xH_y Deposition from NH₃-SiH₄ Plasma. *Journal of the Electrochemical Society*, 137(2), pp.614-623. §7.1.1
- [103] Soudi, A., Khan, E.H., Dickinson, J.T. and Gu, Y., 2009. Observation of unintentionally incorporated nitrogen-related complexes in ZnO and GaN nanowires. *Nano letters*, 9(5), pp.1844-1849. §7.1.1

- [104] Dhakal, A., Wuytens, P., Peyskens, F., Subramanian, A.Z., Le Thomas, N. and Baets, R., 2014, May. Silicon-nitride waveguides for on-chip Raman spectroscopy. In *SPIE Photonics Europe* (pp. 91411C). International Society for Optics and Photonics. § 7.2
- [105] Shuker, R. and Gammon, R.W., 1970. Raman-scattering selection-rule breaking and the density of states in amorphous materials. *Physical Review Letters*, 25(4), p.222. § 7.1.5
- [106] Sokolov, A.P., Kisliuk, A., Quitmann, D. and Duval, E., 1993. Evaluation of density of vibrational states of glasses from low-frequency Raman spectra. *Physical Review B*, 48(10), p.7692. § 7.1.5
- [107] Eilers, P. H., & Boelens, H. F. (2005). Baseline correction with asymmetric least squares smoothing. *Leiden University Medical Centre Report*. Leiden university. § 7.3
- [108] Peyskens, F., Subramanian, A., Dhakal, A., Le Thomas, N. and Baets, R., 2013, June. Enhancement of Raman scattering efficiency by a metallic nano-antenna on top of a high index contrast waveguide. In *CLEO: Science and Innovations* (pp. CM2F-5). Optical Society of America. § 8.1
- [109] Raphael Van Laer, 2016, Light-Sound Interaction in Nanoscale Silicon Waveguides. PhD Thesis, Ghent University. § 2.2.3
- [110] Hamaguchi, H.O., Kato, C. and Tasumi, M., 1983. Observation of transient resonance raman spectra of the S 1 state of trans-stilbene. *Chemical physics letters*, 100(1), pp.3-7. § 2.4
- [111] Chaves, J., 2015. *Introduction to nonimaging optics*. CRC Press. § D, D, D
- [112] Meinhart, C.D. and Wereley, S.T., 2003. The theory of diffraction-limited resolution in microparticle image velocimetry. *Measurement science and technology*, 14(7), p.1047. § D, D
- [113] Peyskens, F., Subramanian, A.Z., Neutens, P., Dhakal, A., Van Dorpe, P., Le Thomas, N. and Baets, R., 2015. Bright and dark plasmon resonances of nanoplasmonic antennas evanescently coupled with a silicon nitride waveguide. *Optics express*, 23(3), pp.3088-3101. § 8.1
- [114] Peyskens, F., Dhakal, A., Van Dorpe, P., Le Thomas, N. and Baets, R., 2015. Surface enhanced Raman spectroscopy using a single mode nanophotonic-plasmonic platform. *ACS Photonics*, 3(1), pp.102-108. § 8.1
- [115] Mrksich, M., Sigal, G.B. and Whitesides, G.M., 1995. Surface plasmon resonance permits in situ measurement of protein adsorption on

- self-assembled monolayers of alkanethiolates on gold. *Langmuir*, 11(11), pp.4383-4385. 18. § 8.3
- [116] Vollmer, F. and Arnold, S., 2008. Whispering-gallery-mode bio-sensing: label-free detection down to single molecules. *Nature methods*, 5(7), pp.591-596. § 8.3
- [117] Homola, J., 2003. Present and future of surface plasmon resonance biosensors. *Analytical and bioanalytical chemistry*, 377(3), pp.528-539. § 8.3
- [118] Baaske, M.D., Foreman, M.R. and Vollmer, F., 2014. Single-molecule nucleic acid interactions monitored on a label-free microcavity biosensor platform. *Nature nanotechnology*, 9(11), pp.933-9. § 8.3
- [119] Koreeda, A., Takano, R. and Saikan, S., 2009. Light scattering in a phonon gas. *Physical Review B*, 80(16), p.165104. 7.1.5
- [120] Homola, J., Yee, S.S. and Gauglitz, G., 1999. Surface plasmon resonance sensors: review. *Sensors and Actuators B: Chemical*, 54(1), pp.3-15. 8.3
- [121] Fang, S., Lee, H.J., Wark, A.W. and Corn, R.M., 2006. Attomole microarray detection of microRNAs by nanoparticle-amplified SPR imaging measurements of surface polyadenylation reactions. *Journal of the American Chemical Society*, 128(43), pp.14044-14046. 8.3
- [122] Martin, A.J. and Brenig, W., 1974. Model for Brillouin scattering in amorphous solids. *physica status solidi (b)*, 64(1), pp.163-172.

7.1.5